Vibrational Modes of Carbon Nanotubes: A Force-Constant-Model Approach

Diplomarbeit

von

Janina Zimmermann

aus

Herdecke

durchgeführt am Institut für Theoretische Physik
der Universität Regensburg
unter Anleitung von

Dr. Gianaurelio Cuniberti

März 2006

Contents

Introduction

Until some decades ago, only two types of all-carbon crystalline structure were known: the naturally occurring allotropes diamond and graphite. The breakthrough which revolutionized carbon research came from experiments on clusters formed by laser vaporization on graphite: The discovery first of C_{60} in 1985 [1] and then of carbon nanotubes by S. Iijima in 1991 [2] marked the beginning of a new era in carbon science. Carbon nanotubes are crystals with the shape of hollow cylinders made of one or more graphite sheets. Soon after their discovery in multiwall form, carbon nanotubes consisting of one single graphitic layer were synthesized [3, 4].

During the past ten years carbon nanotubes (CNTs) have been at the focus of intense experimental and theoretical research. This is due to their potential for applications as well as to the fact that they represent an ideal model system to investigate the physical properties of an ordered, quasi-one-dimensional crystal. From a technological point of view, one of the highlights of nanotube research is the construction of nanotube-based electronic devices, such as single-electron transistors [5] or even logic circuits [6]. Beyond the variety of applications, single-walled CNTs (SWCNTs) are interesting for their fundamental physical properties. With a length of about 1 μm and diameters around 1 nm, single-walled CNTs fall into the size range where quantum effects become important and this, combined with their particular symmetries, leads to remarkable electronic, magnetic and vibrational properties.

Vibrational properties are the subject of increasing attention for several reasons. Besides the interest in the phonons of a system with such a unique structure [7], detailed knowledge of the vibrational spectrum of CNTs is of central importance for temperature-dependent properties such as charge, spin and heat transport [8], for superconductivity [9], and optical characterization [10]. Recently, particular attention has been paid to the thermal properties of carbon nanotubes since some of their applications may depend significantly on their thermodynamic features. A detailed knowledge of energy dissipation and thermal transport is required for controlling the performance and stability of nanotube-based devices. For this purpose, the role of molecular vibrations might be very relevant. Especially at low temperatures the thermal properties are

determined by phonons, rather then by electrons. In this temperature regime carbon nanotubes are characterized by ballistic phonon transport and thermal conductance quantization [11].

The main practical aspect related to vibrational modes of CNTs is their optical characterization: Raman spectra give information about the vibrational properties limited to the center of the Brillouin zone, which can be used to distinguish among nanotubes of different diameters through the radial breathing modes. It is a powerful tool to derive properties such as tube diameter, tube orientation, metallic or semiconducting nature of the nanotube and even tube chirality.

The first approaches to the theoretical determination of the phonon dispersion relations are phenomenological lattice-dynamical models, in particular *force-constant models*. These start from some approximation for the interatomic force constants or the potential energy of the crystal. They are based on few adjustable parameters and are able to reproduce satisfactory results and to describe accurately heat transport. An alternative tool is given by first principles or *ab initio* calculations based on the quantum mechanical description of electrons. This method includes all relevant effects and provides accurate, experimentally-confirmed results without the need for adjustable parameters. However, the computational effort is large, leading to severe restrictions in the systems which can be handled in practice. The advantage of the phenomenological models consists in their simplicity and the possibility of fast application. A good model calculation can often provide reliable information that is indeed complementary to that obtainable from more sophisticated methods.

In this work we present a detailed description of the vibrational modes of carbon nanotubes using and comparing two different force-constant models. The latter are then compared to *ab initio* results and used to calculate non-trivial thermodynamical properties of carbon nanotubes, such as the specific heat and thermal conductance.

The thesis is organized according to the following plan:

- *The physics of carbon nanotubes*
  Chapter 1 provides an introduction of the structural and geometrical properties of carbon nanotubes, starting from graphene. Afterwards we give an overview of experimental methods for measurements of vibrational frequencies, taking into consideration in particular Raman spectroscopy.

- *Fundamentals of lattice-dynamical theory*
  The theory of lattice dynamics is one of the most confirmed and successful theories of solid state physics. A review of the basics is presented in Chapter 2, emphasizing on the concept of the force-constant tensor. In this context we in-

troduce the basic ideas of the force-constant model and the *ab initio* method, illustrating their different approach to the calculation of vibrational modes. Application of force-constant models on the example of two elementary systems are also given. We begin then to draw the attention on the concepts of flexural modes and bending forces, which are of central importance for CNTs.

- *Phonon dispersion relations for graphene and carbon nanotubes*
  In Chapter 3 we turn to consider a single graphite layer, a graphene sheet. A good comprehension of the lattice dynamics of graphene is the starting point for dealing with carbon nanotubes. First, we focus on two main force-constant approaches, the valence force field model and the direct parameterization of the real-space force constants, reproducing some models presented in the literature. By applying one of these models to graphene, we were able to find a set of parameters in order to fit the phonon curves of graphene obtained by *ab initio* calculations. We continue on this track also for carbon nanotubes. In Chapter 4, we consider two specific force constant models applied to the nanotube geometry. In particular, we concentrate on the important Raman-active radial-breathing mode, which is most frequently used to characterize nanotubes, and on one of the low-energy acoustic modes, the flexural mode, and on the main point whether its dispersion is linear or quadratic. This result has crucial consequences for the low-temperature specific heat. For a better understanding, we support our calculations with the visualization of some selected modes.

- *Thermal properties of carbon nanotubes*
  The remaining part of this work is concentrated on the thermodynamics of carbon nanotubes. After discussing briefly the effect of temperature on lattice dynamics, we take into consideration the specific heat, probing that its low-temperature behavior contains information regarding the type of excitations involved and the dimensionality of the system. Eventually, we investigate the low-temperature thermal conductance of carbon nanotubes through an analysis based on the Landauer theory of heat transport. Nanotubes can conduct heat by ballistic phonon propagation. We determine the thermal conductance quantum, the ultimate limit to thermal conductance for a single phonon channel.

Chapter 1

Structural properties of carbon nanotubes

A single-wall carbon nanotube (SWCNT) is built by a single graphite layer, called graphene, rolled up into a hollow cylinder with a typical diameter of 0.7-1.5 nm. Depending on the way how to roll the sheet into a cylinder, one can obtain many possible variants of carbon nanotubes, differing in diameter, chirality, number of atoms in the unit cell, and in the orientation and size of the unit cell and the Brillouin zone. The resulting types of carbon nanotubes (CNT) can be distinguished not only by their geometrical structure but also by several important physical properties like the electronic band structure, the spatial symmetry group and, as we will see, the lattice vibrations.

In Sec. 1.1 and 1.2, we explain the methods to describe the geometry of the graphene lattice and show that it is transferable, with some adaptations, to carbon nanotubes. For more details we refer to the books of Ref. [12, 13]. Section 1.3 briefly illustrates vibrational spectroscopy on the important example of Raman scattering.

1.1 Geometric structure of graphene

Graphite is a three-dimensional (3D) layered crystal composed by planar sheets of hexagonal rings of carbon atoms ordered in a honeycomb lattice. The interaction between the graphite layers is relatively weak because the interlayer spacing of 3.35 Å is much larger than the carbon-carbon bond length $a_{\text{C-C}} = 1.42$ Å in the hexagonal rings. In this work, we will focus on a single layer of graphite, a sheet called 2D graphite or graphene.

In order to describe the geometry of graphene, we start considering the 2D hexagonal Bravais lattice, which consists of atoms ordered in a triangular pattern in the plane as

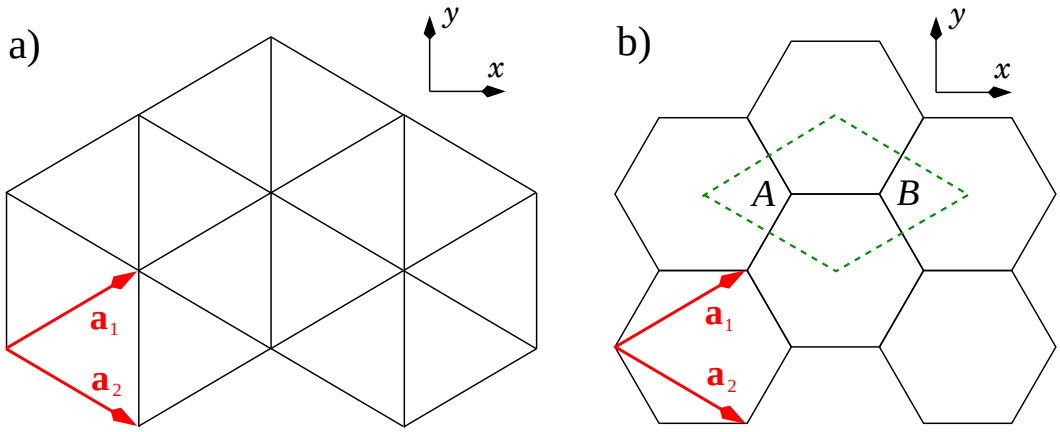

Figure 1.1: Panel (a): the 2D hexagonal lattice. Panel (b): the graphene honeycomb structure is a hexagonal lattice with a two-atom basis. The dotted lines indicate a possible choice of unit cell.

illustrated in Fig. 1.1 (panel (a)). It is defined by the lattice vectors:

$$\mathbf{a}_1 = \left(\frac{\sqrt{3}}{2}a, \frac{a}{2}\right), \qquad \mathbf{a}_2 = \left(\frac{\sqrt{3}}{2}a, -\frac{a}{2}\right) \tag{1.1}$$

with the lattice constant $a = |\mathbf{a}_1| = |\mathbf{a}_2| = 1.42 \times \sqrt{3} = 2.46$ Å. The typical honeycomb structure of graphene is a 2D hexagonal lattice with a basis of two atoms, which we call type A and B, as illustrated in Fig. 1.1 (panel (b)). There are several possibilities to choose a unit cell, the dotted lines indicate one in real space which has the shape of a rhombus and is defined by the lattice vectors in Eq. (1.1). The reciprocal lattice of both the hexagonal lattice and of graphene is again hexagonal but rotated by 90° respectively to the real space one and with a different lattice constant, which now is $4\pi/\sqrt{3}a$. The reciprocal lattice vectors fulfill the condition $\mathbf{a}_i \cdot \mathbf{b}_j = 2\pi\delta_{ij}$ and can be written as

$$\mathbf{b}_1 = \left(\frac{2\pi}{\sqrt{3}a}, \frac{2\pi}{a}\right), \qquad \mathbf{b}_2 = \left(\frac{2\pi}{\sqrt{3}a}, -\frac{2\pi}{a}\right). \tag{1.2}$$

Figure 1.2 shows the reciprocal lattice vectors pointing at the reciprocal lattice points, while the shaded hexagon indicates the Brillouin zone. The hole system has a six-fold rotational symmetry, which means that rotations by 60° do not change the lattice. Γ, K and M are high-symmetry-points and are situated respectively at the center, the corner, and the center of the edge of the Brillouin zone. We will see that it is usual to calculate the phonon dispersion relations along the lines connecting this three points.

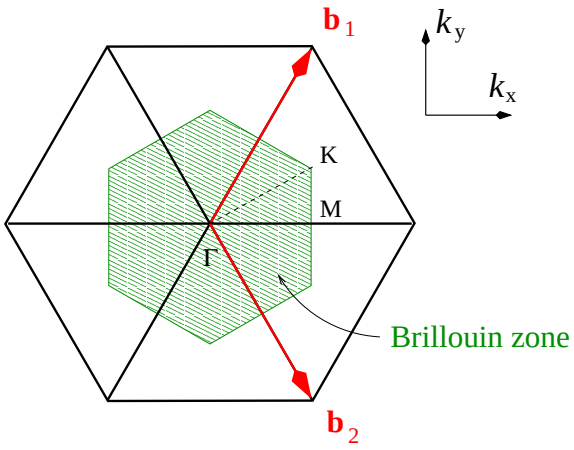

Figure 1.2: The reciprocal lattice of graphene is a two-dimensional hexagonal lattice. The grey shaded area represents the first Brillouin zone.

1.2 Geometric structure of carbon nanotubes

Since there are many possibilities to roll a graphene sheet into a cylinder, one can obtain carbon nanotubes with quite different microscopic structure. Carbon nanotubes are classified in two categories: chiral and achiral nanotubes. The first one have a spiral symmetry while the second one are completely symmetric around the nanotube axis. There are only two types of achiral nanotubes, called armchair and zigzag due to the shape of the cross section along the circumference. Three examples of nanotubes are shown in Fig. 1.3. Because the microscopic structure of carbon nanotubes is derived from that of graphene, carbon nanotubes are usually labeled in terms of graphene lattice vectors. It is common to define a circumferential vector and a vector parallel to the tube axis.

1.2.1 Chiral vector C

The chiral vector uniquely determines the hole microscopic and geometric structure of a nanotube and provides the classification of them in different categories. $\mathbf{C}$ is defined in terms of the unit vectors of graphene and the sheet is rolled up in such a way, that it becomes the circumference of the tube:

$$\mathbf{C} = n\mathbf{a}_1 + m\mathbf{a}_2 \equiv (n, m) \tag{1.3}$$

where n and m are integers and define a particular tube, as it is shown in Fig. 1.4. Consequently the tube diameter can be easily calculated by the length of the chiral

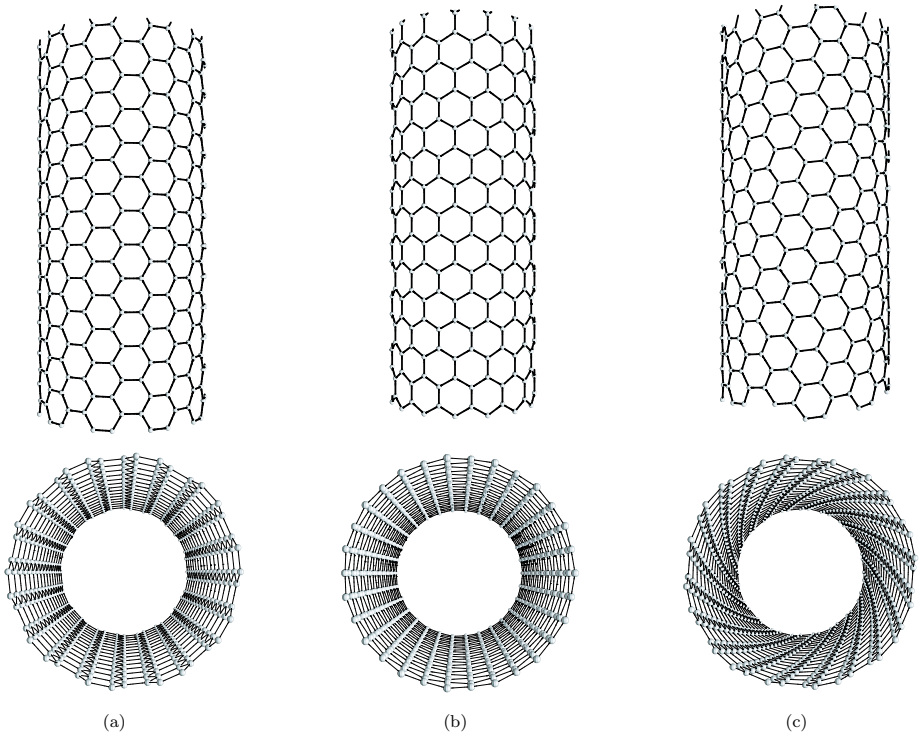

Figure 1.3: Sights from different angles on three types of carbon nanotubes: (a) an armchair (10,10) CNT, (b) a zigzag (15,0) CNT, and (c) a chiral (12,8) CNT (taken from Ref. [14]).

vector:

$$d_t = \frac{|\mathbf{C}_h|}{\pi} = \frac{a}{\pi}\sqrt{n^2 + m^2 + nm}. \tag{1.4}$$

For a stable SWCNT, typical diameter values have been observed of the order of 0.7-1.5 nm. The chiral angle ϑ is given by the chiral vector measured relative to the direction defined by $\mathbf{a}_1$ and can be calculated from

$$\cos\vartheta = \frac{\mathbf{C}\cdot\mathbf{a}_1}{|\mathbf{C}||\mathbf{a}_2|} = \frac{2n+m}{2\sqrt{n^2+m^2+nm}}. \tag{1.5}$$

Since there are six definable angles because of the hexagonal structure of the lattice, it is common the choose $|\vartheta|$ between 0° and 30°, where 0° is the special case of a

Type	$\mathbf{C}$	ϑ
armchair	(n,n)	30°
zigzag	$(n,0)$	0°
chiral	(n,m)	$0° < \|\vartheta\| < 30°$

Table 1.1: Properties of achiral (zigzag and armchair) and chiral nanotubes.

zigzag and 30° of an armchair nanotube. This restriction implies that we consider only $0 \leq m \leq n$, without loosing in generality. Table 1.1 summarizes these facts.

1.2.2 Translational vector T

The translational vector is perpendicular to the chiral vector and reproduces the periodicity of the nanotube structure along the axis direction. It is given by

$$\mathbf{T} = t_1\mathbf{a}_1 + t_2\mathbf{a}_2 \equiv (t_1, t_2) \tag{1.6}$$

t_1 and t_2 are integers and are chosen in such a way that $\mathbf{C} \cdot \mathbf{T} = 0$ with $|\mathbf{T}|$ as small as possible. We obtain

$$t_1 = \frac{2m+n}{d_R}, \quad t_2 = -\frac{2n+m}{d_R} \tag{1.7}$$

where d_R is the greatest common divisor of $2m+n$ and $2n+m$.

The chiral and the translational vector form a rectangle in the graphene sheet which becomes, after rolling the sheet, a finite size cylinder; the latter defines the unit cell of the nanotube. The translational period $|\mathbf{T}|$ is strongly dependent on the chirality of the tube, in fact armchair nanotubes have the shortest unit cells with less number of atoms and chiral tubes can have very long unit cells with many more atoms (see below). Figure 1.4 shows the unrolled honeycomb lattice with the graphene unit vectors $\mathbf{a}_1$ and $\mathbf{a}_2$ and an example of chiral and translational vector. Considering that the area of the rectangular unit cell of a nanotube is $|\mathbf{C} \times \mathbf{T}|$, the number N of graphene hexagons per unit cell is:

$$N = \frac{|\mathbf{C} \times \mathbf{T}|}{|\mathbf{a}_1 \times \mathbf{a}_2|} = \frac{2(m^2 + n^2 + nm)}{d_R} \tag{1.8}$$

and since the graphene unit cell contains two atoms, the number of atoms per nanotube unit cell is $2N$. For example a (10,10) CNT has 40 atoms in the unit cell, the close-by (10,9) CNT has 1084. As we will see later in this work, three-dimensional phonon dispersion relations have $6N$ branches, meaning that two geometrically similar nanotubes will lead to very different phonon spectra.

1.2.3 Brillouin zone of carbon nanotubes

As mentioned, the unit vectors of a CNT are the chiral and the translational vector, which define a finite size cylinder. The reciprocal lattice vectors have to be perpendicular to the unit vectors in real space, therefore we obtain one in the direction of the

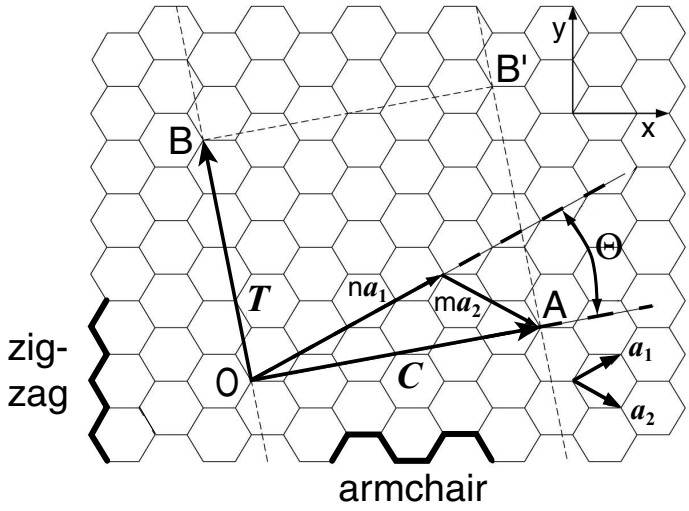

Figure 1.4: The graphene honeycomb lattice. The chiral vector $\mathbf{C}$ and the translational vector $\mathbf{T}$ are shown on the example of a $(n, m) = (4, 2)$ CNT. The tube can be constructed by rolling the honeycomb sheet so that points O and A coincide (and B and B' coincide). ϑ denotes the chiral angle (taken from Ref. [15]).

tube axis, defined as $\mathbf{K}_2$, and one that points along the circumference, $\mathbf{K}_1$. We can calculate them with the relations

$$\begin{aligned} \mathbf{C} \cdot \mathbf{K}_1 &= 2\pi, \quad & \mathbf{T} \cdot \mathbf{K}_1 &= 0, \\ \mathbf{C} \cdot \mathbf{K}_2 &= 0, \quad & \mathbf{T} \cdot \mathbf{K}_2 &= 2\pi \end{aligned} \tag{1.9}$$

and obtain using Eq. (1.7-1.8):

$$\mathbf{K}_1 = \frac{1}{N}(-t_2\mathbf{b}_1 + t_1\mathbf{b}_2), \qquad \mathbf{K}_2 = \frac{1}{N}(m\mathbf{b}_1 - n\mathbf{b}_2) \tag{1.10}$$

where $\mathbf{b}_1$ and $\mathbf{b}_2$ are the reciprocal lattice vectors of graphene. The vector $\mathbf{K}_1$ is naturally discretized by the periodic boundary condition of the circumferential direction of the nanotube, while $\mathbf{K}_2$ depends on the boundary condition at the nanotube edges. In case of an infinitely long nanotube the vector $\mathbf{K}_2$ is continuous. The wave vectors along the circumferential direction obey to the following quantization condition:

$$\mathbf{k} \cdot \mathbf{C}_h = 2\pi\ell_1 \quad \Longrightarrow \quad \mathbf{k} = \ell_1 \cdot \mathbf{K}_1 \tag{1.11}$$

where ℓ_1 is an integer and goes from 0 to $N-1$. Since $N\,\mathbf{K}_1 = -t_2\mathbf{b}_1 + t_1\mathbf{b}_2$ is a vector in the reciprocal lattice of graphene, wave vectors which differ by $N\,\mathbf{K}_1$ are equivalent. For $\ell_1 = 1, ..., N-1$ none of the $N-1$ vectors $\ell_1\,\mathbf{K}_1$ are reciprocal lattice vectors of graphene, because t_1 and t_2 have no common divisor – see Eq. (1.7). Though the

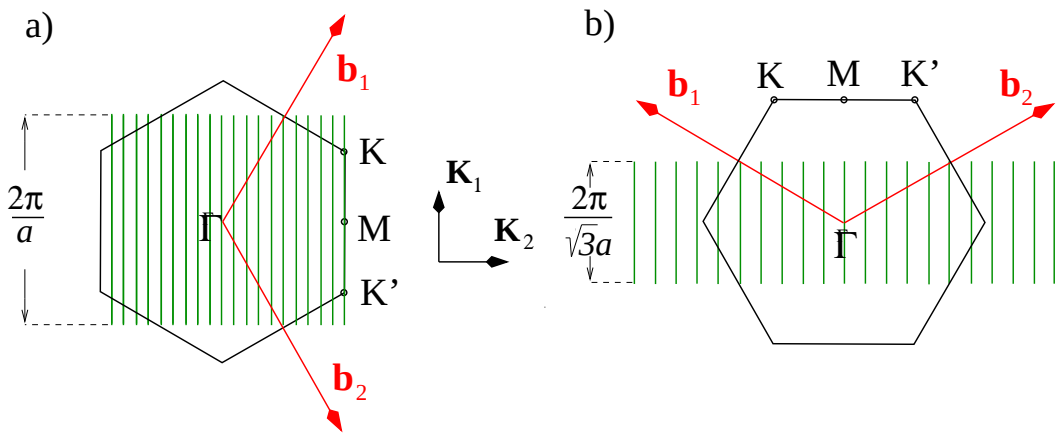

Figure 1.5: The Brillouin zone of a (10,10) CNT (panel (a)) and a (10,0) CNT (panel (b)). It consists of N lines parallel to $\mathbf{K}_2$, the reciprocal lattice vector along the tube axis.

quantization condition implies that we have N discrete q vectors given by $\ell_1 \mathbf{K}_1$ with $\ell_1 = 0, ..., N-1$.

The one-dimensional Brillouin zone of carbon nanotubes is therefore a cut through the Brillouin zone of graphene and consists of N lines parallel to the axis direction of length $2\pi/|\mathbf{T}|$, as illustrated in two examples in Fig. 1.5. The number of lines increases with increasing diameter, while their distance decreases. The allowed states are given by

$$\mathbf{k} = \ell_1 \mathbf{K}_1 + \ell_2 \frac{\mathbf{K}_2}{|\mathbf{K}_2|} \quad \text{with} \quad -\frac{\pi}{|\mathbf{T}|} \leq \ell_2 \leq \frac{\pi}{|\mathbf{T}|}, \quad \ell_1 = 0, ..., N-1. \tag{1.12}$$

If one of this lines goes through a K point, the nanotube is metallic, otherwise it is semiconducting.

1.3 Experimental aspects

Of the common spectroscopic methods for the investigation of vibrations in solids—inelastic X-ray scattering, light scattering, far-infrared absorption spectroscopy, and neutron scattering [16]—Raman scattering has been by far the most used. We briefly discuss the basics of Raman scattering and illustrate their importance for the analysis of carbon nanotube spectra.

1.3.1 Raman scattering

Inelastic light scattering by phonons, or Raman spectroscopy, is a useful *in-situ* non destructive tool for investigating and characterizing molecular vibrations. It provides a powerful method for determining phonon dispersion relations, particularly in low dimensional materials, when combined with information about the electronic structure. The Raman process includes absorption and emission of light as well as inelastic scattering of electrons by phonons. Besides the characterization of vibrations, also information on electronic properties and electron-phonon interaction is obtained.

First order Raman scattering is a three-step process: an incoming photon with a frequency ω_1 and wave vector $\mathbf{q}_1$ excites an electron-hole pair. The electron is scattered inelastically under the emission of a phonon with frequency ω_{ph} and wave vector $\mathbf{q}_{\mathrm{ph}}$. The electron-hole pair finally recombines and emits the scattered photon ω_2 with wave vector $\mathbf{q}_2$. Energy and momentum are conserved during the process:

$$\hbar\omega_1 = \hbar\omega_2 \pm \hbar\omega_{\mathrm{ph}} \tag{1.13}$$

$$\mathbf{q}_1 = \mathbf{q}_2 \pm \mathbf{q}_{\mathrm{ph}} \tag{1.14}$$

In the one phonon emission (Stokes process) or absorption (anti-Stokes process), one of the two scattering processes is inelastic with a phonon emission or absorption, and the other is an elastic scattering process mediated by the defect. Furthermore the Raman spectra may change if one changes the frequency of the excitation laser. When the excitation energy is close to an electronic state energy of high optical absorption, the Raman intensity is enhanced, and this is known as the resonant Raman effect. Under resonant conditions, more light can be absorbed, thereby enhancing the Raman signal through the electron-phonon coupling process.

Among the $6N$ calculated phonon dispersion relations for carbon nanotubes, only a few modes are Raman or infrared (IR) active, as specified by the symmetry of the phonon modes. Group theory predicts that there are 15 or 16 Raman-active modes at $q = 0$ for both chiral and achiral nanotubes. The Raman experiments in first order excited with laser light in the visible or near-visible energy regime (514 - 1320 nm [10]) are limited to Γ-point phonons ($\mathbf{q} = 0$) due to the small wave vector of the incident light. For second-order scattering, the elastic scattering by a defect is replaced by inelastic scattering by a second phonon. In the case of two phonons with the same frequency but opposite wave vector, the Raman shift is about twice the single phonon (first order) frequency and hence the shift with laser energy is approximately doubled. In higher order processes the phonon wave vectors are not restricted to zero. The mechanism of double resonance dominates the entire Raman spectrum of carbon nanotubes [17].

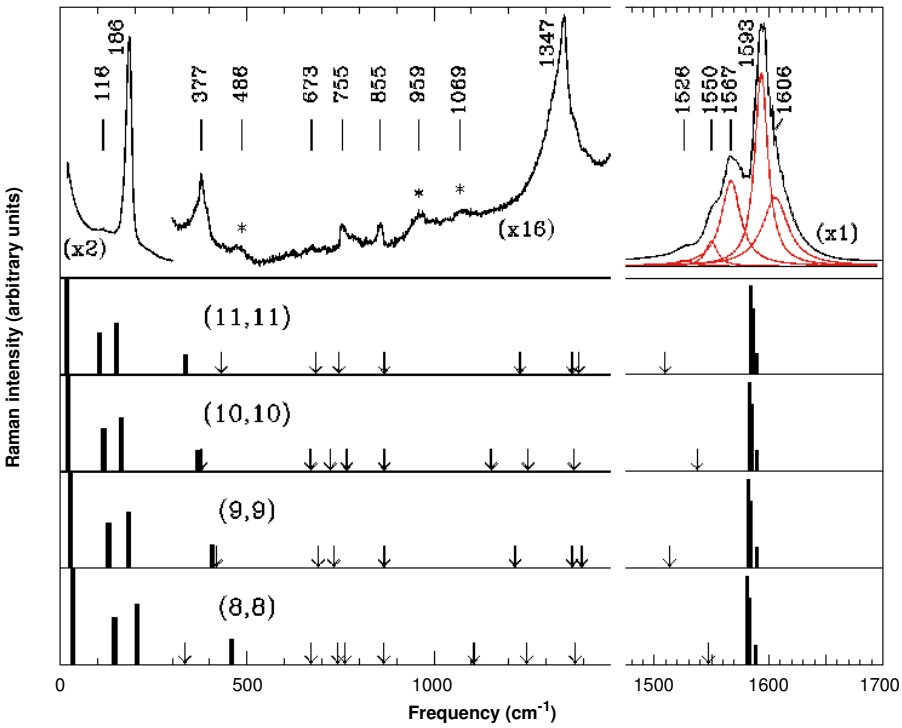

Figure 1.6: Raman spectrum of a sample containing randomly oriented carbon nanotubes. The four lower panels are the calculated Raman spectra for some armchair nanotubes ($n = 8, \ldots, 11$). The arrows indicate the positions of weaker Raman-active modes. (taken from Ref. [10]).

The Raman scattering signal of CNT is so large that even isolated tubes could be investigated.

Most of the Raman studies on single wall carbon nanotubes were made on nanotubes synthesized by the laser vaporization method with transition metal catalysts, or by the carbon arc method. In both methods, the nanotubes grow in a triangular lattice to form a bundle or 'rope' containing 10-50 nanotubes. Under some synthesis conditions, the (10,10) armchair nanotube is the dominant species in the rope. In general, the Raman samples have a narrow distribution of diameters and chiralities, which depend on the catalysts that are used.

Rao and coworkers have reported Raman spectra for single-walled CNTs in which they assigned the observed Raman modes with specific (n, m) nanotubes known to be present in the sample [10]. Figure 1.6 shows the measured Raman spectrum, taken on a sample containing microfiltered, randomly oriented single-walled CNTs dispersed in a KBr pellet. The spectra were collected in a backscattering geometry at room temperature with the 514.5 nm-laser incident at 45° with respect to the plane of the

pellet. They showed that the Raman signal from the rope not only consists of graphite-oriented modes, which occur around 1550 - 1600 cm^{-1}, but also contains a strong low-frequency mode, known as the nanotube radial breathing mode, which is special to the nanotube geometry. Furthermore the predicted diameter dependence of the mode frequencies can be easily observed, in particular in the low-frequency region.

The strongest low-frequency Raman mode is the radial breathing mode (RBM), whose frequency is around 186 cm^{-1} for the (10,10) CNT (see Fig. 1.6). Because of the strong dependence of the RBM frequency on nanotube diameter, the frequency of the RBM mode can be used as a marker for assigning the approximate diameter d_t of the carbon nanotube [18]. The RBM frequency quickly decreases to 0 cm^{-1} with increasing radius. We discuss later in Sec. 4.4 about the diameter dependence of the RBM. Other two modes were observed in the low frequency region, around 116 cm^{-1} and 377 cm^{-1}, but with lower intensities than the RBM mode. However, these are important since they also show a diameter dependence of their frequencies. Instead the Raman frequencies in the high frequency region, between 1550 cm^{-1} and 1600 cm^{-1}, do not vary much with nanotube diameter. They originate from an out-of-phase mode of graphite, and for this reason they are close to another. The intermediate Raman modes around 1200-1500 cm^{-1} give almost low intensity peaks. In Section 4.5 we visualize the seven strongest Raman modes.

Chapter 2

Classical theory of lattice dynamics

The aim of lattice dynamics is to set up and solve the equations of motion for the atoms in a crystal. To derive them we will use Hamiltonian mechanics, treating the atoms as point masses moving according to the laws of classical mechanics.

In this Chapter the formalism for solving the equations of motion for the displacement vectors is presented. For this purpose we introduce the Bloch theorem, which allows us to use the high symmetry of crystal structure to obtain analytical results as a function of the linear momentum. This reduces the order of the secular problem that one has to solve in order to obtain the normal modes. In particular we focus on the important concept of force-constant tensor and illustrate two different approaches to calculate it. We conclude this Chapter by calculating the normal modes of two archetypal systems, chosen as example: a one-dimensional linear chain of N atoms and a two-dimensional square lattice.

2.1 Crystal Hamiltonian

In order to describe a crystal and its properties one has to start from the general Hamiltonian of the solid, which is given by

$$\mathcal{H}_0 = \mathcal{H}_{\text{ion}} + \mathcal{H}_{\text{el}} + \mathcal{H}_{\text{el-ion}}. \tag{2.1}$$

Ions and electrons can be considered as two systems described respectively by the first and second term in the Hamiltonian $\mathcal{H}_0$, and they are in contact as mediated by $\mathcal{H}_{\text{el-ion}}$. The three terms are given by

$$\mathcal{H}_{\text{ion}} = \sum_{n=1}^{N_{\text{ion}}} \frac{\mathbf{P}_n^2}{2M_n} + \frac{1}{2} \sum_{\substack{n,m=1 \\ n \neq m}}^{N_{\text{ion}}} V(\mathbf{R}_n - \mathbf{R}_m), \tag{2.2a}$$

$$\mathcal{H}_{\text{el}} = \sum_{\ell=1}^{N_{\text{el}}} \frac{\mathbf{p}_\ell^2}{2m} + \frac{1}{2} \sum_{\substack{k,\ell=1 \\ k\neq\ell}}^{N_{\text{el}}} \frac{e^2}{4\pi\epsilon_0 |\mathbf{r}_\ell - \mathbf{r}_k|}, \tag{2.2b}$$

$$\mathcal{H}_{\text{el-ion}} = \sum_{\ell=1}^{N_{\text{el}}} \sum_{n=1}^{N_{\text{ion}}} v(\mathbf{r}_\ell - \mathbf{R}_n). \tag{2.2c}$$

Here we use $\mathbf{R}_n$, $\mathbf{P}_n$ and M_n for the coordinates, the momentum and the mass of the ions and analogously $\mathbf{r}_\ell$, $\mathbf{p}_\ell$ and m for the electrons. The potential $V(\mathbf{R}_n - \mathbf{R}_m)$ is the ion-ion interaction, while $v(\mathbf{r}_\ell - \mathbf{R}_n)$ gives the electron-ion interaction. The sums go over the hole number of ions, N_{ion}, or electrons, N_{el}, of the crystal. Starting from this Hamiltonian one has to solve the time-dependent Schrödinger equation

$$\mathcal{H}_0 \Psi = \mathrm{i}\hbar \frac{\partial}{\partial t} \Psi \tag{2.3}$$

where $\Psi = \Psi(\{\mathbf{r}_\ell\}; \{\mathbf{R}_n\})$ depends on the configuration of the electrons and ions.

2.1.1 Separating the motion of electrons and ions

To solve the Schrödinger equation (2.3) we consider the *Born-Oppenheimer approximation* [19], whose basic steps are briefly illustrated below, following Ref. [20,21]. The basic idea is to separate the motion of electrons and ions and then solve two distinct Schrödinger equations. The electrons are assumed to move in a stationary potential defined by any actual configuration of the ions. It is called also *adiabatic approximation* because the electrons follow the motion of the ions adiabatically, that means instantaneously without changing their eigenstate, which is the state of lowest energy. This assumption is justified by the mass ratio of $m/M \sim 10^{-4}$, indicating that the electrons move much faster than the ions.

Basically we consider a quantum mechanical system of N_{el} interacting electrons in a static potential generated by N_{ion} cores at fixed positions $\mathbf{R}_n$. It can be described by the stationary Schrödinger equation

$$(\mathcal{H}_{\text{el}} + \mathcal{H}_{\text{el-ion}})\psi_\alpha = \mathcal{E}_{\text{el},\alpha}\psi_\alpha \tag{2.4}$$

where α describes a complete set of quantum numbers. The core positions $\mathbf{R}_n$ enter only as parameter in the electronic wave functions $\psi_\alpha(\{\mathbf{r}_\ell\}; \{\mathbf{R}_n\})$ and in the energy eigenvalues $\mathcal{E}_{\text{el},\alpha}(\{\mathbf{R}_n\})$. For the ions one obtains the time dependent Schrödinger equation [20]:

$$(\mathcal{H}_{\text{ion}} + \mathcal{E}_{\text{el},\alpha})\varphi_\alpha = \mathrm{i}\hbar \frac{\partial}{\partial t} \varphi_\alpha \tag{2.5}$$

with

$$\mathcal{H}_{\text{ion}} + \mathcal{E}_{\text{el},\alpha} = \sum_{n=1}^{N_{\text{ion}}} \frac{\mathbf{P}_n^2}{2M_n} + \underbrace{\mathcal{E}_{\text{el},\alpha}(\{\mathbf{R}_n\}) + \frac{1}{2}\sum_{\substack{n,m=1 \\ n\neq m}}^{N_{\text{ion}}} V(\mathbf{R}_n - \mathbf{R}_m)}_{\mathcal{U}_\alpha(\{\mathbf{R}_n\}):\ \text{adiabatic potential energy}}. \tag{2.6}$$

The motions of the ions, described by the wave function $\varphi_\alpha(\{\mathbf{R}_n\})$, is therefore determined by the potential energy of the ion configuration and by the energy of the electron system in the eigenstate α. Commonly only the ground state $\mathcal{E}_{\text{el},0}$ is taken into account and the index α can be dropped, but since it is generally not possible to calculate the dependence of $\mathcal{E}_{\text{el},0}$ on the ion configuration, semiempirical models are chosen to determine the adiabatic potential.

In conclusion, to describe the dynamic of the crystal lattice one has consider the Hamiltonian

$$\mathcal{H} = \mathcal{H}_{\text{ion}} + \mathcal{E}_{\text{el}} = \sum_{n=1}^{N_{\text{ion}}} \frac{\mathbf{P}_n^2}{2M} + \mathcal{U}(\{\mathbf{R}_n\}). \tag{2.7}$$

2.1.2 Harmonic approximation

In the harmonic approximation the potential energy of a lattice ion is expanded in powers of the instantaneous displacement from its equilibrium position and only the first nonvanishing term is taken. To describe the ion configuration, characterized by the instantaneous location of the atoms, we use the following notation:

$$\mathbf{R}_{n,\tau}(t) = \mathbf{R}_{n,\tau}^{(0)} + \mathbf{u}_{n,\tau}(t) \tag{2.8}$$

Hence at time t the ion is located at $\mathbf{R}_{n,\tau}(t)$, while $\mathbf{R}_{n,\tau}^{(0)}$ is its equilibrium position, as denoted by the superscript "0". Since we want to develop a general model that can be applied also to crystals with more than one atom in the basis, we introduced also the index τ which characterizes every single atom of the basis. Now the equilibrium position of the ions is $\mathbf{R}_{n,\tau}^{(0)} = \mathbf{R}_n^{(0)} + \mathbf{R}_\tau^{(0)}$ where $\mathbf{R}_n^{(0)}$ denotes the Bravais lattice points or a suitable reference point inside the unit cell and $\mathbf{R}_\tau^{(0)}$ are the vectors from this point to the τth basis point. The index n therefore runs from 1 to the number N_u of Bravais lattice points (or unit cells) in the solid and τ runs from 1 to r for a basis made up of r atoms. Furthermore, $\mathbf{u}_{n,\tau}(t)$ are the time-dependent displacements around the equilibrium positions. Figure 2.1 shows an example of the introduced vectors.

At low enough temperature, as well as at high enough pressure, it is reasonable to assume that the atom displacements are small compared to the lattice spacings, so

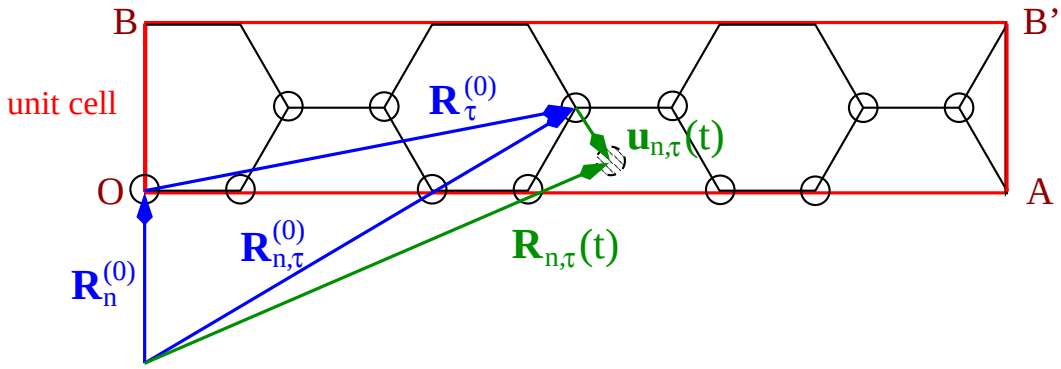

Figure 2.1: Coordinates of the ions shown at the example of the unit cell of a (3,3) CNT (O has to coincide with A and B with B', forming a finite size cylinder): the vector $\mathbf{R}_n^{(0)}$ points at a Bravais lattice point and the index n denotes the unit cell. The vector $\mathbf{R}_\tau^{(0)}$ points from the lattice point n to every single atom of the basis, thus the equilibrium position of the ions is $\mathbf{R}_{n,\tau}^{(0)} = \mathbf{R}_n^{(0)} + \mathbf{R}_\tau^{(0)}$. The index τ runs from 1 to r, the number of atoms per unit cell. In this example we have $r = 12$. The vector $\mathbf{R}_{n,\tau}(t)$ indicates the instantaneous positions of the ions and $u_{n,\tau}(t)$ their displacements.

that the ions move close around their equilibrium position. Under this condition, the adiabatic potential can be expanded in a Taylor series about the static positions $\mathbf{R}_{n,\tau}^{(0)}$:

$$\begin{aligned}\mathcal{U}(\{\mathbf{R}_{n,\tau}\}) &= \mathcal{U}(\{\mathbf{R}_{n,\tau}^{(0)}\}) + \sum_{n=1}^{N_u}\sum_{\alpha=1}^{3}\sum_{\tau=1}^{r} \left.\frac{\partial \mathcal{U}}{\partial R_{n,\tau,\alpha}}\right|_{\mathbf{R}_{n,\tau}^{(0)}} u_{n,\tau,\alpha} \\ &+ \sum_{n,m=1}^{N_u}\sum_{\alpha,\beta=1}^{3}\sum_{\tau,\tau'=1}^{r} \frac{1}{2} \left.\frac{\partial^2 \mathcal{U}}{\partial R_{n,\tau,\alpha}\partial R_{m,\tau',\beta}}\right|_{\mathbf{R}_{n,\tau}^{(0)},\mathbf{R}_{m,\tau'}^{(0)}} u_{n,\tau,\alpha}u_{m,\tau',\beta} \\ &+ \mathcal{O}(u^3) \end{aligned} \tag{2.9}$$

where $R_{n,\tau,\alpha}$ are the ion coordinates and α, β are Cartesian vector components. The first term in the expansion is the potential energy of the ion lattice in equilibrium. It does not contribute to the dynamics of lattice vibrations, which is our interest here, and thus can be dropped. The derivatives are evaluated with the atoms at their equilibrium position, which implies that the potential energy $\mathcal{U}(\{\mathbf{R}_{n,\tau}\})$ has its minimum and the first derivative vanishes. In the harmonic approximation terms of higher than second order are neglected, because they generate anharmonic, nonlinear responses (see Sec. 5.1). The inclusion of higher anharmonic terms in the expansion means an interaction between the phonons, but it is not topic in this work. Thus, the second order becomes the leading term and we can rewrite it defining a 3×3 tensor, whose

elements are

$$\Phi_{\alpha\beta}(\mathbf{R}^{(0)}_{n,\tau},\mathbf{R}^{(0)}_{m,\tau'}) = \left.\frac{\partial^2\mathcal{U}}{\partial R_{n,\tau,\alpha}\partial R_{m,\tau',\beta}}\right|_{\mathbf{R}^{(0)}_{n,\tau},\mathbf{R}^{(0)}_{m,\tau'}}. \tag{2.10}$$

It is called *force-constant tensor* or *interaction tensor* and couples pairs of atoms and is a function of their equilibrium positions. The translational symmetry of the lattice requires also that $\Phi_{\alpha\beta}$ does not depend on the two equilibrium positions separately, but only on their difference: $\Phi_{\alpha\beta}(\mathbf{R}^{(0)}_{n,\tau},\mathbf{R}^{(0)}_{m,\tau'})=\Phi_{\alpha\beta}(\mathbf{R}^{(0)}_{n,\tau}-\mathbf{R}^{(0)}_{m,\tau'})$. We will discuss later in Sec. 2.3 about the meaning and properties of the force constant tensor and show how to calculate it in some specific cases.

Summarizing we obtain a compact expression for the potential energy:

$$\begin{aligned}\mathcal{U}_{\text{harm}}(\mathbf{R}_1,\ldots,\mathbf{R}_N) &= \frac{1}{2}\sum_{n,m=1}^{N_u}\sum_{\alpha,\beta=1}^{3}\sum_{\tau,\tau'=1}^{r} u_{n,\tau,\alpha}\,\Phi_{\alpha\beta}(\mathbf{R}^{(0)}_{n,\tau}-\mathbf{R}^{(0)}_{m,\tau'})\,u_{m,\tau',\beta}\\ &= \frac{1}{2}\sum_{n,m=1}^{N_u}\sum_{\tau,\tau'=1}^{r}\mathbf{u}_{n,\tau}\cdot\Phi(\mathbf{R}^{(0)}_{n,\tau}-\mathbf{R}^{(0)}_{m,\tau'})\cdot\mathbf{u}_{m,\tau'}\end{aligned} \tag{2.11}$$

and the Hamiltonian (2.7) of the system is:

$$\mathcal{H} = \frac{1}{2}\sum_{n,\tau}M_\tau\left|\frac{\partial\mathbf{u}_{n,\tau}}{\partial t}\right|^2 + \frac{1}{2}\sum_{\substack{n,\tau,\alpha\\ m,\tau',\beta}} u_{n,\tau,\alpha}\,\Phi_{\alpha\beta}(\mathbf{R}^{(0)}_{n,\tau}-\mathbf{R}^{(0)}_{m,\tau'})\,u_{m,\tau',\beta}. \tag{2.12}$$

The equations of motion are a set of $3rN_u$ coupled second order differential equations for each component α of the atomic displacements:

$$M_\tau\frac{\partial^2 u_{n,\tau,\alpha}}{\partial t^2} = -\frac{\partial\mathcal{U}}{\partial u_{n,\tau,\alpha}} = -\sum_{m,\tau',\beta}\Phi_{\alpha\beta}(\mathbf{R}^{(0)}_{n,\tau}-\mathbf{R}^{(0)}_{m,\tau'})\,u_{m,\tau',\beta}. \tag{2.13}$$

The expression above represents the force in the α direction on the τth ion in the nth unit cell when the τ'th ion in the mth unit cell is displaced in the β direction.

2.2 Lattice normal modes

2.2.1 Bloch theorem and dynamical matrix

The solution of the coupled differential equations (2.13) is generally a very intricate mathematical problem, as it is of order $3rN_u$. Due to lattice periodicity it is possible to reduce the problem to a much lower order, $3r$, as we will see, where r is the number of atoms per unit cell: this is the essence of the Bloch theorem.

Due to the perfect periodicity of the crystal, we can choose the index n in Eq. (2.13) to be equal to zero without loosing in generality. Furthermore since the force-constant tensors depend on the cell indices n and m only through their difference (see Sec. 2.3), the Hamiltonian (2.12) commutes with the operator describing a rigid translation of the crystal through a lattice translation vector. It follows that the atomic displacements must simultaneously be eigenfunctions of the translation operator and the Hamiltonian [22]. This is what the Bloch theorem states: the spatial part $\phi(\mathbf{r})$ of a classical normal mode can be written so that under a real space lattice translation $\mathbf{R}$, taken from the set of lattice points $\{\mathbf{R}\}$, it transforms as

$$\phi(\mathbf{r}+\mathbf{R}) = \mathrm{e}^{\mathrm{i}\mathbf{q}\cdot\mathbf{R}}\phi(\mathbf{r}) \tag{2.14}$$

where q is the wave vector that specifies the spatial dependence of $\phi(\mathbf{r})$ and $e^{\mathrm{i}\mathbf{q}\cdot\mathbf{R}}$ are the eigenvalues of the translation operator. From this fact follows that the eigenfunctions can be written as a product of a plane wave and a function $f(\mathbf{r})$:

$$\phi(\mathbf{r}) = \mathrm{e}^{\mathrm{i}\mathbf{q}\cdot\mathbf{R}} f(\mathbf{r}) \tag{2.15}$$

where $f(\mathbf{r})$ has the periodicity of the Bravais lattice, $f(\mathbf{r}+\mathbf{R}) = f(\mathbf{r})$ for every vector $\mathbf{R}$ of the Bravais lattice. For further specifications and the proof of the theorem we refer to the book of Ashcroft and Mermin [22].

With the help of the Bloch theorem it is now possible to solve analytically the coupled equations (2.13). To do this we follow a standard formalism as described for example by Cleland [23] or Madelung [24]. Since we are searching for eigenmodes, all atoms must have the same frequency and therefore the normal modes have a functional dependence of the type

$$\mathbf{u}_{n,\tau}(t) = \mathbf{A}_{n,\tau}\,\mathrm{e}^{-\mathrm{i}\omega t} \tag{2.16}$$

where $\mathbf{A}_{n,\tau}$ gives the spatial dependence and $\mathrm{e}^{-\mathrm{i}\omega t}$ the harmonic time dependence. The general motion of the crystal will be a superposition of the harmonic motions, and in general is a non-periodic motion. We can now write the vector displacements $\mathbf{A}_{n,\tau}$ in Bloch form and obtain

$$\mathbf{u}_{n,\tau}(t) = \mathbf{A}_{\tau}\,\mathrm{e}^{\mathrm{i}\mathbf{q}\cdot\mathbf{R}_n^{(0)}}\mathrm{e}^{-\mathrm{i}\omega t}. \tag{2.17}$$

$\mathbf{A}_\tau$ gives the amplitude of the mode. Starting from now, we set $M_\tau \equiv M$, since we are interested in carbon nanotubes and there all the ions have the same mass. Inserting expression (2.17) in (2.13), the equation of motion for the τth atom in the nth unit cell becomes

$$\omega^2 M A_{\tau,\alpha} = \sum_{m,\tau',\beta} \Phi_{\alpha\beta}(\mathbf{R}_{n,\tau}^{(0)} - \mathbf{R}_{m,\tau'}^{(0)})\,\mathrm{e}^{\mathrm{i}\mathbf{q}(\mathbf{R}_m^{(0)}-\mathbf{R}_n^{(0)})} A_{\tau',\beta}. \tag{2.18}$$

We can rewrite this expression defining a new tensor $\mathsf{D}(\mathbf{q})$ as the Fourier transform of the force constant tensor. Its components are:

$$D^{\tau\tau'}_{\alpha\beta}(\mathbf{q}) = \frac{1}{M}\sum_{m=1}^{N_u} \Phi_{\alpha\beta}(\mathbf{R}^{(0)}_{n,\tau} - \mathbf{R}^{(0)}_{m,\tau'})\, \mathrm{e}^{\mathrm{i}\mathbf{q}(\mathbf{R}^{(0)}_m - \mathbf{R}^{(0)}_n)}. \tag{2.19}$$

It is called *dynamical matrix* and is hermitian. As one can see it does not depend on the index n of the unit cell. In a periodic system, the dynamical matrix elements are given by the product of the force constant tensor $\Phi(\Delta\mathbf{R}^{(0)}_{nm})$ and a phase difference factor $\mathrm{e}^{\mathrm{i}\mathbf{q}\cdot\Delta\mathbf{R}^{(0)}_{nm}}$. Now the equations of motion (2.13) can be written in the compact form

$$\omega_s^2 A_{\tau,\alpha} = \sum_{\tau'=1}^{r}\sum_{\beta=1}^{3} D^{\tau\tau'}_{\alpha\beta}(\mathbf{q})\, A_{\tau',\beta}. \tag{2.20}$$

Lattice periodicity has thus reduced the system of $3rN_u$ equations to a system of $3r$ equations. They form the following eigenvector-eigenvalue problem:

$$\omega_s^2 \begin{pmatrix} A_{1,x}\\ A_{1,y}\\ A_{1,z}\\ \hline A_{2,x}\\ A_{2,y}\\ A_{2,z}\\ \hline \vdots\\ \vdots\\ \hline A_{r,x}\\ A_{r,y}\\ A_{r,z} \end{pmatrix} = \left(\begin{array}{ccc|ccc|c|c} D^{11}_{xx} & D^{11}_{xy} & D^{11}_{xz} & D^{12}_{xx} & D^{12}_{xy} & D^{12}_{xz} & \cdots & \cdots\\ D^{11}_{yx} & D^{11}_{yy} & D^{11}_{yz} & D^{12}_{yx} & D^{12}_{yy} & D^{12}_{yz} & \cdots & \cdots\\ D^{11}_{zx} & D^{11}_{zy} & D^{11}_{zz} & D^{12}_{zx} & D^{12}_{zy} & D^{12}_{zz} & \cdots & \cdots\\ \hline D^{21}_{xx} & D^{21}_{xy} & D^{21}_{xz} & \cdots & \cdots & \cdots & \cdots & \cdots\\ D^{21}_{yx} & D^{21}_{yy} & D^{21}_{yz} & \cdots & \cdots & \cdots & \cdots & \cdots\\ D^{21}_{zx} & D^{21}_{zy} & D^{21}_{zz} & \cdots & \cdots & \cdots & \cdots & \cdots\\ \hline \cdots & \cdots & \cdots & \cdots & \cdots & \cdots & \cdots & \cdots\\ \cdots & \cdots & \cdots & \cdots & \cdots & \cdots & \cdots & \cdots\\ \hline D^{r1}_{xx} & D^{r1}_{xy} & D^{21}_{rz} & \cdots & \cdots & \cdots & \cdots & \cdots\\ D^{r1}_{yx} & D^{r1}_{yy} & D^{21}_{rz} & \cdots & \cdots & \cdots & \cdots & \cdots\\ D^{r1}_{zx} & D^{r1}_{zy} & D^{21}_{rz} & \cdots & \cdots & \cdots & \cdots & \cdots \end{array}\right) \begin{pmatrix} A_{1,x}\\ A_{1,y}\\ A_{1,z}\\ \hline A_{2,x}\\ A_{2,y}\\ A_{2,z}\\ \hline \vdots\\ \vdots\\ \hline A_{r,x}\\ A_{r,y}\\ A_{r,z} \end{pmatrix}. \tag{2.21}$$

The dynamical matrix is a hermitian and positive definite matrix and therefore its eigenvalues ω_s^2 are real and positive. In order that the system is stable in the harmonic approximation ω_s must be real, because an imaginary frequency corresponds to atomic motions whose amplitudes depend exponentially on the time.

For each $\mathbf{q}$ there are $3r$ eigenfrequencies $\omega_s(\mathbf{q}) = \omega_s(-\mathbf{q})$, $s = 1, \ldots, 3r$. For each ω_s Eq. (2.20) has a solution $A_{\tau,\alpha} = a^s_{\tau,\alpha}(\mathbf{q})$. These solutions can be combined to vectors as in (2.21). They are defined except for a common factor which can be chosen such that the $\mathbf{a}^s_\tau(\mathbf{q})$ are normalized and orthogonal to each other. For the displacements we then have:

$$\mathbf{u}^s_{n,\tau}(\mathbf{q},t) = \mathbf{a}^s_\tau(\mathbf{q})\, \mathrm{e}^{\mathrm{i}(\mathbf{q}\cdot\mathbf{R}^0_n - \omega_s(\mathbf{q})t)}. \tag{2.22}$$

They form a complete set of solutions, called normal modes, that can be used as basis for representing an arbitrary motion of the lattice. The function $\omega(\mathbf{q})$ is periodic in $\mathbf{q}$-space, so we need to consider only one Brillouin zone, consisting of exactly N_u values of $\mathbf{q}$. Since s can take $3r$ values, there are at most $3rN_u$ different $\omega_s(\mathbf{q})$, as many as the crystal has internal degrees of freedom.

2.2.2 Boundary conditions

Up to now we considered an infinite system where any equivalent atom has the same nearest neighbor configuration, neglecting the fact that atoms at the edge of the crystal have less number of neighbors and therefore need a special treatment. This presents a disturbing aspect and creates only difficulties in the analysis. Boundary conditions simplify the mathematics considerably without influencing significantly the physics of the problem. They work very well in large systems, where the typical wavelengths are much smaller than the solid dimensions and thus surface effects become irrelevant. We will consider the case of periodic and of fixed boundary conditions.

In case of periodic boundary conditions, the motion in each point is assumed to be identical to that at a repeated point at the distance L away, where L is the size of the crystal [22]. We make this assumption under the condition that the macroscopic properties of the crystal do not change. For our purpose it is useful to take a periodicity volume that is commensurate with a unit cell of the crystal. If $\mathbf{a}_i$ $(i = 1, 2, 3)$ are the lattice unit vectors, the size of the crystal in this directions is $L_i = N_i a_i$. Here N_i denotes the number of Bravais lattice points that one passes going for a distance L_i in direction $\mathbf{a}_i$. The periodic boundary condition reads then:

$$\phi(\mathbf{r} + N_i\mathbf{a}_i) = \phi(\mathbf{r}), \qquad i = 1, 2, 3. \tag{2.23}$$

Here $\phi(\mathbf{r})$ indicates general crystal variables, as for example the spatial part of a classical normal mode or a quantum mechanical energy eigenstate. $N_u = N_1N_2N_3$ is the number of unit cells in the crystal. Now applying the Bloch theorem (2.15) on Eq. (2.23) one obtains that the wave vector $\mathbf{q}$ can take only discrete values in $\mathbf{q}$ space [22]. In the direction $\mathbf{a}_i$ they are

$$q_i = \frac{2\pi}{L_i}m = \frac{2\pi}{a_i}\frac{m}{N_i}, \qquad -\frac{N_i}{2} \leq m \leq \frac{N_i}{2}. \tag{2.24}$$

The number of allowed $\mathbf{q}$ vectors in one Brillouin zone is equal to the number of unit cells N_u in real space lattice.

For many purposes the most realistic boundary conditions are to fix the ends of the lattice to rigid supports. This is the case of fixed boundary conditions. The solutions

are now standing waves, given by the superposition of the left- and right-going waves found in the case of periodic boundary conditions. From the condition that the walls do not move, $u_{\text{walls}} = 0$, one obtains the restriction for the wave vectors. The $\mathbf{q}$ vectors are again discretized but not with the same values as in periodic boundary conditions:

$$q_i = \frac{\pi}{a_i} \frac{m}{(N_i + 1)}, \qquad 0 < m < N_i + 1. \tag{2.25}$$

In Sec. 2.4.1 we will show it on the example of the linear chain.

It is clear that each lattice with fixed boundary conditions is naturally embedded in configurations of a system with periodic boundary conditions. Other than the restriction for the wave vector, the force constant tensors and the equations of motion are the same as for an infinite solid; we will therefore ignore the discretized values for the wave vector and assume that $\mathbf{q}$ can be treated as a continuous vector.

2.3 The force-constant tensor

The concept of force-constant tensor is of central importance within the model approach of calculating normal modes. We introduced it as the second derivative of the interaction energy at equilibrium:

$$\Phi_{\alpha\beta}(\mathbf{R}^{(0)}_{n,\tau} - \mathbf{R}^{(0)}_{m,\tau'}) = \left. \frac{\partial^2 \mathcal{U}}{\partial R_{n,\tau,\alpha} \partial R_{m,\tau',\beta}} \right|_{\mathbf{R}^{(0)}_{n,\tau}, \mathbf{R}^{(0)}_{m,\tau'}} . \tag{2.26}$$

The derivatives are taken with respect to the components of the atomic displacements and evaluated with the atoms at their equilibrium position. Since the form of the force constant tensor depends strictly on the potential that we choose, it reflects the characteristics of the different models and presents a valid possibility to compare them among each other. The name is justified by the fact that in the force constant model the atom interactions are symbolized by springs that couple pairs of atoms. Every entry $\Phi_{\alpha\beta}$ gives the spring force constant acting on the atom at $\mathbf{R}^{(0)}_{n,\tau}$ in direction α when the atom at $\mathbf{R}^{(0)}_{m,\tau'}$ is shifted in direction β.

2.3.1 General properties

Apart from specific features characterizing a special lattice, the force constants are subjected to a number of general restrictions resulting from certain invariance conditions every solid must obey. In particular they are linked by a large number of symmetry relations, which greatly simplify the calculations. Here we consider only the most relevant ones.

As we already mentioned, due to the invariance of the lattice under translation it follows:

$$\Phi_{\alpha\beta}(\mathbf{R}^{(0)}_{n,\tau}, \mathbf{R}^{(0)}_{m,\tau'}) = \Phi_{\alpha\beta}(\mathbf{R}^{(0)}_{n,\tau} - \mathbf{R}^{(0)}_{m,\tau'}). \tag{2.27}$$

According to Newton's third axiom (*actio=reactio*) the tensor Φ is inversion symmetric in its variables, which means:

$$\Phi_{\alpha\beta}(\mathbf{R}^{(0)}_{n,\tau} - \mathbf{R}^{(0)}_{m,\tau'}) = \Phi_{\alpha\beta}(-(\mathbf{R}^{(0)}_{n,\tau} - \mathbf{R}^{(0)}_{m,\tau'})). \tag{2.28}$$

It is symmetric in its indices:

$$\Phi_{\alpha\beta}(\mathbf{R}^{(0)}_{n,\tau} - \mathbf{R}^{(0)}_{m,\tau'}) = \Phi_{\beta\alpha}(\mathbf{R}^{(0)}_{n,\tau} - \mathbf{R}^{(0)}_{m,\tau'}). \tag{2.29}$$

If the displacements $\mathbf{u}_{m,\tau'}$ are the same for all the atoms m, τ', the crystal is only translated and the potential energy does not change. This means that $\partial\mathcal{U}/\partial u_{n,\tau,\alpha} = 0$ and according to Eq. (2.13) it follows:

$$\sum_{m,\tau',\beta} \Phi_{\alpha\beta}(\mathbf{R}^{(0)}_{n,\tau} - \mathbf{R}^{(0)}_{m,\tau'})\, u_\beta = 0 \qquad \text{for any } u_\beta \tag{2.30}$$

so that for every $\alpha\beta$ tensor element holds:

$$\sum_{m,\tau'} \Phi_{\alpha\beta}(\mathbf{R}^{(0)}_{n,\tau} - \mathbf{R}^{(0)}_{m,\tau'}) = 0. \tag{2.31}$$

This is an important rule called *acoustic sum rule*, which has always to be fulfilled. It is a good method to verify the correctness of the calculations of the force constant tensors or also a practical method to determine the self-interaction terms $\Phi_{\alpha\beta}(0)$ of the dynamical matrix.

2.3.2 Model approaches

A practical method of investigating vibrational properties is to use an empirical force-constant model. The approach is based on a microscopic examination of the forces between the ions and on the idea that the motion of the atoms in a solid is governed by spring-like harmonic force constants. In model approaches one assumes an analytic expression for the interaction energy of two or more atoms, and then calculates the force constants as a function of the parameters involved in this expression. Thus, the crucial point is to construct an appropriate analytical form for the potential energy of a crystal, which mimics the behavior of the "true" potential in realistic way for specific lattices taken in consideration. It is subjected to various physical requirements: some

general conditions, such as rotational and translational invariance, and those imposed by the symmetry of the crystal. In a simple approximation it is almost a sum of pairwise terms, with the energy of a pair of atoms depending on their relative distance.

In the attempt to capture as much as possible the physics and chemistry of the bonding, it is necessary to introduce interaction-energy terms that involve more than two atoms. In fact a single spring can simulate a bond successfully only if the bonding forces are central, as in ionic crystals. For a lattice based on covalent bonds the bonding forces are directional and therefore depend on the bond angle. Such forces can be described only by more than one spring, in particular angular springs are needed. A typical analytical form for the interaction energy is constituted by a number of functions, depending on geometrical quantities such as distances or angles, or on other variables such as atom coordinations. Another important aspect is that bonding forces do not act only between nearest neighbor atoms. In principle they must also be considered to involve even atoms which are far apart. The experimental results can be reproduced as closely as possible by increasing the number of the force constants. This improves the results considerably but introduces more and more parameters in the calculations, deviating from the purpose to find a successful model with a small number of parameters. One has to find a balance between taking the minimal number of parameters and still reproducing satisfactory results.

In Section 2.4.2 we illustrate the importance of the choice of the potential making a comparison between different potentials shown on the example of the square lattice. In Chapter 3 and 4 we will see that systems such as graphene or carbon nanotubes require a more sophisticated approach, with the inclusion of interaction-energy terms involving more than two atoms.

2.3.3 *Ab-initio* approach

The first-principles or *ab-initio* approach is a method based on quantum-mechanical theory that does not rely on input from experimental informations. The basic idea is to determine the interatomic force constants through the total energy of a crystal with frozen nuclear coordinates. For this purpose the quantum-mechanical problem including all electrons and nuclei has to be solved. Starting point is again the Born-Oppenheimer approximation: The remaining many-particle problem of interacting valence electrons, which feel the field of the ionic cores, can be simplified by means of the density-functional theory (DFT). This is a method for finding the ground state properties of the Schrödinger equation of a many-body system. The central idea is to express the electronic energy as a functional $E[n(\mathbf{r})]$ of the single-particle density

$n(\mathbf{r})$, which is minimal only if $n(\mathbf{r})$ equals the ground-state density $n_0(\mathbf{r})$ of the electrons. Kohn and Sham have found an expression for $E[n(\mathbf{r})]$ by mapping the interacting many-electron system into a system of noninteracting electrons moving in an effective potential [25]. The ground-state electron density is obtained from the solution of a set of self-consistent coupled single-particle equations which are known as Kohn-Sham equations.

There are two commonly used approaches based on DFT: The so-called *frozen phonon* method and the *perturbative* approach [26]. The former consists of the computation of the total energy as a function of atomic displacements. A distorted crystal is treated as a crystal in a new structure with a lower symmetry than the undistorted one. The electronic energy of the crystal can be computed as a function of a suitably chosen phonon coordinate and used for dealing with both the undistorted and the perturbed crystal. The interatomic force constants can be obtained by numerical differentiation of the calculated energy. Unfortunately, symmetry reduction due to perturbation increases drastically the computational effort. To retain partial symmetry one uses displacements corresponding to superstructures, which restricts the practical application of the method to phonons with high-symmetry wave vectors. For the investigation of phonons not only at the zone center, it is necessary to use larger unit cells for a proper description of the periodicity according to the wave vector. This is the main disadvantage of the frozen phonon approach.

The use of supercells can be avoided employing the perturbative approach to the DFT. This generalization is called density-functional perturbation theory (DFPT) [27]. Within the Born Oppenheimer approximation, lattice distortions associated with a phonon can be regarded as static perturbations acting on the electrons. It can be shown that the determination of the force acting on the atoms only requires the calculation of the electronic ground state density for a given configuration of atoms. This allows to determine the electronic contribution to the interatomic force constants. Moreover, the linear variation of the electronic density upon a static external perturbation allows to calculate the change in the total energy up to second order. Hence, the harmonic force constants can be calculated by combining DFT with first-order perturbation theory. This procedure results in a system of coupled equations that should be solved self-consistently. The DFPT theory allows to calculate the dynamical matrices on a fine grid of wave vectors in the Brillouin zone by using the same unit cell as in the ground-state calculations. Thus, it is possible to determine complete phonon dispersion curves.

In conclusion, comparing the force-constant-model approach with the *ab initio* method, one can state that the former provides a fast method for obtaining phonon dispersion curves even for complex systems of considerable size. However, such models are

Figure 2.2: The one dimensional linear chain of N atoms connected by springs. On the left it is shown with periodic boundary condition and on the right with fixed boundary conditions (taken from Ref. [23]).

an *a posteriori* construct: Their predictive power is limited to those systems which are already partially known from experiments, and even in these cases the predictions for the unknown properties are not very reliable. The advantage consists in its simplicity as compared to quantum mechanical computational efforts of *ab initio* calculations.

2.4 Archetypal examples

In this Section we want to show on minimal archetypal examples few concepts which are central in the physics of carbon-nanotube lattice dynamics. Namely, we will show the emergence of q^2-dependent normal modes (also called flexural modes) and the need to generalize nearest-neighbor bond-stretching models.

2.4.1 The one-dimensional linear chain of N atoms

After presenting above a general formalism to get an expression of the equations of motion and to solve them, we now show how to find the normal modes of a simple system, a one-dimensional linear chain of N atoms. We will see that solving directly Eq. (2.13) leads to an N-dimensional linear system which is not pleasant to solve, but considering the translational symmetry of the system and using the Bloch theorem one can greatly simplify the purpose.

In the linear chain all the atoms have mass M and are connected to their nearest neighbors by massless springs with force constant k and equilibrium length r_0, as shown in Fig. 2.2. In the force-constant models the bonds between atoms are represented by springs and therefore the diatomic interaction is given by the spring potential energy $\mathcal{U}_{\text{spring}} = k(u_n - u_{n+1})^2/2$, where u_n is the displacement of the nth atom. Summing

over N atoms, for the whole chain we obtain

$$\mathcal{U} = \frac{1}{2} \sum_{\substack{\text{all} \\ \text{springs}}} \mathcal{U}_{\text{spring}} \tag{2.32}$$

and Newton's equation of motion (2.13) for the nth atom becomes:

$$M\ddot{u}_n = k(u_{n+1} - 2u_n + u_{n-1}). \tag{2.33}$$

In this simple example one can clearly see the meaning of the force constant tensor (2.10), which is 1×1 because of the one-dimensionality of the system. Comparing the above expressions with Eq. (2.13) one can see that for the nth atom the tensor is $\Phi(R_n^{(0)} - R_{n+1}^{(0)}) = \Phi(R_n^{(0)} - R_{n-1}^{(0)}) = -k$ and $\Phi(R_n^{(0)} - R_n^{(0)}) = \Phi(0) = 2k$, representing respectively the force constant of the springs connecting it with the two nearest neighbor atoms and a self-interaction constant, given by the fact that in a harmonic oscillation the force on a mass is direct proportional to its own displacement.

For a chain with a finite number of atoms one has to consider also the special case of the atoms 1 and N, that form the end of the chain. We can suppose that they interact only with one neighbor atom, but as discussed in Sec. 2.2.2 the best solution is to introduce boundary conditions.

2.4.1.1 Periodic boundary conditions

In the case of the linear chain applying periodic boundary conditions means that we connect the first and last atom by a spring of the same type as inside the chain. The chain becomes a ring, but the system remains still one-dimensional. The condition to describe it mathematically is $u_1 = u_{N+1}$, or $u_0 = u_N$. Since we are searching for eigenmodes, all atoms must have the same frequency. Now to solve Eq. (2.33) we make the *Ansatz*

$$u_n = A_n \, \mathrm{e}^{-\mathrm{i}\omega t}. \tag{2.34}$$

A_n is the time independent amplitude of atom n. This leads to the eigenvector-eigenvalue problem:

$$\left(\frac{\omega}{\omega_0}\right)^2 \begin{pmatrix} A_1 \\ A_2 \\ A_3 \\ \vdots \\ \vdots \\ A_N \end{pmatrix} = \begin{pmatrix} 2 & -1 & & & & -1 \\ -1 & 2 & -1 & & & \\ & -1 & 2 & \ddots & & \\ & & \ddots & \ddots & \ddots & \\ & & & \ddots & \ddots & -1 \\ -1 & & & & -1 & 2 \end{pmatrix} \begin{pmatrix} A_1 \\ A_2 \\ A_3 \\ \vdots \\ \vdots \\ A_N \end{pmatrix} \tag{2.35}$$

with $\omega_0^2 = k/M$. It is an N-dimensional linear system and not very convenient to solve. But according to the Bloch Theorem, the amplitudes on different lattice sites differ only by a phase factor: $A_n = A\,\mathrm{e}^{\mathrm{i}qr_n}$ where A is the overall amplitude and $r_n = nr_0$ the equilibrium position of the nth atom. The spatial dependence of the modes is sinusoidal with wave vector q. Thus we search for normal modes that have the form

$$u_n = A\,\mathrm{e}^{\mathrm{i}qr_n}\,\mathrm{e}^{-\mathrm{i}\omega t}. \tag{2.36}$$

The boundary condition $u_0 = u_N$ imposes that $\mathrm{e}^{\mathrm{i}qNr_0} = 1$, so that q assumes discrete values given by

$$q_m = \frac{2\pi}{r_0}\frac{m}{N} \tag{2.37}$$

where m is an integer. Inserting the *Ansatz* (2.36) in Eq. (2.33) we will get the eigenfrequencies ω_m as a function of the wave vector q_m:

$$\omega_m = \omega_0\sqrt{2 - 2\cos q_m r_0} = 2\omega_0\left|\sin\frac{q_m r_0}{2}\right|. \tag{2.38}$$

In Figure 2.3 the solution is plotted for q in the range $-\pi/r_0 \leq q \leq \pi/r_0$. Values of q out of this range do not represent physically different solutions and can be neglected [23]. This means that the index m goes from $-N/2$ to $N/2$ so that there are exactly N values for q that give distinct solutions. Instead q changes continuously only in the limit of a chain composed by an infinite number of atoms.

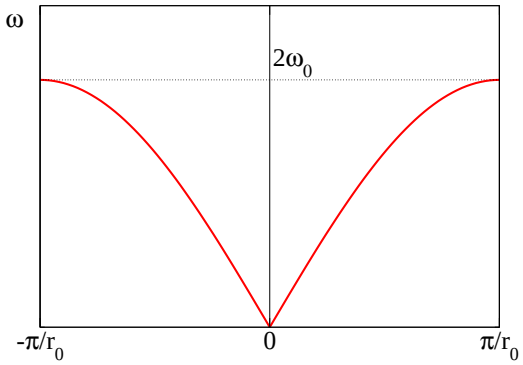

Figure 2.3: The dispersion relation of the one dimensional linear chain consists of an acoustic mode. It is plotted without considering the discreteness of the wave vector and for $\omega_0 = \sqrt{k/M}$. At long wavelengths ($q \to 0$) the frequency is linear in q.

The effective atomic displacements are given by the real- or imaginary part of expression (2.36), thus the normal modes are characterized by an oscillatory behavior. A special case arises when $m = 0$ because it follows that $q = 0$: the displacements of all the atoms have same amplitude and direction, so it represents an infinite wavelength "oscillation" or a translation mode of the whole crystal. Due to the translation invariance of $\mathcal{U}$ this mode has zero frequency.

2.4.1.2 Fixed boundary conditions

Let us consider the same chain as before, but now the first and last atom (1 and N) are constrained to two rigid walls, as shown in Fig. 2.2. The restriction imposes that $u_0 = u_{N+1} = 0$, in fact this are the displacements of the rigid walls and they are obviously not dynamical variables. The equations of motion read

$$\begin{cases} M\ddot{u}_1 &= k(u_2 - 2u_1), \\ M\ddot{u}_n &= k(u_{n+1} - 2u_n + u_{n-1}), \quad \text{for } n = 2, \ldots, N-1 \\ M\ddot{u}_N &= k(u_{N-1} - 2u_N). \end{cases} \tag{2.39}$$

and a simple *Ansatz* $u_n = A_n \, \mathrm{e}^{-\mathrm{i}\omega t}$ gives the N-dimensional linear system:

$$\left(\frac{\omega}{\omega_0}\right)^2 \begin{pmatrix} A_1 \\ A_2 \\ A_3 \\ \vdots \\ \vdots \\ A_N \end{pmatrix} = \begin{pmatrix} 2 & -1 & & & & 0 \\ -1 & 2 & -1 & & & \\ & -1 & 2 & \ddots & & \\ & & \ddots & \ddots & \ddots & \\ & & & \ddots & \ddots & -1 \\ 0 & & & & -1 & 2 \end{pmatrix} \begin{pmatrix} A_1 \\ A_2 \\ A_3 \\ \vdots \\ \vdots \\ A_N \end{pmatrix}. \tag{2.40}$$

Also in this case it is much more convenient to apply the Bloch Theorem, but taking into consideration that the solutions will be standing waves, which means a superposition of the travelling waves of Eq. (2.36). Thus the new *Ansatz* is

$$u_n = A \sin(qnr_0) \, \mathrm{e}^{-\mathrm{i}\omega t}. \tag{2.41}$$

Inserting it into the equations (2.40) we find the same relation $\omega_m(q_m)$ as in the case of periodic boundary conditions, see Eq. (2.38). We obtain also a condition for the wave vector q:

$$q_m = \frac{\pi}{(N+1)r_0} m, \qquad 1 \leq m \leq N. \tag{2.42}$$

The values of q are still discrete but in the range $\frac{\pi}{(N+1)r_0} \leq q \leq \frac{\pi N}{(N+1)r_0}$. The index m assumes positive values because we consider only standing waves with positive wave vector q. Those with negative wave vector are physically equal. The special case of $m = 0$ is excluded because it is not of physical interest: we can not have a translation as in the case of periodic boundary conditions, in fact for $q = 0$ the displacements are $u_n = 0$, and this represents a chain without movement.

Summarizing the expression for the dispersion relation is $\omega_m = 2\omega_0 \left|\sin(q_m r_0/2)\right|$ (illustrated in Fig. 2.3) for both an infinite chain[1] and a chain with boundary conditions.

[1] Or a chain with open boundary conditions

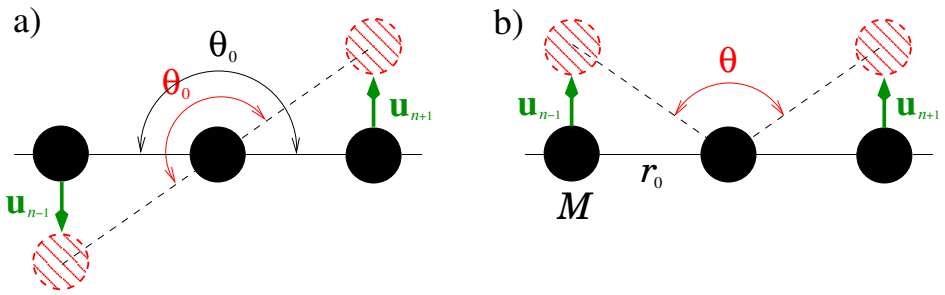

Figure 2.4: Bending forces in a linear chain. Panel (a): A displacement from equilibrium position which does not change the bond angle $\Theta_0 = \pi$. In this case the bending potential $\mathcal{U}$ of Eq. (2.43) is equal to zero. Panel (b): A displacement which changes the equilibrium bond angle. Now $\mathcal{U} > 0$, which means that there is a bending force acting.

To introduce boundary conditions has the effect of discretizing the values of the wave vector q.

2.4.1.3 A minimal model for flexural modes

With the stretching potential of Eq. (2.32) we obtained a dispersion relation with linear q dependence for long wavelengths. Now we want to clarify the nature of modes with q^2 dependence, as it emerges e.g. in the so-called flexural modes. We will show the importance of bond-bending forces and how these are correlated to the flexural modes.

So far we considered a stretching potential which is responsible for variations of the bond lengths, while it preserves the equilibrium bond angles between neighboring atoms. Now we consider another type of potential, which acts in case of variation of bond angles. The corresponding atomic displacements, which are due to bond-bending forces, are illustrated in Fig. 2.4 (panel (b)). A possible bending potential describing such a motion, where the atoms move perpendicular to the direction of the chain, is:

$$\mathcal{U} = \frac{k}{2} \sum_{n=1}^{N-1} (u_{n+1} + u_{n-1} - 2u_n)^2. \tag{2.43}$$

We solve the corresponding equations of motion with the same *Ansatz* as in Eq. (2.36) and obtain the following expression:

$$\omega^2 = \frac{k}{M} \left[6 - 8\cos(qr_0) + 2\cos(2qr_0)\right]. \tag{2.44}$$

After expanding the right hand side in a Taylor series with respect to qr_0 and taking the square root, we finally obtain:

$$\omega = \sqrt{\frac{k}{M}} r_0^2 \, q^2 \tag{2.45}$$

which shows the expected quadratic dependence that is typical of the flexure modes. It becomes also clear why the modes with q^2 dependence are called flexural modes: the atoms move in a direction perpendicular to the direction of the wave vector and the system makes transversal bending oscillations. This proves that bending forces, flexural modes and a quadratic dispersion are strictly correlated. It will be relevant when dealing later with carbon nanotubes.

2.4.2 The square lattice

Before we consider the normal modes of graphene and carbon nanotubes, we draw attention to a few important points by taking the simple case of a two-dimensional square lattice, as shown in Fig. 2.5. To do this we choose three different diatomic interaction potentials and then compare the results.

2.4.2.1 Lennard Jones potential

First nearest-neighbor approximation

A very simple model for diatomic interaction is the Lennard Jones model, which couples pairs of atoms through the Van der Waals interaction and depends only on their distance R. The atoms interact with one another only pairwise through a spherically symmetric potential:

$$\varphi(R) = -2A\left(\frac{r_0}{R}\right)^6 + A\left(\frac{r_0}{R}\right)^{12} \tag{2.46}$$

where the parameter A is the depth of the potential minimum at the equilibrium spacing r_0. The attractive term $1/R^6$ is characteristic of the van der Waals interaction, while the repulsive term $1/R^{12}$ is somewhat phenomenological. The total potential energy is then the sum over all atom pairs:

$$\mathcal{U}_{\mathrm{LJ}}(\mathbf{R}_1, \ldots, \mathbf{R}_N) = \sum_{\substack{n,m=1 \\ m>n}}^{N} \varphi(\mathbf{R}_n - \mathbf{R}_m). \tag{2.47}$$

The clause $m > n$ has the purpose of considering each atom pair only once. In a first approach we consider only nearest-neighbor interactions, as in Ref. [23], so an atom situated at $\mathbf{R}_n$ interacts only with those at $\mathbf{R}_n \pm r_0\widehat{\mathbf{x}}$ and $\mathbf{R}_n \pm r_0\widehat{\mathbf{y}}$. The 2×2 force constant tensor can be calculated taking $\mathcal{U}_{\mathrm{LJ}}$ and evaluating Eq. (2.10). Due to the translation invariance of the system, the tensor is the same for all other atoms. We obtain:

$$\Phi(r_0\widehat{\mathbf{x}}) = \Phi(-r_0\widehat{\mathbf{x}}) = -\frac{A}{r_0^2}\begin{pmatrix} 72 & 0 \\ 0 & 0 \end{pmatrix} \tag{2.48}$$

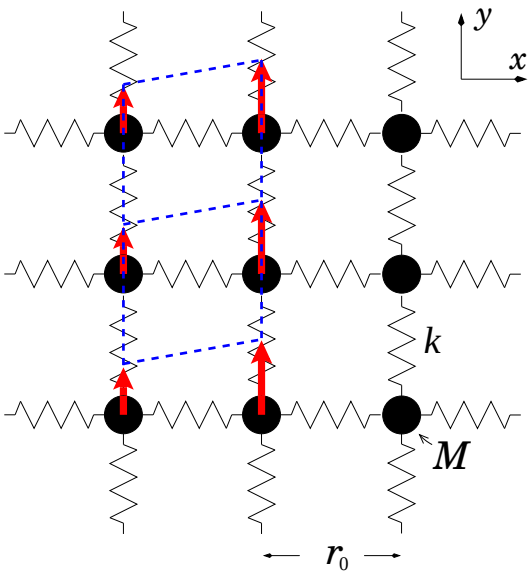

Figure 2.5: Two dimensional square lattice of atoms of mass M connected by springs with force constant k. We illustrate a special case that happens in the Lennard Jones model for $q_y = 0$ and $\omega_2 = 0$. The displacements of the atoms along the y direction, indicated by the red arrows, have zero frequency and thus do not cost energy. The system is instable against shear strain along the y axis, as indicated by the dotted blue lines.

$$\Phi(r_0\widehat{\mathbf{y}}) = \Phi(-r_0\widehat{\mathbf{y}}) = -\frac{A}{r_0^2}\begin{pmatrix} 0 & 0 \\ 0 & 72 \end{pmatrix} \tag{2.49}$$

$$\Phi(0) = \frac{A}{r_0^2}\begin{pmatrix} 144 & 0 \\ 0 & 144 \end{pmatrix}. \tag{2.50}$$

We note that the force constant tensor is identical to that found if the atoms are coupled by springs with spring constant $k = 72\,A/r_0^2$. The dynamical matrix can be calculated through Eq. (2.19):

$$\mathsf{D}(q_x, q_y) = 4k\begin{pmatrix} \sin^2(\frac{q_x r_0}{2}) & 0 \\ 0 & \sin^2(\frac{q_z r_0}{2}) \end{pmatrix}. \tag{2.51}$$

q_x and q_y are the components of $\mathbf{q}$ in the (two-dimensional) Brillouin zone. For the two-dimensional square lattice this is itself a square of side length $2\pi/r_0$. The dynamical matrix is almost diagonal so the eigenfrequencies can be easily obtained taking the square root of the entries and multiplying them by $1/\sqrt{M}$:

$$\omega_1(\mathbf{q}) = 2\omega_0\left|\sin(\frac{q_x r_0}{2})\right| \tag{2.52}$$

$$\omega_2(\mathbf{q}) = 2\omega_0\left|\sin(\frac{q_y r_0}{2})\right| \tag{2.53}$$

with $\omega_0 = \sqrt{k/M} = \sqrt{72A/(r_0^2 M)}$. These correspond to the two branches possible in the two-dimensional Bravais lattice. The result is analogous to that obtained for the linear chain, see Eq. (2.38). Figure 2.6 shows a plot for one Brillouin zone. The

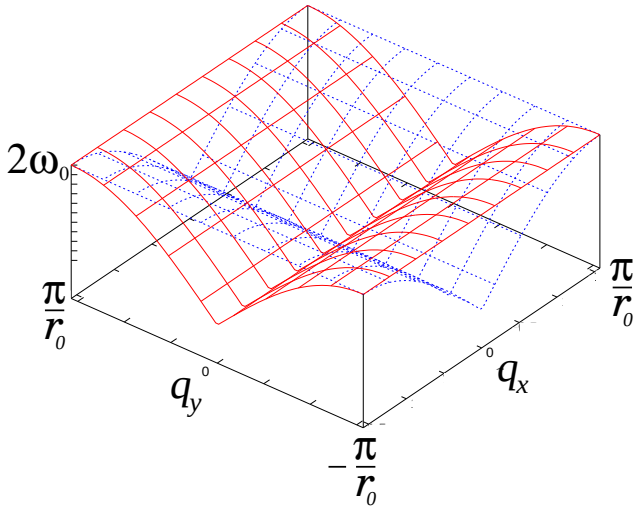

Figure 2.6: Dispersion curve for a two dimensional square lattice in the Lennard Jones model including first nearest neighbors. Here $\omega_0 = \sqrt{k/M}$ with $k = 72\,A/r_0^2$. The system is instable because for the whole lines $q_y = 0$ and $q_x = 0$ one of the two branches has zero frequency.

eigenvectors are $\mathbf{A}_1 = (1, 0)$ and $\mathbf{A}_2 = (0, 1)$, therefore the polarizations of the modes are along the x and y direction.

An important statement is that the system is unstable, as we can recognize from the fact that for the whole lines $q_y = 0$ and $q_x = 0$ one of the two normal modes has zero frequency and hence does not cost energy. Let us take for example the line $q_y = 0$ and the branch described by ω_2, which is equal to zero. The corresponding displacements $\mathbf{u}_n(\mathbf{q}) = \mathbf{A}_2\, \mathrm{e}^{\mathrm{i}q_x R^0_{n,x}}$ depend only on q_x and not on t. This means that a shear strain along the $\mathbf{A}_2$ ($\equiv \widehat{\mathbf{y}}$) direction, as indicated by the dotted blue lines in Fig. 2.5, does not cost energy. The system, having many possible configurations with the same energy and thus no preferential configuration, is unstable against shear forces.

In conclusion the Lennard Jones potential including only nearest neighbors is not an appropriate choice for this system. In order to understand this properly we first need to discuss about the nature of the van der Waals forces. These are originated by dipole-dipole interactions due to fluctuating dipoles. They are rather weak interactions, which however dominate the bonding character of closed-shell systems. Therefore, the Lennard Jones potential gives an excellent, quantitative description of the interaction between noble gas atoms, such as argon, krypton, and xenon. On the other hand, it is not at all adequate to model situations with open shells, as in covalent systems or in metals. In these systems the two-body interactions scheme itself fails very badly. However, the study of noble gas crystals goes beyond the purpose of this work. Anyway,

regardless of how apt it is to model actual materials, the Lennard Jones potential constitutes an extremely important model system. One could say that it is the standard potential to use for all the investigations where the focus is on fundamental issues, rather than studying the properties of a specific material. For this reason we will further investigate the lattice dynamics of simple systems with the Lennard Jones potential with the inclusion of the second-nearest-neighbor interactions.

Second-nearest-neighbor approximation

In a second approach we consider interactions between first- and second-nearest-neighbor atoms, as illustrated in Fig. 2.7 (panel (a)).

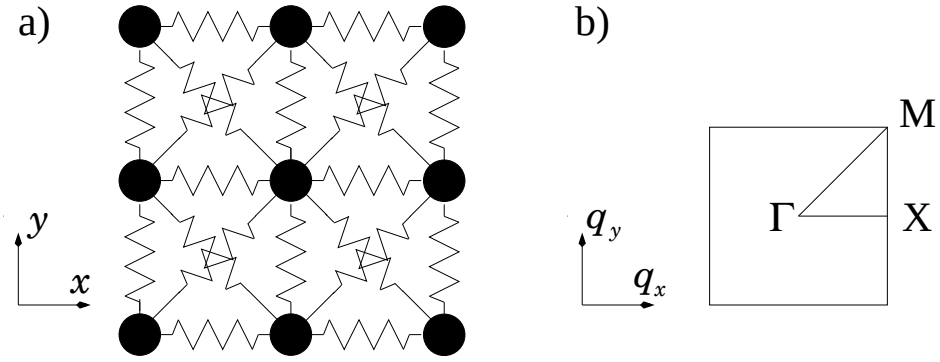

Figure 2.7: Panel (a) The square lattice with first- and second-nearest-neighbor interactions. Panel (b) The Brillouin zone of the square lattice is a square with side length $2\pi/r_0$. Important high symmetry points are marked.

The force constant tensor for the interaction with the second-nearest neighbors is given by Eq. (2.10) evaluated at the equilibrium distance $\sqrt{2}r_0$ and reads

$$\Phi(r_0(\widehat{\mathbf{x}}+\widehat{\mathbf{y}})) = \Phi(-r_0(\widehat{\mathbf{x}}+\widehat{\mathbf{y}})) = -k \begin{pmatrix} \frac{3}{128} & \frac{3}{128} \\ \frac{3}{128} & \frac{3}{128} \end{pmatrix} \tag{2.54}$$

$$\Phi(r_0(\widehat{\mathbf{x}}-\widehat{\mathbf{y}})) = \Phi(-r_0(\widehat{\mathbf{x}}-\widehat{\mathbf{y}})) = -k \begin{pmatrix} \frac{3}{128} & -\frac{3}{128} \\ -\frac{3}{128} & \frac{3}{128} \end{pmatrix} \tag{2.55}$$

and according to the acoustic sum rule (2.31) the self interaction tensor is now:

$$\Phi(0) = k \begin{pmatrix} \frac{67}{32} & 0 \\ 0 & \frac{67}{32} \end{pmatrix}. \tag{2.56}$$

The dynamical matrix now looks more complicate and also the off-diagonal terms are non-zero. For this reason it is common to calculate the dispersion along high symmetry

lines in the Brillouin zone. As mentioned, this last is a square with side length $2\pi/r_0$. The midpoint is conventionally denoted by Γ, the Δ axis leads to the midpoint X of a side of the square, and the Σ axis to a corner M of the square, as illustrated in Fig. 2.7 (panel (b)). The Z axes are the sides of the square X-M-X-... The dispersion curves along the lines of high symmetry are shown in Fig 2.8 (panel (a)) in blue. There are some changes from the result obtained for only nearest neighbors (plotted in red). Now both branches have non-zero frequency and the two-fold degeneracy of the branch along the Σ axis has been removed. The inclusion of the second-nearest-neighbor atoms stabilizes the system and refines the results in some particulars.

Now we shall see what happens considering other interatomic potentials that simulate the bonds of the square lattice in a different way.

2.4.2.2 Mahan-Jeon bond-stretching potential

We consider a potential from stretching of directed bond lengths, used by Mahan and Jeon [28] in a model for carbon nanotubes, as we will see later in Chapter 4. For first-neighbor interactions it has the form:

$$\mathcal{U}_1 = \frac{k_1}{2} \sum_{\langle ij \rangle} \left| \widehat{\delta}_{ij} (\mathbf{u}_j - \mathbf{u}_i) \right|^2 \tag{2.57}$$

where $\widehat{\delta}_{ij}$ is the unit vector connecting atom i and j and $\mathbf{u}$ denotes the displacements. The sum is over all nearest neighbor bonds and k_1 is the corresponding adjustable force constant.

The lattice is not stable against shear forces if elastic forces only exist between directly adjacent neighbors. Indeed, we obtain the same dispersion curve as in the case of the Lennard Jones model. Thus, we will pass to consider the second-nearest-neighbor approximation, as in Ref. [24]. The other potential $\mathcal{U}_2$ has the same form as $\mathcal{U}_1$, but between second nearest neighbors with force constant k_2. The total potential energy is the sum of this two terms. The force constant tensor for the first neighbors reads

$$\Phi(r_0\widehat{\mathbf{x}}) = \Phi(-r_0\widehat{\mathbf{x}}) = -k_1 \begin{pmatrix} 1 & 0 \\ 0 & 0 \end{pmatrix} \tag{2.58}$$

$$\Phi(r_0\widehat{\mathbf{y}}) = \Phi(-r_0\widehat{\mathbf{y}}) = -k_1 \begin{pmatrix} 0 & 0 \\ 0 & 1 \end{pmatrix} \tag{2.59}$$

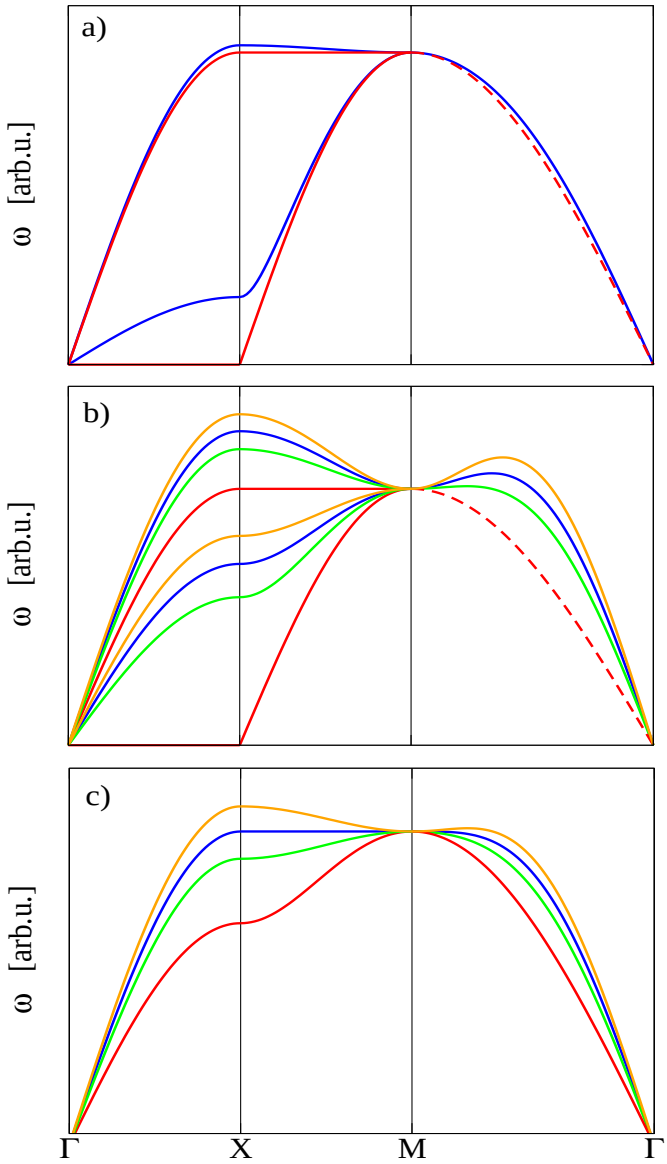

Figure 2.8: Dispersion relation of a two dimensional square lattice along high symmetry lines calculated with three different models. Panel (a): Lennard Jones model with first neighbors (red) and second neighbors (blue). The branch indicated by the dashed red line remains unchanged after including also the second neighbors, but it is not any more degenerate. The relative weight of the second neighbors is 3/128. Panel (b): Mahan-Jeon (MJ) bond-stretching model with first neighbors (red) and second neighbors (green, blue and orange for, respectively, $k_2 = k_1/3$, $k_2 = k_1/2$ and $k_2 = 2k_1/3$). The dotted red line remains unchanged passing from first- to second-nearest-neighbor approximation and is independent on k_2/k_1. Panel (c): general bond-stretching model with first neighbors (red) and second neighbors (green, blue and orange for $k_2 = k_1/3$, $k_2 = k_1/2$ and $k_2 = 2k_1/3$). In this model all the branches are two-fold degenerate.

and for the second neighbors:

$$\Phi(r_0(\widehat{\mathbf{x}}+\widehat{\mathbf{y}})) = \Phi(-r_0(\widehat{\mathbf{x}}+\widehat{\mathbf{y}})) = -k_2 \begin{pmatrix} \frac{1}{2} & \frac{1}{2} \\ \frac{1}{2} & \frac{1}{2} \end{pmatrix} \tag{2.60}$$

$$\Phi(r_0(\widehat{\mathbf{x}}-\widehat{\mathbf{y}})) = \Phi(-r_0(\widehat{\mathbf{x}}-\widehat{\mathbf{y}})) = -k_2 \begin{pmatrix} \frac{1}{2} & -\frac{1}{2} \\ -\frac{1}{2} & \frac{1}{2} \end{pmatrix} \tag{2.61}$$

and the self interaction tensor is

$$\Phi(0) = \begin{pmatrix} 2k_1+2k_2 & 0 \\ 0 & 2k_1+2k_2 \end{pmatrix}. \tag{2.62}$$

They have the same functional form as those found with the Lennard Jones potential (2.48, 2.49, 2.54, 2.55), but differ by a numerical factor. The deciding point is the choice of the ratio k_2/k_1, which in the Lennard Jones model is given by 3/128 and is fixed, while it is adjustable in the Mahan-Jeon (MJ) model. The dispersion relation is plotted in Fig. 2.8 (panel (b)) for different values of k_2/k_1. Comparing with the Lennard Jones model (panel (a)) we can state that the free adjustable ratio k_2/k_1 is the relevant point and that the Lennard Jones model assumes for this ratio a fixed value, which is lower than those used with the MJ model.

2.4.2.3 General bond-stretching potential

As last remark we choose also a stretching potential, but without the projection on the unit vector as in Eq. (2.57):

$$\mathcal{U}_1 = \frac{k_1}{2} \sum_{\langle ij \rangle} |(\mathbf{u}_j - \mathbf{u}_i)|^2 . \tag{2.63}$$

The force constant tensor now has an easy form:

$$\Phi(\pm r_0 \widehat{\mathbf{x}}) = \Phi(\pm r_0 \widehat{\mathbf{y}}) = -k_1 \begin{pmatrix} 1 & 0 \\ 0 & 1 \end{pmatrix} \tag{2.64}$$

$$\Phi(\pm r_0(\widehat{\mathbf{x}}+\widehat{\mathbf{y}})) = \Phi(\pm r_0(\widehat{\mathbf{x}}-\widehat{\mathbf{y}})) = -k_2 \begin{pmatrix} 1 & 0 \\ 0 & 1 \end{pmatrix} \tag{2.65}$$

$$\Phi(0) = \begin{pmatrix} 4k_1+4k_2 & 0 \\ 0 & 4k_1+4k_2 \end{pmatrix}. \tag{2.66}$$

Comparing with the precedent potentials we note that the interaction tensor is now diagonal and the only difference between first- and second nearest neighbor tensor elements are the factors k_1 and k_2. This facts are obvious since the direction given by $\widehat{\delta}_{ij}$

in Eq. (2.57) is now missing and Eq. (2.63) is completely symmetric in x and y and also in i and j. With this potential the lattice is stable already in first neighbor approximation. We obtain two degenerate branches with non-zero frequency, as illustrated in Fig. 2.8 (panel (c)). The inclusion of also the second neighbors does not change substantially the results. The degeneracy remains, the only thing that changes is the value at the X point, which increases with increasing k_2/k_1.

To conclude this Section, we can say that the three potentials taken in consideration are more or less in good agreement with each other and provide the general shape of the dispersion curves. We learned that a zero-frequency branch means instability which can be removed by the inclusion of second-nearest-neighbor interactions. We can state that the potential (2.63), needing only the first neighbors for stability, provides a simple and fast method to find a general overview of the dispersion. However, it does not take into consideration the particular geometric location of the neighbor atoms, since it has no parameter that specifies a direction, and because of its simplicity it is not able to remove the degeneracy of the branches.

For the more complicated lattice of graphene this is a clear disadvantage and the potential (2.57) provides a much better description without degeneracy. We will see in the next Chapter that a stretching potential alone is not able to describe a complicated lattice such as graphene and that it has to be accompanied by a bond-bending potential that takes rise of angular forces.

Chapter 3

Phonons in graphene

For investigation of graphene, graphite, or carbon nanotubes it is often desirable to have a force constant parameterization for fast—yet reliable—calculations. In this Chapter we deal with two main force-constant approaches: the valence-force-field model and the direct parameterization of the diagonal real-space force constants up to the 4th nearest neighbor. In many model calculations, the force-constant parameters for graphene are empirically determined by fitting experimental data. We perform, instead, a parameter fit to *ab initio* dispersion relations.

3.1 General observations

3.1.1 The dynamical matrix

The graphene honeycomb lattice consists of two hexagonal sublattices with respectively atoms of type A and B (see Sec. 1.1). Since there are two carbon atoms in the unit cell, we must consider $3r = 6$ degrees of freedom. The secular equation to be solved is thus a 6×6 dynamical matrix. The dynamical matrix $\mathsf{D}(\mathbf{q})$ is constructed using the site representation and is written as

$$\mathsf{D}(\mathbf{q}) = \begin{pmatrix} D^{AA} & D^{AB} \\ D^{BA} & D^{BB} \end{pmatrix} \tag{3.1}$$

where each block $D^{\tau,\tau'}$ is a 3×3 matrix describing the coupling for the τ and τ' atoms within the unit cell. As mentioned the dynamical matrix is symmetric. Figure 3.1 shows the neighbor atoms up to fourth nearest neighbors for atoms of type A and B: for an A atom, the three nearest-neighbor atoms are $B1$, $B2$, and $B3$ and their contributions to $\mathsf{D}(\mathbf{q})$ are contained in D^{AB}. The second nearest neighbors are six

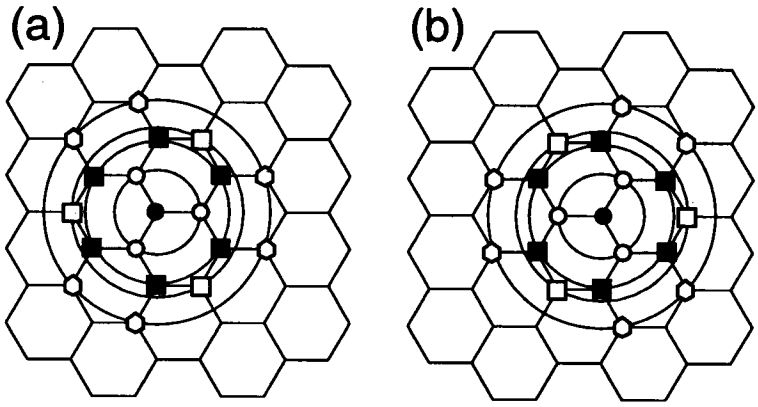

Figure 3.1: Nearest-neighbor atoms for an atom of type A (panel (a)) and B (panel (b)). The atoms from 1st to 4th neighbors are marked by open circles, solid squares, open squares and open hexagons, respectively. The circles connect atoms of the same neighbor order (taken from Ref. [13]).

atoms of type A, denoted by solid squares. As concerns the self interaction tensor, they contribute to D^{AA}.

Now the important point is how to construct the force constant tensor. The general form of the force constant tensor for the interaction of the atom (n, τ) with the atom (m, τ') in the graphene sheet is:

$$\Phi(\mathbf{R}^0_{n,\tau} - \mathbf{R}^0_{m,\tau'}) = \begin{pmatrix} a & b & 0 \\ c & d & 0 \\ 0 & 0 & e \end{pmatrix}. \tag{3.2}$$

The coordinate system is chosen such that x is the longitudinal coordinate (along the line connecting the two atoms), y the transverse in-plane coordinate, and z the coordinate perpendicular to the plane. The block-diagonal structure of the tensor reflects the fact that in graphene the in-plane and out-of-plane vibrational modes are completely decoupled from each other. We will see how to get the force constants in the next Section, but first we introduce the concept of bond-bending forces, which play a relevant role in the graphene lattice.

3.1.2 Bond-bending forces

In Sec. 2.4.2 we studied the square lattice within three simple force-constant models, but considering only bond-stretching forces, which act in case of variations of the bond length. We saw that using a model that includes only first nearest neighbors, the

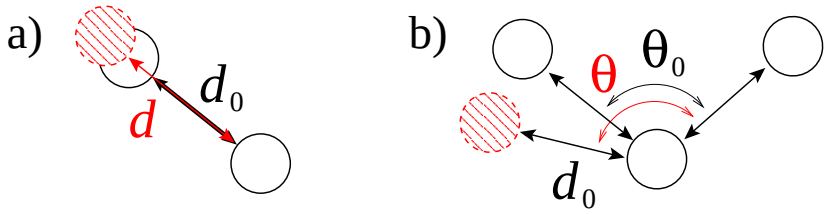

Figure 3.2: Schematic representation of nearest-neighbor forces: a) two-body force (bond stretching), b) three-body force (bond bending).

square lattice results unstable against shear strain along the axis directions. This problem can be avoided considering bond-bending forces as well, which are angular forces that try to preserve the equilibrium bond angle. We already mentioned them in Sec. 2.4.1. They are three-body forces because of involving the three atoms that form the bond angle. Figure 3.2 shows a schematic representation of bond stretching and bond bending. The two-body force constant should depend only on the interatomic distance, whereas the three-body force constant depends in general on the two involved bond lengths and on the enclosed angle θ. Force-constant models including such terms were proposed by Kirkwood [29] and Keating [30] and then refined and adapted to various systems by many other authors. For a correct description of graphene, bond-bending forces are of central importance. In Ref. [31] Hass directly compared a two-parameter Kirkwood model with a two-parameter Keating model (which we will see later) applied to graphene.

3.2 Valence-force-field models

In the valence-force-field (VFF) approach, all interatomic forces are resolved into bond-stretching and bond-bending forces. Forces between atoms arise from changes of the electronic energy due to atomic displacements from the equilibrium configuration during the vibrations. Because of the directional properties of orbitals, force act along the valence bonds and bond angles. The VFF model gets the parameters of the force-constant tensor through the introduction of spring constants that determine the change in potential energy upon different deformations. In our case, the spring constants reflect the fact that a sp^2-bonded system tries to preserve its planar geometry and equilibrium bond angles.

There are two primary advantages of the VFF model. Firstly, because all distortions are described in terms of bond lengths and angles, the model is automatically rota-

tionally invariant so that serious errors that may arise in the ordinary force-constant approach are avoided [30]. Secondly, in crystals in which atom-pair bonds play an essential role, the VFF model is the most natural description of interatomic forces. Therefore, we expect that the VFF model involves the smallest possible number of parameters.

3.2.1 Keating model

A useful and also one of the simplest special cases of the VFF model was proposed by Keating [30]. It has two terms corresponding to bond-stretching and bond-bending contributions to the total energy. Such terms have been included by other authors in model calculations for graphene and graphite [31-37] or other materials [38, 39]. The weak interlayer interactions in crystalline graphite have small effects on the vibrational spectrum, allowing us to compare directly results obtained for graphene and graphite. In this Section we calculate the dispersion relations for graphene with a two-parameter Keating model as presented by Hass [31].

The key idea of the Keating model is to write the potential energy of the solid as a sum of two terms that are positive definite scalars constructed from the bond vectors $\mathbf{X}_{ij} = \mathbf{R}_i - \mathbf{R}_j$ that connect an atom i to one of its nearest neighbors j. The first term is of bond stretching and describes deviations from the equilibrium bond length d_0, while the second term is of bond bending and denotes deviations from the equilibrium bond angle $\theta_0 = 120°$. Following that idea, the potential energy of sp^2-bonded carbon can be written as:

$$\mathcal{U}_{\mathrm{Keat}} = \frac{k_{\mathrm{Ks1}}}{8d_0^2} \sum_{\langle ij \rangle} \left(\mathbf{X}_{ij} \cdot \mathbf{X}_{ij} - d_0^2 \right)^2 + \frac{k_{\mathrm{Kb}}}{2d_0^2} \sum_{\langle ijk \rangle} \left(\mathbf{X}_{ij} \cdot \mathbf{X}_{ik} - d_0^2 \cos\theta_0 \right)^2 \tag{3.3}$$

The first sum is over all nearest-neighbor bonds and the second sum is over all pairs of such bonds sharing one atom. k_{Ks1} and k_{Kb} are adjustable parameters that describe the bond-stretching and bond-bending restoring forces, where K, s, and b indicate Keating, stretching, and bending terms, respectively, and 1 stands for first nearest neighbors. Figure 3.3 shows the phonon-dispersion curves resulting from this model along high-symmetry lines of the Brillouin zone of graphene. We obtain four non-zero branches: For both acoustic and optic ones we have a transversal (TA and TO, respectively) and a longitudinal (LA and LO) mode, representing all in-plane vibrations.

The valence force parameters are taken as $k_{\mathrm{Ks1}} = 4.409\,\mathrm{mdyn/Å}$ and $k_{\mathrm{Kb}} = 0.754\,\mathrm{mdyn/Å}$ [1] [31]. They were constrained to give a zone-center optic-mode frequency of $1585\,\mathrm{cm}^{-1}$ and a TA mode at M of $800\,\mathrm{cm}^{-1}$, in order to fit the experimental

[1] $1\,\mathrm{mdyn/Å} = 10^2\,\mathrm{N/m}$

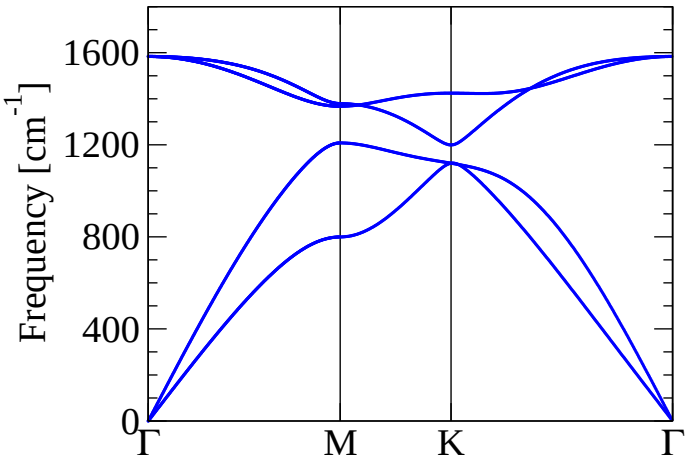

Figure 3.3: Phonon-dispersion curves for the in-plane vibrations of 2D graphene in the Keating model. In three dimensions the system is unstable, because the two out-of-plane modes have zero frequency. The valence-force parameters are $k_{\mathrm{Ks1}} = 4.409\,\mathrm{mdyn/\AA}$ and $k_{\mathrm{Kb}} = 0.754\,\mathrm{mdyn/\AA}$ [31].

frequencies. The last one is a pure bending mode whose frequency is determined entirely by k_{Kb}.

The most important statement is that this model does not reproduce at all the out-of-plane vibration modes, indeed the responsible two missing branches have zero frequency in the whole Brillouin zone. We expect only in-plane vibration modes because the force constant tensor has the generic form:

$$\Phi(\mathbf{R}^0_{n,\tau} - \mathbf{R}^0_{m,\tau'}) = \begin{pmatrix} a & b & 0 \\ c & d & 0 \\ 0 & 0 & 0 \end{pmatrix} \tag{3.4}$$

where a, b, c, d are values depending on k_{Ks1} and k_{Kb}. This means that the bond-stretching and bond-bending terms of the Keating model are not able to describe variations in energy when one atom moves out of the graphene plane, in z direction. Nevertheless, the Keating model has been used frequently because it gives reasonable results for the in-plane modes and is extremely simple. However, we will see that also for this modes there are still differences with the experimental data and the *ab initio* results.

3.2.2 Mahan-Jeon model applied to graphene

In this Section we analyze another VFF model which was developed by Mahan and Jeon for the special case of carbon nanotubes [28]. Before considering the application to the latter, we want to see if the same model provides suitable results also for graphene. It is more sophisticated than the simple two-parameter Keating model, therefore, we expect more detailed results.

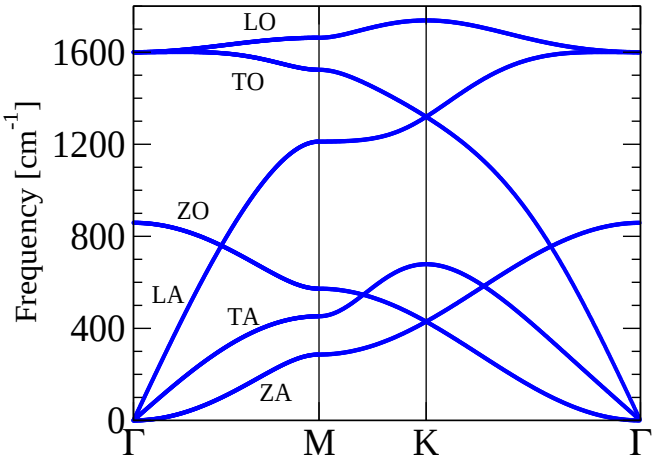

Figure 3.4: Phonon-dispersion curves in the Mahan-Jeon (MJ) model. The relative weights of the three parameters is set to $k_{\mathrm{Ms1}} = 1$, $k_{\mathrm{Ms2}} = 0.12$ and $k_{\mathrm{Mb}} = 0.024$, as in Ref. [28] for the (10,10) CNT. The frequencies in units of cm^{-1} are given by the square root of the eigenvalues of the dynamical matrix multiplied by a factor $1600/\sqrt{3}$.

The Mahan-Jeon (MJ) model is characterized by three potential-energy terms: The first two take into account the bond stretching with the first- and the second- nearest-neighbor atoms, respectively, the latter is related to the bond bending. We already introduced the bond-stretching potential in the example of the square lattice (see Eq. (2.57)). For the nth nearest neighbors it has the form:

$$\mathcal{U}_{\mathrm{n}} = \frac{k_{\mathrm{Msn}}}{2} \sum_{\langle ij \rangle} \left| \widehat{\delta}_{ij} \cdot (\mathbf{u}_j - \mathbf{u}_i) \right|^2 \tag{3.5}$$

where $\widehat{\delta}_{ij}$ is the unit vector connecting atom i and j. The sum is over all nearest-neighbor bonds. Since we deal with interactions up to the second nearest neighbors, we have to consider the potentials $\mathcal{U}_1$ and $\mathcal{U}_2$ with the parameters k_{Ms1} and k_{Ms2}, respectively. The bond-bending term has the form:

$$\mathcal{U}_3 = \frac{k_{\mathrm{Mb}}}{2} \sum_j \left| \sum_{i=1}^{3} \widehat{n}_{ij} \cdot (\mathbf{u}_j - \mathbf{u}_i) \right|^2 \tag{3.6}$$

where the second sum goes over the first neighbor atoms of atom j. The vector $\widehat{n}_{ij} = \widehat{x} \times \widehat{\delta}_{ij}$ points in a direction perpendicular to the graphene plane, at the midpoint of the bond between the two atoms. The force constant tensor has the generic form as in Eq. (3.2) with a, b, c, d depending on k_{Ms1} and k_{Ms2}, while e depends on k_{Mb}. From this we can state immediately that only the bond-bending term contributes to the out-of plane modes, as expected.

Figure 3.4 shows the resulting phonon-dispersion relation. The dispersion relation comprises three acoustic (A) branches and three optical (O) branches. The modes affiliated with out-of-plane (Z) motion are considerably softer than the in-plane longitudinal (L) and transverse (T) modes. The parameters k_{Ms1} and k_{Ms2} define the dispersion of

LA, LO, TA and TO modes, while k_{Mb} defines ZA and ZO modes. The three branches which originate from the Γ point of the Brillouin zone are acoustic modes: In order of increasing energy there are an out-of-plane ZA mode, an in-plane tangential TA (bond-bending) mode and an in-plane radial LA (bond-stretching) mode. For $\mathbf{q} = 0$ these modes have zero frequency, which corresponds to translations of the graphene sheet along the three orthogonal axes. While the TA and LA modes display the normal linear dispersion around the Γ point, the ZA mode shows a q^2 energy dispersion which is explained in Ref. [13] as a consequence of the D_{6h} point-group symmetry of graphene. Another consequence of the symmetry are the linear crossings of the ZA/ZO modes and the LA/LO modes at the K point.

We will see later that there are great differences between the dispersions obtained in the MJ model and the *ab initio* results. The MJ model was developed and optimized for carbon nanotubes and fails in the case of graphene. Also changing the relative weights of the parameters k_{Ms1}, k_{Ms2} and k_{Mb} the results do not improve.

3.3 Direct parametrization of the force constants

The model proposed by Saito and coworkers in Ref. [13] consists in the direct parametrization of the diagonal real-space force constants including up to fourth nearest neighbor interactions (4NNFC approach). It was developed by Jishi and coworkers [40,41] for planar graphene based on the experimental data of graphite and further also adapted to carbon nanotube geometries.

In the 4NNFC approach the force-constant tensor has the generic form as in Eq. (3.2), but with the additional simplifying assumption that, when writing Φ in a system of coordinates where x is parallel to the bond, the off-diagonal elements b and c can be neglected. Using a new notation, the force constant tensor describing the interaction between an atom and its nth nearest neighbor atom on the x axis has the form:

$$\Phi = \begin{pmatrix} \phi_r^{(n)} & 0 & 0 \\ 0 & \phi_{ti}^{(n)} & 0 \\ 0 & 0 & \phi_{to}^{(n)} \end{pmatrix}. \tag{3.7}$$

where $\phi_r^{(n)}$, $\phi_{ti}^{(n)}$, and $\phi_{to}^{(n)}$ represent the force-constant parameters in the radial (bond-stretching), in-plane, and out-of-plane tangential (bond-bending) directions of the nth nearest neighbors. Due to the fact that the off-diagonal elements are zero, a longitudinal displacement of an atom can only induce a force in longitudinal direction towards its nth neighbor and a transverse displacement can induce only a transverse force. Figure 3.5

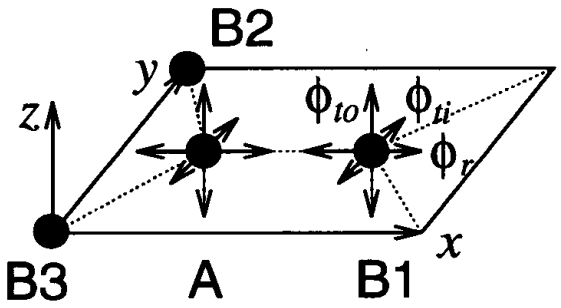

Figure 3.5: An atom A and its first nearest neighbors $B1$, $B2$, and $B3$. ϕ_r, ϕ_{ti}, and ϕ_{to} represent forces in the radial, in-plane, and out-of-plane directions (taken from Ref. [13]).

shows an atom of type A with its three nearest neighbor atoms $B1$, $B2$, and $B3$ and a schematic representation of the force constants between atom A and $B1$. The radial direction corresponds to the direction of the bonds and the two tangential directions are perpendicular to the radial direction.

The force-constant tensors for the other nth nearest neighbor atoms are obtained by rotating the tensor in Eq. (3.7). For example for first nearest neighbors ($n = 1$) we obtain the force-constant tensor $\Phi^{(A,Bp)}$ between atom A and Bp ($p = 2, 3$) by

$$\Phi^{(A,Bp)} = U_z^{-1}(\theta_p)\, \Phi^{(A,B1)}\, U_z(\theta_p) \tag{3.8}$$

where $U_z(\theta_p)$ is a unitary rotation matrix around the z axis:

$$U_z(\theta_p) = \begin{pmatrix} \cos(\theta_p) & \sin(\theta_p) & 0 \\ -\sin(\theta_p) & \cos(\theta_p) & 0 \\ 0 & 0 & 1 \end{pmatrix}. \tag{3.9}$$

For example, for atom $B2$ the rotation angle is $\theta_2 = 2\pi/3$. Considering the force-constant tensor of the nth-nearest-neighbor atom, we note that they are not always located on the x axis, so that we can not assume an initial tensor as given by Eq. (3.7). This is for example the case of the 2nd and 4th neighbor atoms in graphene. We can get the tensor constructing first a tensor for a virtual atom at the same distance but on the x axis, and then rotating it by the appropriate angle.

As we have seen in the example of the square lattice (Sec. 2.4.2), the inclusion of more than only first-nearest-neighbor atoms improves a lot the results, because it takes more and more into account the long-range character of the dynamical matrix. Saito and coworkers considered interactions up to 4th nearest neighbors, in order to describe also the twisted motion of four atoms [13]. Thus, there are twelve free parameters to determine. We calculate the dispersion relation with the parameters proposed by Jishi and coworkers [41], shown in Table 3.1. Those have been obtained by fitting experimental phonon-dispersion relations [37].

Radial		Tangential			
$\phi_r^{(1)} =$	36.50	$\phi_{ti}^{(1)} =$	24.50	$\phi_{to}^{(1)} =$	9.82
$\phi_r^{(2)} =$	8.80	$\phi_{ti}^{(2)} =$	-3.23	$\phi_{to}^{(2)} =$	-0.40
$\phi_r^{(3)} =$	3.00	$\phi_{ti}^{(3)} =$	-5.25	$\phi_{to}^{(3)} =$	0.15
$\phi_r^{(4)} =$	-1.92	$\phi_{ti}^{(4)} =$	2.29	$\phi_{to}^{(4)} =$	-0.58

Table 3.1: Force-constant parameters of Ref. [41] for graphene in units of 10^4 dyn/cm = 10 N/m.

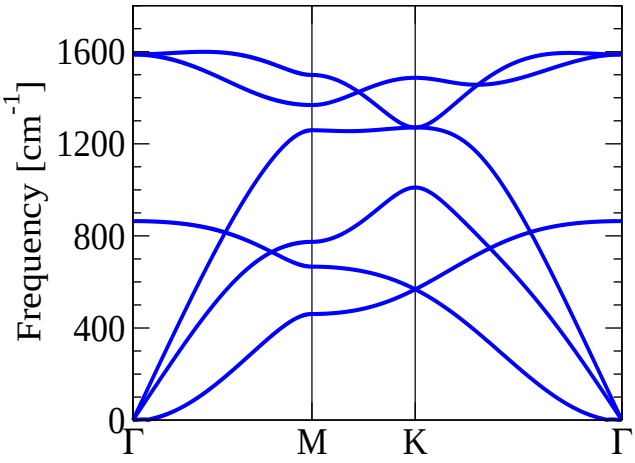

Figure 3.6: The phonon-dispersion curves for graphene in the fourth-nearest-neighbor approach (4NNFC), using the parameters of Table 3.1

Figure 3.6 shows the resulting phonon-dispersion curves of a graphene sheet. As in the case of the MJ model, we obtain a quadratic dispersion for the out-of-plane acoustic phonon branch. In the next Section we will make a direct comparison with the results of *ab initio* calculations and then try to adapt the parameters of Tab 3.1 in order to fit these values.

3.4 Comparison with *ab-initio* calculations

First-principles calculations are generally in good agreement with the experimental data [37,42-44] since the long-range character of the dynamical matrix is properly taken into account. The latter fact limits the validity of force-constant approaches that take into account only interactions with few neighboring atoms. In this Section we show that the 4NNFC model yields a excellent fit for the low-frequency modes and a moderately good fit for the high-frequency modes.

The first *ab initio* calculations for graphite were done in the framework of density-functional perturbation theory by Pavone and coworkers [45] and recently in local-density approximation [46-48] and generalized-gradient approximation [42, 49]. Figure 3.7 shows the *ab initio* phonon-dispersion relation of graphene resulting from calculations done by Bohnen and Heid [50]. These calculations introduce considerable

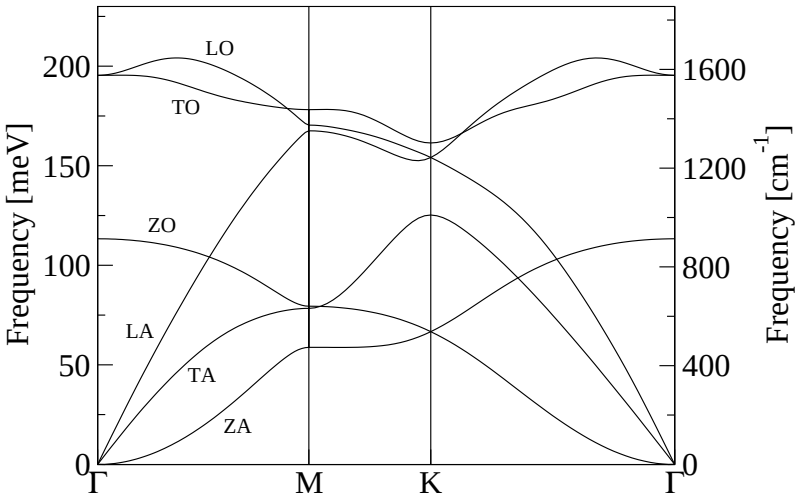

Figure 3.7: Phonon-dispersion relation of graphene calculated with an *ab initio* approach [50].

qualitative changes in the behavior of the high-frequency branches as compared to the force-constant fits. In particular, these calculations establish a crossing of the longitudinal and transverse optical branches along the Γ-K as well as the Γ-M direction. Another important feature is that the graphite phonon branch that corresponds to the longitudinal high-energy optic mode (LO) has a local minimum at the Γ point. This is usually referred as "overbending", since the local maxima thus appear at some general points of the Brillouin zone around the Γ point. A similar overbending has been found also for diamond: In that case a frequency shift of about $30\,\mathrm{cm}^{-1}$ above the Γ point frequency was found. Pavone and coworkers explained it as due to strong bending forces between the in-plane atoms [51]. For graphene the overbending is so strong that the LO mode decreases rapidly, crossing in both directions the TO mode.

A direct comparison between the force-constant models and the *ab initio* results yields as an immediate result that the two-parameter Keating model and the MJ model applied to graphene are insufficient to describe accurately the dispersion relations of graphene. They provide only the general shape of the dispersion curves, but fail to reproduce the correct slope and the correct frequency values. A combination of the two models to a new four-parameter model provides better results: Taking the three MJ potentials and in addition the bond-bending term of the Keating model (second term in Eq. (3.3)), we get the dispersion curves of Fig. 3.8 (panel (a)).

We probed also another combination of the two models: the bond-stretching term is taken from Keating and includes first- and also second-nearest neighbors, the bond-bending term is given by the sum of the Keating and the MJ-bond-bending forces. The results are shown in Fig. 3.8 (panel (b)). The behavior of the LA and TA branches is almost satisfactory, and especially in the model of Fig. 3.8 (panel (a)) also the behavior of the LO and LA branches along the M-K direction is correctly described. The out-of-

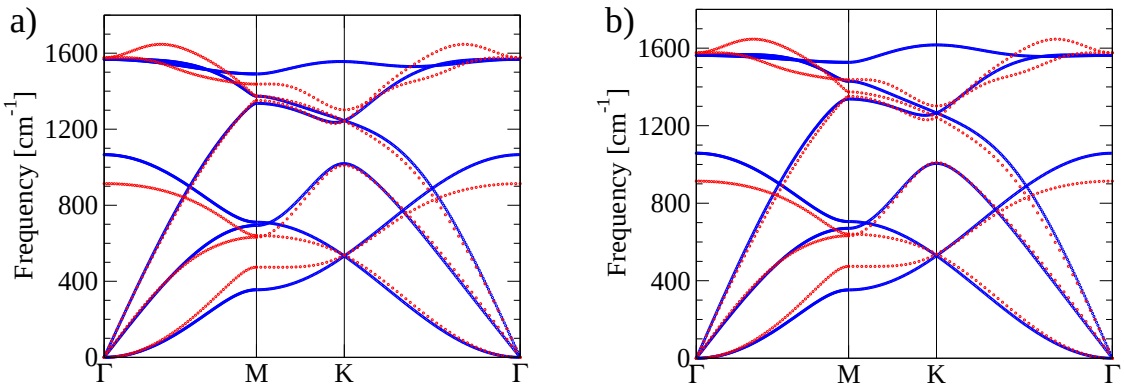

Figure 3.8: Dispersion relation of graphene calculated with a model calculation (blue lines). For comparison are shown also the *ab initio* curves (dotted red lines). The model calculation is given by a combination of the MJ and the Keating potentials. Panel (a): MJ potentials and the bond-bending term of Keating. The relative weights of the interactions were set to k_{Ms1}=0.082, k_{Ms2}=0.072, k_{Mb}=0.037, and k_{Kb}=0.07. The results have to be multiplied by a factor $1600/\sqrt{3}$. Panel (b): The Keating potentials of bond stretching (for 1st and 2nd nearest neighbors) and bond bending in addition to the MJ-bond-bending potential term. The parameters are given by k_{Ks1}=5.1, k_{Ks2}=0.2, k_{Kb} = 0.33, and k_{Mb}= 0.22 [mdyn/Å].

plane modes ZO and ZA are determined only by the bond-bending term of Mahan and Jeon. The general behavior is correct, but the gap between the two branches in the Γ point and in the M point is too large. Both models still fail in describing correctly the high-energy optical modes, in particular the LO branch. In order to obtain better results one has to include more parameters, as in the model of Aizawa *et al.* [37], Gartstein [35], or the recent bond-charge model of Mahan and Jeon [34]. But due to the fewer number of parameters, the VFF models can not compete in accuracy with the 4NNFC approach. We turn now to this approach.

In our next attempt we consider the 4NNFC model with twelve free parameters. The purpose is to adapt the parameters in order to fit the *ab initio* dispersion relation. Saito *et al.* proposed new parametrizations in Ref. [52, 53], but only the higher-frequency region around the K point is different from that in Fig. 3.6 and does not reproduce at all the crossings of the LO and TO branches along the Γ-M and Γ-K lines. As a starting point for our new parametrization we consider the force-constant tensors obtained by the *ab initio* calculations of Bohnen and Heid [50]. It is possible to compare them directly with the force constant tensors of the 4NNFC model. A remarkable point is that for the *ab initio* tensors also the off-diagonal terms (b and c in Eq. (3.2)) are non-zero. Taking into account the parameters of Bohnen and Heid we adapt the twelve parameters for the 4NNFC approach. We obtain a good fit for the set of parameters listed in

Table 3.2. We follow Gartstein [35] choosing the in- and out-of-plane tangential force constants $\phi_t^{(n)}$ so as to satisfy $\phi_t^{(1)} + 6\phi_t^{(2)} + 4\phi_t^{(3)} + 14\phi_t^{(4)} = 0$. This equality is required by the rotational invariance of the graphene plane, and the original parameters of Saito and coworkers do not obey this rule. Figure 3.9 shows the dispersion relation resulting from the original parametrization (panel (a)) and from our new parametrization (panel (b)). The resulting curves are superposed to the *ab initio* dispersion, for direct comparison. The 4NNFC model with our force constants of Table 3.2 gives good results for the general behavior of the dispersion relation. In particular it gives a good fit of the slope of the acoustic modes (which in turn determine the specific heat), but cannot properly describe the dispersion of the high-frequency modes. Neither parametrization reproduces the initial upward curvature (overbending) of the LO branch away from Γ that is seen in both the experimental data and the *ab initio* dispersions. Our fit of the 4NNFC model yields a major improvement referring to the crossing of the LO and TO branches along the Γ-M and Γ-K directions and leads to a qualitatively correct ordering of the LA and LO modes along the line M-K. For a very high-accuracy fit, a fourth-nearest-neighbor approach is not enough and we need to consider also more distant neighbor atoms. In particular, the TO phonon at the K-point is very sensitive to the parametrization and can be described accurately only if the long-range character of the dynamical matrix is properly taken into account.

Of particular interest is the nature and range of the force-constant tensor. Firstly, we consider the influence of single parameters on the shape of the dispersion curves. The out-of-plane branches (ZA, ZO) are determined only by the tangential out-of-plane constants $\phi_{to}^{(n)}$, which is due to the decoupling of the in-plane and out-of-plane modes, as mentioned. Indeed setting $\phi_{to}^{(n)} = 0\ \forall n$, the dispersion shows two zero-frequency branches. The first-neighbor constants determine the overall scaling of the whole phonon dispersion curves. In particular $\phi_r^{(1)}$ can be chosen so as to reproduce graphene experimental LO and TO optical frequencies at $\mathbf{q} = 0$, while $\phi_{lo}^{(1)}$ fixes the value of the ZO branch at $\mathbf{q} = 0$. $\phi_r^{(1)}$ and $\phi_{ti}^{(1)}$ determine the behavior of the TA and LO branch along the M-K direction. $\phi_r^{(3)}$ has an influence in particular on the initial slope of the LO branch, which increases with increasing $|\phi_r^{(3)}|$ and the TA branch, in

Radial		Tangential			
$\phi_r^{(1)} =$	41.8	$\phi_{ti}^{(1)} =$	15.2	$\phi_{to}^{(1)} =$	10.2
$\phi_r^{(2)} =$	7.6	$\phi_{ti}^{(2)} =$	-4.35	$\phi_{to}^{(2)} =$	-1.08
$\phi_r^{(3)} =$	-0.15	$\phi_{ti}^{(3)} =$	3.39	$\phi_{to}^{(3)} =$	1.0
$\phi_r^{(4)} =$	-0.69	$\phi_{ti}^{(4)} =$	-0.19	$\phi_{to}^{(4)} =$	-0.55

Table 3.2: New parametrization for the force constants of graphene in units of 10^4 dyn/cm = 10 N/m.

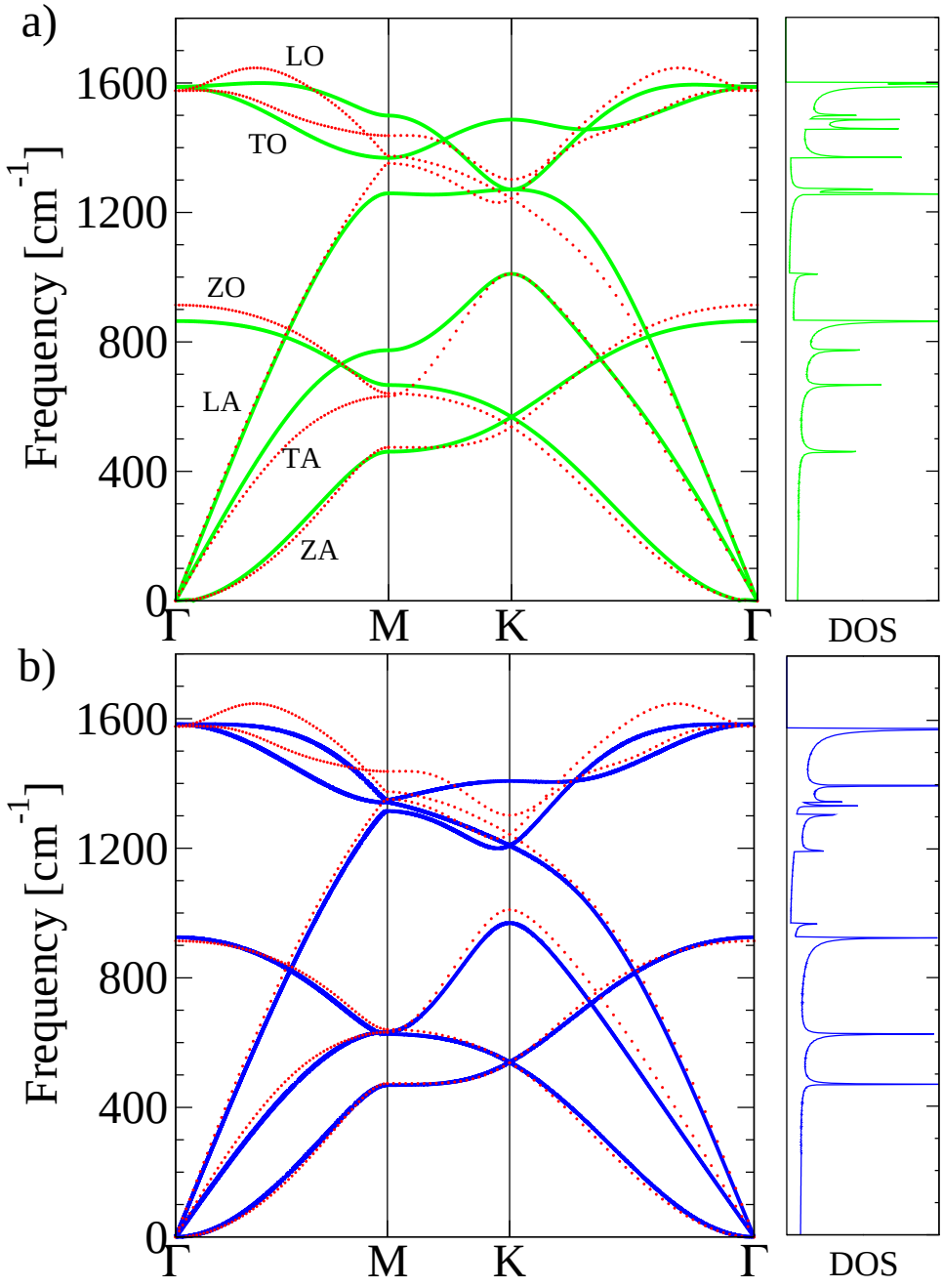

Figure 3.9: Dispersion relation of graphene calculated with the 4NNFC approach (green and blue solid lines) and the corresponding vibrational density of states (DOS). For comparison are plotted also the *ab initio* results (dotted red lines). Panel (a): 4NNFC approach using the parameters of Ref. [41], listed in Table 3.1. Panel (b): 4NNFC approach with our parametrization, given in Table 3.2. It reproduces most of the features of the phonon dispersion relation of graphene. Notable exceptions are the TO mode at K and the missing overbending of the LO branch. See text for details.

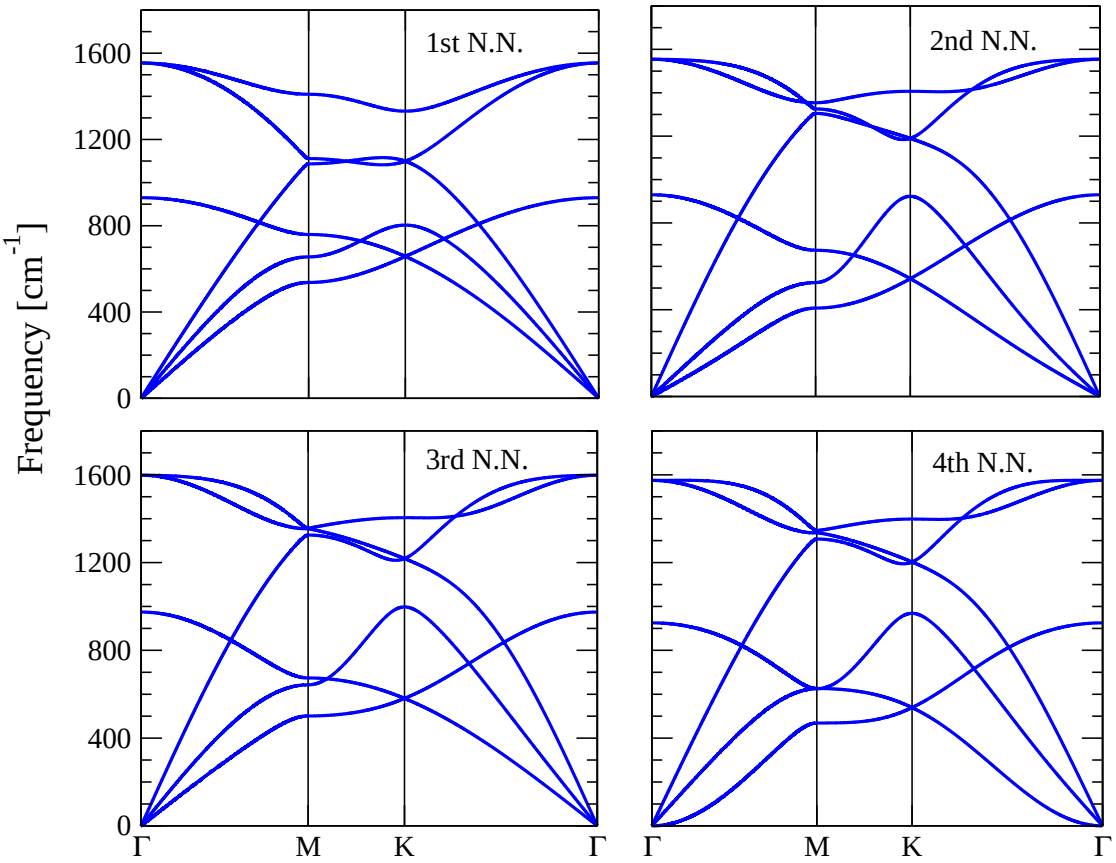

Figure 3.10: Dispersion relation for graphene calculated through the direct parametrization of the diagonal force constants, shown with increasing number n of nearest neighbor atoms included ($n = 1 \dots 4$). All curves are plotted using the parametrization of Table 3.2, setting $\phi^{(m)} = 0$ for $m > n$.

particular around the M point, which lowers with increasing $|\phi_r^{(3)}|$.

As can be seen, the magnitude of the force constants falls off very rapidly when moving to more distant atoms. Because of this rapid decay, it is tempting to include only few nearest neighbors for the determination of the dynamical matrix. For this reason, starting from first nearest neighbors, it is interesting to observe the changes when including step for step the next neighbor atoms. Figure 3.10 shows the resulting curves from first up to fourth nearest neighbors. A first nearest neighbor approximation alone gives unsatisfying results in particular for the optical branches. The crossing point of the ZA and ZO branches at K has to high frequency and the ZA mode has linear dispersion around Γ. The inclusion of the second neighbor atoms improves a lot the behavior of the optical LO and TO branches, and of the LA mode between M and K. Neglecting the off-diagonal terms of the *ab initio* force-constant tensor for

second nearest neighbors, we obtain also the crossing of the LO and TO branches. The third neighbors contribute in lowering the TO branch, which is the most delicate matter and is difficult to fit correctly within a force constant model. At the same time the other modes are shifted to higher frequencies, in particular the TA mode. It is interesting to note that in a approximation up to third nearest neighbors only, the ZA branch shows a linear dispersion. The inclusion of also the fourth nearest neighbors is needed to obtain the correct q^2 dependence. This is the main effect of fourth neighbors, furthermore another effect is the lowering of the out-of-plane branches. Instead there are no changes in the high frequency region. For further improvements longer ranged interactions need to be included.

Chapter 4

Phonons in carbon nanotubes

A carbon nanotube can be thought of as a single graphene sheet that is wrapped into a cylinder. Wrapping the sheet has two major effects on the phonon band structure. Firstly, the phonon spectrum of CNTs displays quantum size effects, since the 2D phonon bands of graphene fold into a set of quantized 1D subbands of the nanotube. Secondly, the cylindrical shape of the tube renders it stiffer than the sheet, changing the dispersion of the lowest-lying modes. First tentatives for calculating the phonon dispersion of carbon nanotubes were to construct a spring and mass model for a single sheet of graphite and use the same forces to calculate the phonons in a nanotube. Unfortunately this does not work. The fact that the bonds are bent, in a nanotube, means that the force constants change not only in value, but also in symmetry.

In Sec. 4.2 and 4.3 we present two methods for calculating the phonon dispersions of both armchair and zigzag nanotubes. Particular attention is drawn in Sec. 4.4 to the important Raman-active radial breathing mode and to its diameter dependence. Finally, in Sec. 4.5 we focus on strong Raman-active modes and show on explicit examples how the atoms do effectively move.

4.1 From graphene to carbon nanotubes

In a first approximation the phonon dispersion of carbon nanotubes can be found theoretically by zone folding the graphene dispersion. The folding is obtained by slicing the graphene Brillouin zone in the appropriate direction. For details we refer to the books of Maultzsch and coworkers [12] and Saito and coworkers [13]. This approach works reasonably well and is applicable for almost all the phonon modes of a carbon nanotube. However, it does not always give the correct dispersion relation for a carbon nanotube, especially in the low frequency region. Firstly, the out-of-plane acoustic (TA)

mode of graphene, which for $\mathbf{q} = 0$ describes translations along the axis perpendicular to the sheet, transforms into a mode in which all the atoms of the nanotube move radially, with non-zero frequency at the Γ point. This mode is called radial breathing mode and cannot be reproduced using the zone folding scheme. Secondly, there should be two modes, called flexure modes, with zero frequency corresponding to translation of the tube perpendicular to the tube axis. This corresponds to a linear combination of both in-plane and out-of-plane graphene-derived modes. These modes do not couple in graphene, but do couple to each other in a nanotube, forming an acoustic mode. Since the zone folding procedure neglects any effects of the cylinder geometry and curvature of the tube walls, results obtained by zone folding have to be used with great care.

First calculations of the phonon dispersion in carbon nanotubes have been accomplished either by the zone-folding method with correction of the dynamical matrix in order to obtain the two acoustic branches (Jishi *et al.* [41]) or by a force-constant model with a modification of the force constants in order to fulfil the rotational sum rule and to obtain the torsional-acoustic branch (Saito *et al.* [18]). In the latter work it is obtained, however, that the four acoustic modes have non-zero slope at the origin. In the last years have been published valence force-field model [28,35,36,54,55], tight binding [56] and *ab initio* [46, 48, 57, 58] phonon dispersions of a few carbon nanotubes. The full phonon dispersion of carbon nanotubes could not be determined experimentally, so far, because single crystals of single-wall nanotubes of the same chirality do not exist. Only Γ-point phonons are probed by conventional Raman scattering. First-principles calculations of the phonon dispersion in carbon nanotubes are rare and mostly restricted to achiral tubes because of the large number of atoms in the chiral unit cell.

4.1.1 Nanotube unit cells

The unit cell of a carbon nanotube in real space is a finite size cylinder defined by chiral and translational vector, which we introduced in Sec. 1.2. The number of atoms per unit cell is strongly chirality-dependent, indeed armchair nanotubes have less number of atoms and chiral nanotubes have the most. For better understanding we give some examples of the dimensions in Table 4.1. We denote the $2N$ atoms in the unit cell as Ai and Bj with $i, j = 1 \ldots N$, where the N Ai (or N Bj) atoms are geometrically equivalent to each other. In Fig. 4.1 are shown the unit cells of an armchair and a zigzag carbon nanotube. We can emphasize the different shape and also the length of the unit cell for different types of CNTs with the same number of atoms in the unit cell. The latter is defined by the translational vector $|\mathbf{T}|$ (defined in Sec. 1.2) and takes the value a for every armchair tube and $\sqrt{3}a$ for zigzag tubes, where a =2.46 Å is

Type	(n,m)	atoms/unit cell	diameter (Å)
armchair	(2,2)	8	2.7
	(10,10)	40	13.6
zigzag	(4,0)	16	3.1
	(10,0)	40	7.8
chiral	(3,1)	52	2.8
	(10,9)	1084	12.9

Table 4.1: Structural properties of some examples of carbon nanotubes. The smallest nanotube that has been observed has a diameter of 3 Å [59]. There are three possible structures for it: (2,2), (4,0), or (3,1). Theoretical calculations of formation energies indicate that (n, n) armchair tubes for $n = 8 - 12$ are the most stable SWCNT species in their diameter range.

the lattice constant of graphene. Since we have $2N$ carbon atoms in the basis, the dynamical matrix to be solved becomes a $6N \times 6N$ matrix. Due to the large dimension of the dynamical matrix the diagonalization can be performed only numerically. The phonon-dispersion curves consist of $6N$ branches resulting from a vector displacement of each carbon atom in the unit cell. The big $6N \times 6N$ dynamical matrix is composed by $(2N)^2$ small 3×3 matrices, which couple only two atom types and are indicated as $D^{Ai,Bj}$, $D^{Ai,Aj}$, $D^{Bi,Aj}$, and $D^{Bi,Bj}$. These are the Fourier transforms of the force-constant tensors of pairs of atoms. Within the approximation of short-range interactions, we need therefore, for every single atom in the unit cell, the force-constant tensors describing the interactions with its nearest neighbors.

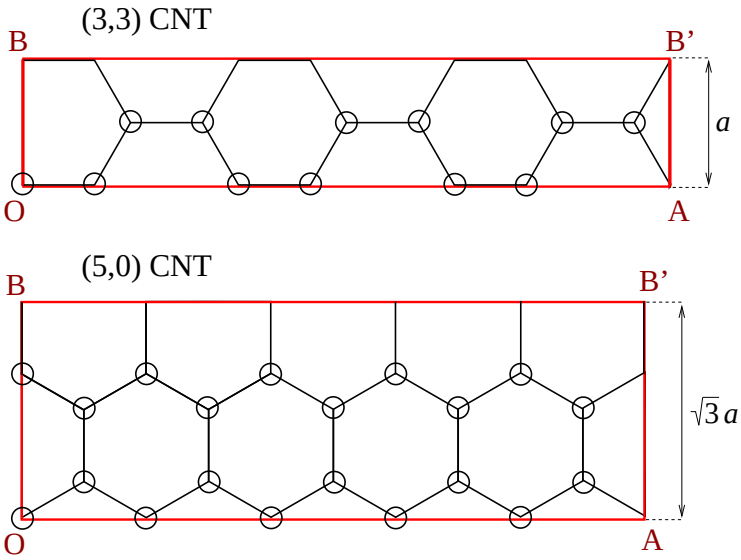

Figure 4.1: Unit cells of a (3,3) CNT and a (5,0) CNT: the rectangle has to be rolled up so that O coincides with A and B with B', forming a finite-size cylinder. For these two examples the diameters are 4.1 Å and 3.9 Å, respectively. The circles indicate the atoms of the basis. The length of the unit cell is a for armchair CNTs and $\sqrt{3}a$ for zigzag CNTs, where $a = 2.46$ Å.

4.2 Armchair nanotubes

In this Section we discuss the specific case of armchair (n, n) nanotubes. To describe the interaction between the atoms we consider the two force-constant models already introduced for graphene: The three-parameter model of Mahan and Jeon (MJ) and the fourth-nearest-neighbor approach (4NNFC) with the direct parametrization of the real-space force constants.

4.2.1 Mahan-Jeon model for carbon nanotubes

This force-constant model presented by Mahan and Jeon [28] for carbon nanotubes contains just three adjustable parameters: two for first- and second-nearest-neighbor directed bonds (with force constants k_1 and k_2), and a third for radial bond-bending interactions (k_3). The three potential-energy terms have been introduced in Sec. 3.2.2, Eq. (3.5 - 3.6). In the following, we use Mahan's notation where the tube axis is parallel to the z direction. The vector $\widehat{n}_{ij}$ in the expression for bond-bending interactions points in a radial direction with respect to the tube axis, at the midpoint of the bond between two atoms. It is given by $\widehat{n}_{ij} = \widehat{z} \times \widehat{\delta}_{ij}$.

It is convenient to use a systematic coordinate labeling, defined as follows: The unit cell of an armchair (n, n) tube has n atoms of type A and n of type B. In two dimensions, the equilibrium positions of the atoms in the unrolled unit cell is given in terms of the graphene lattice vectors. Considering a graphene sheet in the xz plane, the lattice vectors are given by $\mathbf{a}_1 = a/2\,(\sqrt{3},\, 0,\, 1)$ and $\mathbf{a}_2 = a/2\,(\sqrt{3},\, 0,\, -1)$. For an armchair nanotube it results convenient to define the atom coordinates of the τth atom by $\mathbf{R}_\tau^{(0)} \equiv \mathbf{R}_{ml}^{(0)} = l\mathbf{a}_1 + m(\mathbf{a}_1 + \mathbf{a}_2)$, with m and l integers. We use this notation also after rolling the sheet into a cylinder: Now m defines the location of atom A along the circumference, while l denotes the position along the z axis of the nanotube. Figure 4.2 (panel (a)) shows it in two dimensions. When located on a cylinder surface, we can define an angle θ_1 along the circumference between an A and B atom, and an angle θ_2 between A and B atoms that are first neighbors, but displaced along the z direction. It is shown in Fig. 4.2 (panel (b)) where R is the radius of the tube and $d_0 = a/\sqrt{3}$ is the distance between neighboring atoms A and B. The angles θ_1 and θ_2 are easily obtained as a function of R and d_0. Defining $\theta_{ml} = (\theta_1 + \theta_2)(2m + l)$, the cartesian coordinates of atom A and of its first nearest neighbors in the nanotube are given by:

$$\mathbf{R}_{A,ml}^{(0)} = [R\cos(\theta_{ml}),\, R\sin(\theta_{ml}),\, cl] \tag{4.1}$$

$$\mathbf{R}_{B1,ml}^{(0)} = [R\cos(\theta_{ml} + \theta_1),\, R\sin(\theta_{ml} + \theta_1),\, cl] \tag{4.2}$$

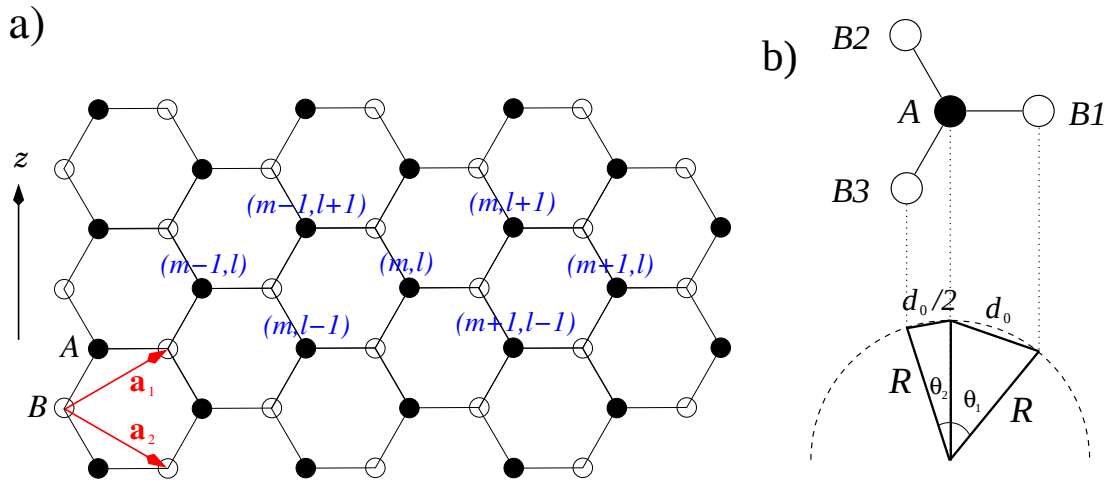

Figure 4.2: Panel (a): Atom equilibrium coordinates $\mathbf{R}^0_{ml} = l\mathbf{a}_1 + m(\mathbf{a}_1 + \mathbf{a}_2)$ in an armchair nanotube. z denotes the tube axis. Panel (b): View of a cut through the nanotube, showing the angles between Atom A and its first nearest neighbors $B1$, $B2$, and $B3$.

$$\mathbf{R}^{(0)}_{B2,m-1,l+1} = [R\cos(\theta_{ml} - \theta_2),\ R\sin(\theta_{ml} - \theta_2),\ c(l+1)] \tag{4.3}$$

$$\mathbf{R}^{(0)}_{B3,m,l-1} = [R\cos(\theta_{ml} - \theta_2),\ R\sin(\theta_{ml} - \theta_2),\ c(l-1)] \tag{4.4}$$

where $c = \sqrt{3}d_0/2$. The six second nearest neighbors of atom A, ml are situated at $\mathbf{R}^{(0)}_{A,m,l+1}$, $\mathbf{R}^{(0)}_{A,m-1,l+2}$, $\mathbf{R}^{(0)}_{A,m-1,l+1}$, $\mathbf{R}^{(0)}_{A,m,l-1}$, $\mathbf{R}^{(0)}_{A,m+1,l-2}$, and $\mathbf{R}^{(0)}_{A,m+1,l-1}$.

In Ref. [28] Mahan and Jeon introduced collective coordinates, with two quantum numbers: one is the wave vector q along the tube axis and the other quantum number α expresses the angular dependence around the tube, such as $\sin(\alpha\theta)$ or $\cos(\alpha\theta)$, where θ is the polar angle around the tube. q is continuous in case of open boundary conditions, while α takes the values $\alpha = 0, \pm1, \pm2, \ldots, \pm n/2$ for a (n, n) CNT. The problem reduces to a 6×6 set of equations to be solved, where each eigenvalue depends on α. Since α takes n values, one gets $6n$ branches (*e.g.* 60 in a (10,10) CNT). These are only half of the total number of branches that are expected. The full dispersion is obtained by folding the branches once in the middle of the Brillouin zone. In our calculations we directly set up the full $6N \times 6N$ dynamical matrix and proceed by solving the secular problem.

4.2.2 Fourth-nearest-neighbor approach

We introduced this frequently used force constant model in Sec. 3.3. It was first developed for planar graphene based on the experimental data for graphite and then adapted

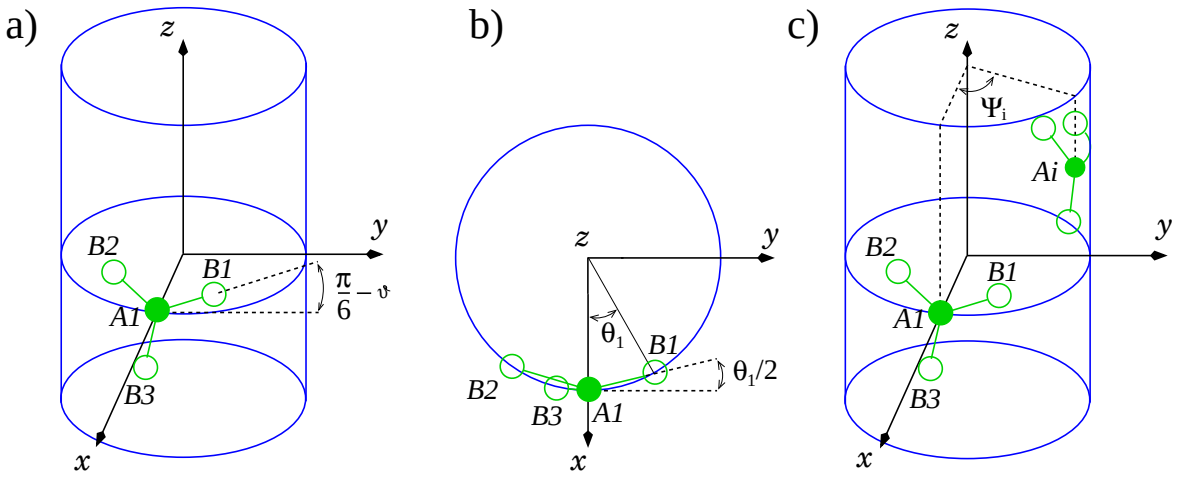

Figure 4.3: Rotation of the chemical bond $A1 - Bp$ from the two-dimensional plane of graphene to the three-dimensional coordinates of the nanotube. Panel (a) and (b) show how to rotate the bond $A1 - B1$: $A1$ is fixed on the x axis and atom $B1$ is first rotated by $\pi/6 - \vartheta$ around the x axis (panel (a)) and then by an angle $\theta_1/2$ around the z axis (panel (b)). ϑ is the chiral angle of the nanotube. This operation puts the $B1$ atom on the cylindrical surface of the nanotube. The force-constant tensor $\Phi^{(A1,Bp)}$ in the tube coordinate system is obtained by the corresponding rotation of the graphene force-constant tensor. The tensors for all the other atoms of the basis can be generated by rotating that of atom $A1$ by the corresponding angle Ψ_i around the nanotube axis (panel (c)).

for nanotube geometries [18, 13]. In this Section we present calculations of the phonon dispersion in carbon nanotubes that relied on the earlier determined force constants of graphene, which, as mentioned, are not correct for some parts of the optical phonon dispersion.

As we already showed, the dynamical matrix is composed by $(2N)^2$ small 3×3 matrices, that are the $D^{Ai,Bj}$, $D^{Ai,Aj}$, $D^{Bi,Aj}$, and $D^{Bi,Bj}$ (with $i, j = 1 \ldots N$), and to construct it we need the force-constant tensor for every single atom of the unit cell. Fortunately, it is enough to calculate it once, for one atom, and then due to the nanotube symmetry it is possible to evaluate it for the other atoms of the basis with simple numerical methods. Firstly, it is necessary to calculate the force-constant tensor of atom $A1$ for the interactions with up to fourth nearest neighbors. The tensor of Eq. (3.7) describes the interaction between atoms in the plane and for nanotubes it has to be adapted because of the curvature of the walls. For example, we consider the interaction of atom $A1$ and $B1$, illustrated in Fig. 4.3 (panel (a)-(b)). We put atom $A1$ on the x axis and obtain $\Phi^{(A1,B1)}$ by a first rotation of the tensor of Eq. (3.7) by $\pi/6 - \vartheta$ around the x axis (panel (a)) and then rotating the tensor by an angle $\theta_1/2$ around

the z axis (panel (b)). Here ϑ is the chiral angle, defined in Sec. 1.2, which is zero for armchair nanotubes, and θ_1 is the angle between $A1$ and $B1$ around the circumference. In the same way, we obtain the other tensors $\Phi^{(A1,Ap)}$ and $\Phi^{(A1,Bp)}$, where Ap and Bp are within the fourth-neighbor distance.

As next step we can generate the force-constant tensors for all the other atoms of the basis from those related to $A1$. For atoms of type A we must rotate the tensors of atom $A1$ by an angle Ψ_i around the z axis of the nanotube:

$$\Phi^{(Ai,Bp)} = U_z^{-1}(\Psi_i)\,\Phi^{(A1,Bp-i+1)}\,U_z(\Psi_i). \tag{4.5}$$

Ψ_i is the polar angle between $A1$ and Ai around the circumference. See also Fig. 4.3 (panel (c)). If $(p-i+1)$ is negative or zero we use $(N+p-i+1)$ instead of it. For atoms of type B we must rotate the tensors of atom $A1$ first by π around the x axis, and then by Ψ_i around the z axis, as before:

$$\Phi^{(Bi,Ap)} = U_z^{-1}(\Psi_i)\,U_x^{-1}(\pi)\,\Phi^{(A1,Bp-i+1)}\,U_x(\pi)\,U_z(\Psi_i) \tag{4.6}$$

where $U_z(\psi)$ and $U_x(\psi)$ are defined as:

$$U_z(\psi) = \begin{pmatrix} \cos\psi & \sin\psi & 0 \\ -\sin\psi & \cos\psi & 0 \\ 0 & 0 & 1 \end{pmatrix} \tag{4.7}$$

$$U_x(\psi) = \begin{pmatrix} 1 & 0 & 0 \\ 0 & \cos\psi & \sin\psi \\ 0 & -\sin\psi & \cos\psi \end{pmatrix}. \tag{4.8}$$

The dynamical matrix is obtained by multiplying the force constant tensors obtained above by $\exp(iq_z nT)$, where n is the number of the unit cell in which atom $A1$ is situated, and $T = |\mathbf{T}|$ is the modulus of the translational vector.

4.2.3 Detailed study for (10,10) CNTs

We proceed considering the results for a specific nanotube, a (10,10) CNT. This case is particularly interesting because the majority of theoretical calculations choose this tube as an example, motivated by the great amount of experimental data attributed to this particular tube. The (10,10) CNT has 40 atoms in the unit cell and the dynamical matrix has the dimension 120×120. The phonon dispersion consists of 120 branches. We calculate the dispersion with the MJ model and the 4NNFC model with both the parameters of Saito and coworkers (Table 3.1) and our parameters (Table 3.2).

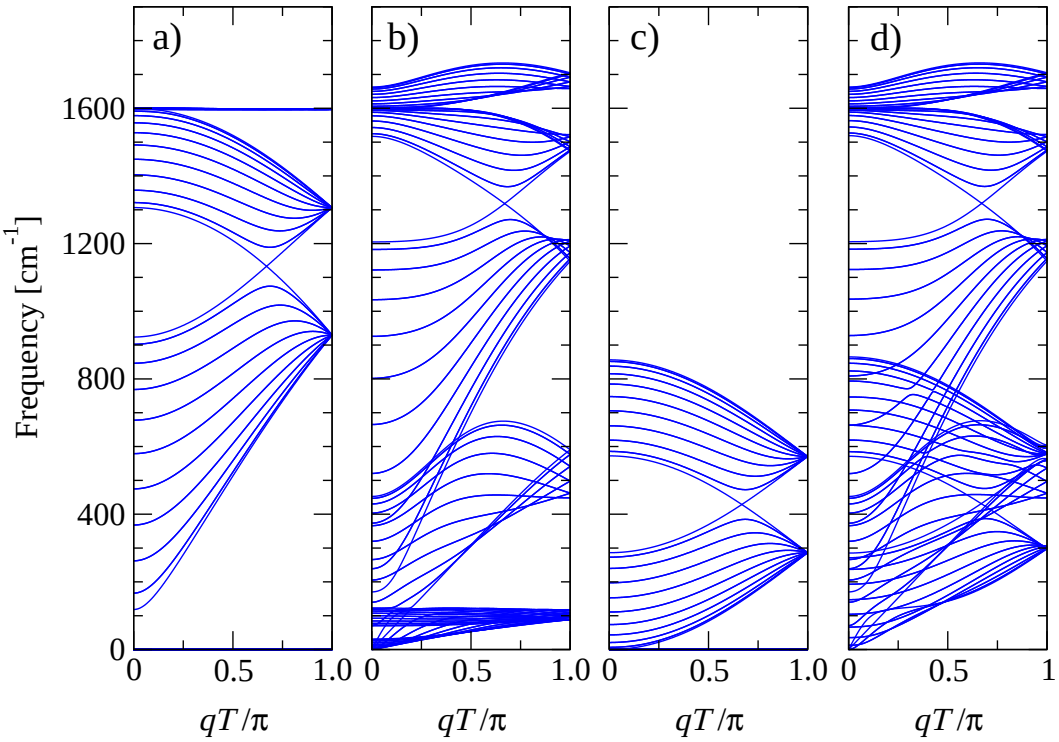

Figure 4.4: Contribution of every single potential-energy term of the MJ model to the dispersion curves of a (10,10) CNT. The curves are plotted using respectively: panel (a) bond stretching for first-nearest-neighbor atoms, panel (b) bond stretching for first and second-nearest-neighbor atoms, panel (c) only bond bending, panel (d) the final dispersion calculated with bond-stretching and bond-bending terms. The high-energy optical modes are purely stretching modes, while the acoustic modes and the low-energy region are determined by a combination of bond bending and bond stretching of 2nd-nearest-neighbors.

In the MJ model it is possible to consider separately the contribution of stretching and bending forces to the final dispersion relation. Figure 4.4 (panel (a)) shows the dispersion including only stretching forces between nearest-neighbor springs: 60 modes have zero frequency. A much better results is obtained by including also second nearest neighbors, as seen in Fig. 4.4 (panel (b)). Bond-bending forces alone are not able to describe a nanotube: they describe only low-frequency vibrations. The corresponding dispersion of panel (c) shows 21 distinct non-zero modes. In panel (d) is shown the final result, obtained by including all three potential energy terms. The bond-bending term is responsible only for the low-energy branches, while the high-energy optical phonons are determined only by stretching forces. The solutions are obtained by taking the square root of the eigenvalues of the dynamical matrix. We set the solution $\sqrt{3}$ to be the high-frequency optical phonon at $1600\,\mathrm{cm}^{-1}$; this fixes the value of the parameter

k_1. In Ref. [28] Mahan and Jeon assert that the relative weights of the three interactions are $k_2/k_1 = 0.06$ and $k_3/k_1 = 0.024$ for a (10,0) CNT, but the corresponding figure shows a dispersion that we obtain using $k_2/k_1 = 0.12$ and $k_3/k_1 = 0.024$.

It is interesting to compare directly the phonon dispersion of the MJ model and the 4NNFC approach with the parameters of Saito and coworkers. The obtained phonon-dispersion curves and the density of states (DOS) for the (10,10) CNT are shown in Fig. 4.5. For the former we obtain 65 distinct phonon branches, of which 10 modes are non-degenerate and 55 are doubly degenerate. For the latter we obtain 12 non-degenerate and 54 doubly degenerate modes.

The periodic boundary condition on the circumferential wave vector splits the modes into 1D quantized subbands that translate into the sharp spikes in the DOS, or one-dimensional van Hove singularities. A clear difference between the two models is the DOS at $\omega = 0\,\mathrm{cm}^{-1}$. Since there is a q^2 dependence in the acoustic modes of the MJ model, we get a singularity at $\omega = 0$, while in the 4NNFC model all acoustic modes have a linear q dependence and the DOS is finite at $\omega = 0$. We can directly compare the results of graphene (see Fig. 3.9) and the (10,10) CNT within the 4NNFC approach: in graphene we obtained a q^2 dependence in the out-of-plane TA mode, which implies a finite DOS at $\omega = 0$, which is known as the two-dimensional Van Hove singularity at the band edge [60]. The magnitude of the DOS at $\omega = 0$ is greater in graphene than in nanotubes, because a graphene sheet is weaker to bending than a nanotube [61]. The most significant difference between the graphene and the nanotube spectra is found in the low-energy range. The DOS of graphene is smoother and nearly constant, while nanotubes present several peaks. The peak at ≈ 170 cm^{-1} appears only in the nanotube spectrum. It is attributed to the radial breathing mode which is unique to carbon nanotubes. It appears at 170.3 cm^{-1} in the MJ model and at 165.0 cm^{-1} in the 4NNFC model. Experimental results from Raman scattering are around 177 cm^{-1}. We will discuss later in Sec. 4.4 about this important mode. Experimental measurements of the vibrational DOS of carbon nanotubes were achieved by Rols and coworkers by inelastic neutron scattering [62].

The details of the dispersion of the acoustic modes around the Γ point are shown in panel (c) and (d). In a carbon nanotube there are four acoustic modes. The force constants are invariant under infinitesimal translations along and perpendicular to the tube axis, that leads to the translational sum rule of Eq. (2.31) and to three zero-frequency modes at $q = 0$. The infinitesimal rotational-invariance condition imposed on the force constants gives rise to a rotational sum rule and to an additional zero-frequency mode. For this reason there are four acoustic modes in a carbon nanotube, of which two are non-degenerate and one is doubly degenerate. Near the Γ point the

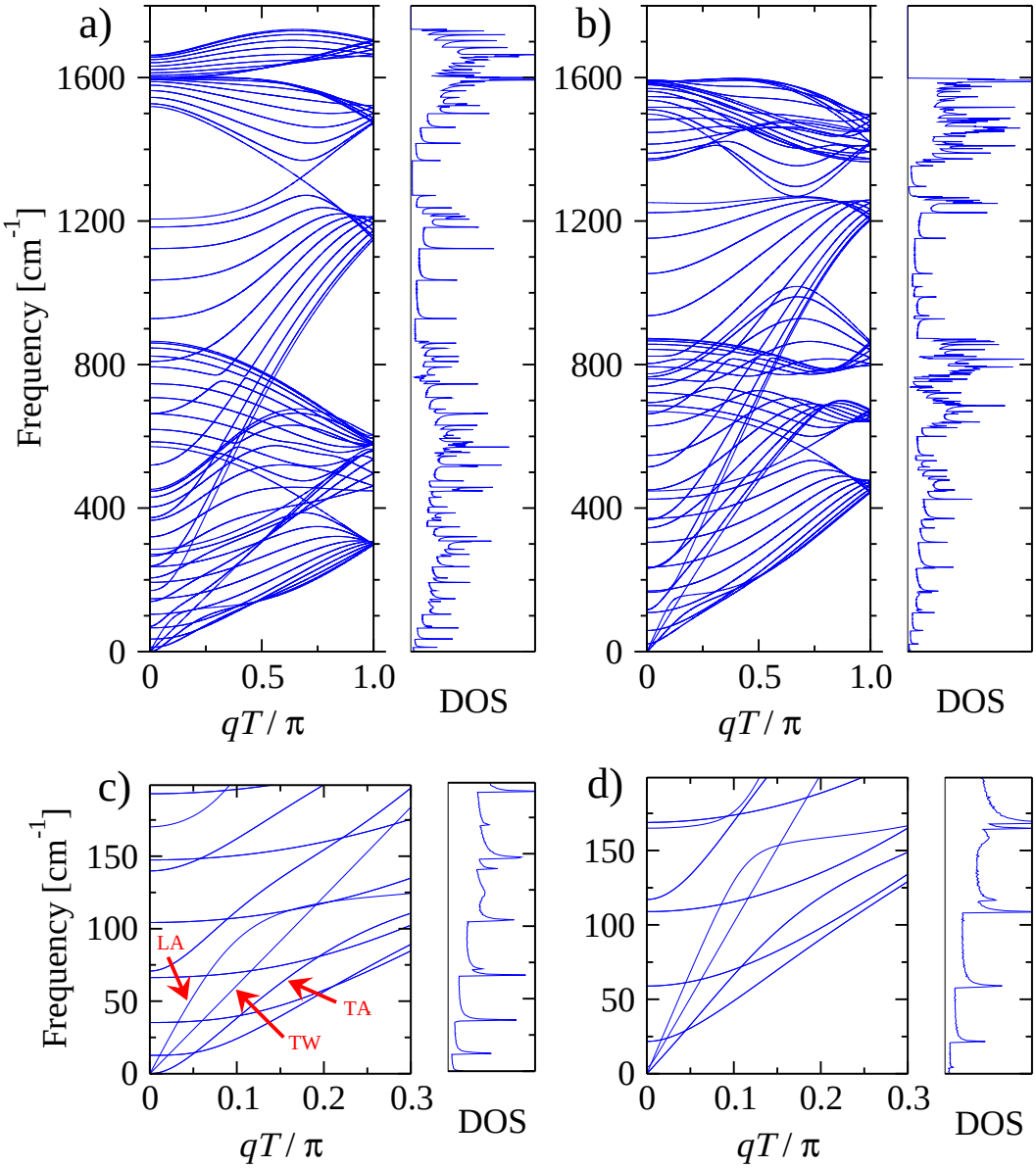

Figure 4.5: Phonon dispersion and vibrational density of states (DOS) for a (10,10) CNT calculated with the MJ model (panel (a)-(c)) and the 4NNFC approach (panel (b)-(d)) with the set of parameters of Saito *et al.*, listed in Table 3.1. T denotes the magnitude of the translational vector. Panel (c)-(d) show a zoom of the phonon dispersion near the Γ point: panel (c) shows four acoustic branches, where two increase linearly with q (LO, TW) and two are degenerate (TA) and increase quadratically. In panel (d) all four acoustic modes have linear dispersion for small wave vectors. Due to the fact that the effect of curvature is not yet completely included in the force constants, the frequency of the rotational acoustic mode (TW) is not exactly zero at $q = 0$ but ≈ 4 cm^{-1} (it gives an additional peak in the DOS).

highest-energy mode is the longitudinal acoustic (LA) mode, followed by a twisting or torsional mode (TW). The lowest energy modes are the transverse acoustic (TA) or flexure modes, which are doubly degenerate. For infinitely long wavelength ($q \to 0$), these correspond respectively to a rigid translation along the tube axis, a rigid rotation around the tube axis and rigid translations perpendicular to the axis. We will analyze them in more detail in Sec. 4.5.

The four acoustic modes are important contributors to the low-temperature specific heat and quantized phonon-thermal conductance, as we will see in Chap. 5. Although the exact dispersion law is apparently irrelevant for the quantized thermal conductance, the quadratic dispersion of the flexure modes, which leads to the one-dimensional singularity of the vibrational density of states at zero frequency, results in a very different behavior of the low-temperature specific heat. The q^2 dependence of the flexure modes obtained by several *ab initio* calculations [46, 48, 57] has been reproduced only by few other force-constant models [35, 55] which use much more parameters than the MJ model. The 4NNFC approach in Fig. 4.5 (panel (d)) shows a linear dispersion for all four acoustic modes. Furthermore, the calculated frequency at $q = 0$ for the rotational acoustic mode (TW) is not zero as it must be, but has a finite value of ≈ 4 cm^{-1} for the (10,10) CNT. This is a deficiency of the model, caused by the fact that the effect of curvature is not perfectly included in the force constants. The rotational sum rule is not satisfied. A new scaling for the force constant parameters was proposed in order to treat the curvature effect correctly [13]. Using this correction, Saito *et al.* realized that the frequency of the rotational acoustic mode shifts and becomes zero, while the correction to the higher-frequency modes is very small (less than 5 cm^{-1}). We do not apply the same rescaling, but vary only the force constant ϕ_{to}, which is the one that changes the most when passing from graphene to nanotubes. In graphene ϕ_{to} describes forces perpendicular to the plane. In a nanotube, the component of this force constant in the direction perpendicular to the cylindrical surface decreases with increasing θ, as illustrated in Fig. 4.6, and thus becomes more relevant the farther are the neighbors. In order to obtain the same amplitude of the motion in this direction as is obtained in the case of graphene, one has to take $\phi_{to}/\cos(\theta/2)$ instead of ϕ_{to}. The correction becomes large with increasing bond length or increasing θ, because the corresponding bond length becomes shorter than in the graphene plane. This correction depends on the bond length and describes vibrations perpendicular to the cylindrical surface. We approximate this correction applying it only to fourth nearest neighbors, and vary empirically $\phi_{to}^{(4)}$ in order to obtain zero frequency for the rotational acoustic mode. For a (10,10) nanotube we obtain a frequency of the twisting mode of $\omega \simeq 10^{-3}$ cm^{-1} at $q = 0$, setting $\tilde{\phi}_{to}^{(4)} = \phi_{to}^{(4)}(1 + \varepsilon)$ where $\varepsilon \sim 5.122 \cdot 10^{-3}$.

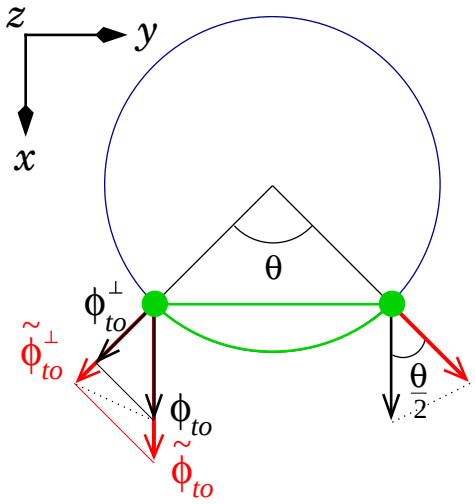

Figure 4.6: Correction of the out of plane force constant ϕ_{to}. The figure shows a cut through the nanotube along the circumference. After rolling up a graphene sheet, due to the curvature the effective bond length becomes shorter. Taking $\tilde{\phi}_{to} = \phi_{to}/\cos(\theta/2)$ instead of ϕ_{to}, it is possible to obtain the same amplitude of the motion in a radial direction as is obtained in graphene in the direction perpendicular to the sheet: $\tilde{\phi}_{to}^{\perp} = \phi_{to}$.

Now we consider the new parametrization of the 4NNFC model that we proposed for graphene in Sec. 3.4, and apply it to nanotubes. In agreement with the previous parametrization we obtain 10 non-degenerate and 55 doubly degenerate modes. While the high-energy optical phonons do not vary significantly, an interesting effect happens for the acoustic modes: the two degenerate TA modes now show the correct quadratic dispersion near the zone center, which was not given with the previous parametrization. Since the acoustic TW mode has a finite frequency at $q = 0$ also in our parametrization, we adjust the force constant ϕ_{to} as above. The quadratic modes are very sensitive to changes in the parameters, and it is not enough to correct ϕ_{to} only for the fourth nearest neighbors, but also for third and second neighbors. For the latter the correction is smaller, because these are less affected by the effect of curvature. The application of the correction procedure for the second, third, and fourth nearest neighbors[1] results in a frequency of the TW mode $\omega \simeq 10^{-1}$ cm^{-1} at $q = 0$. Figure 4.7 shows the result, in direct comparison with the result of the parametrization of Saito and coworkers including our correction. We will discuss later in Sec. 4.5 about the nature of the modes.

4.3 Zigzag nanotubes

In this Section we consider the other type of achiral nanotubes: the zigzag $(n, 0)$ carbon nanotubes. We described the 4NNFC model applied to armchair nanotubes in the previous Section. It can be applied easily also to zigzag nanotubes with only a few changes. In order to obtain the force-constant matrices of atom $A1$ it is possible

[1]The correction to ϕ_{to} is $\varepsilon \sim 9.0 \cdot 10^{-3}$, $9.5 \cdot 10^{-3}$, and $1.42 \cdot 10^{-2}$ for second, third, and fourth nearest neighbors, respectively.

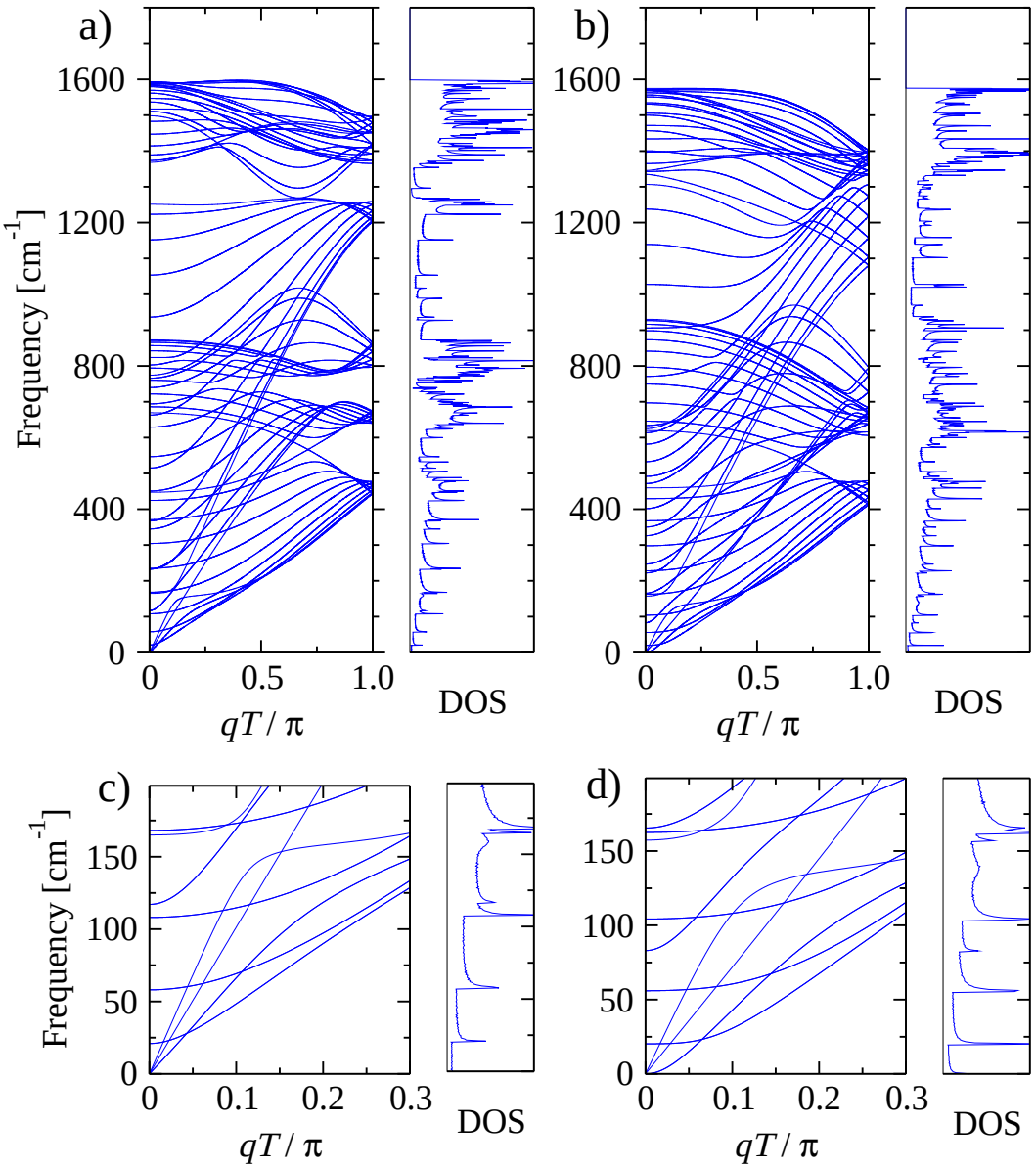

Figure 4.7: Phonon dispersion and vibrational density of states (DOS) for a (10,10) CNT calculated with the 4NNFC model with the parametrization of Saito *et al.* (panel (a)-(c)) and our new parametrization (panel (b)-(d)), given in Table 3.2. Both have been corrected in order to obtain $\omega = 0$ at $q = 0$ for the acoustic TW mode. Panel (c)-(d) show the low frequency phonon band structure. The 1D quantized nature of the band structure is evident: there are a series of 1D quantized subbands. The most important difference between the two calculations is the behavior of the TA modes: in panel (c) these show linear dispersion, resulting in a finite DOS at $q = 0$, while in panel (d) their dispersion is quadratic, which reflects in a singularity in the DOS. The DOS increases stepwise with the entry of higher subbands.

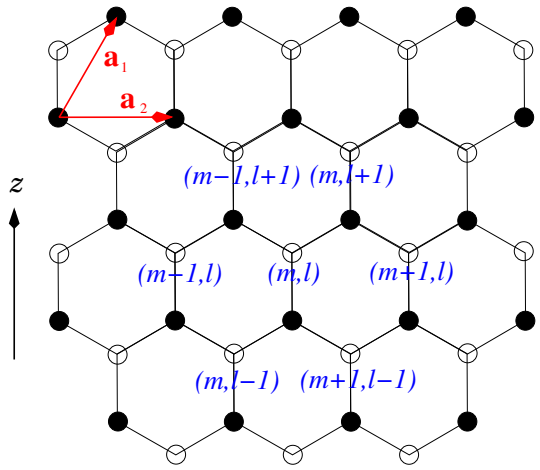

Figure 4.8: Coordinate labeling of atoms in a zigzag nanotube. Each atom of type A or B is denoted by a pair of integers (m, l), and its equilibrium position is given by $\mathbf{R}^0_{ml} = l\mathbf{a}_1 + m(\mathbf{a}_1 + \mathbf{a}_2)$.

either to rotate all the force constant matrices of atom $A1$ for armchair nanotubes by 90° or to change only the axes and let x be the direction of the nanotube axis. The force-constant matrices of the other atoms can be obtained as for armchair nanotubes, by rotating those of atom $A1$ by the appropriate angles.

The MJ model provides a new labeling that is specific for zigzag nanotubes. As for armchair nanotubes, the atom coordinates are given in terms of graphene lattice vectors: $\mathbf{R}^0_{ml} = l\mathbf{a}_1 + m(\mathbf{a}_1 + \mathbf{a}_2)$ as illustrated in Fig. 4.8. Now the angle between two lattice points (two atoms of type A or two of type B) around the circumference is $\theta_z = 2\pi/n$. Defining now $\theta_{ml} = \theta_z(m + l/2)$ and $c = 3d_0/2$, the cartesian coordinates of atom A and its first nearest neighbors $B1$, $B2$, and $B3$ in the nanotube become:

$$\mathbf{R}_{A,ml} = [R\cos(\theta_{ml}),\ R\sin(\theta_{ml}),\ cl] \tag{4.9}$$

$$\mathbf{R}_{B1,ml} = [R\cos(\theta_{ml} + \theta_z/2),\ R\sin(\theta_{ml} + \theta_z/2),\ cl + d_0/2] \tag{4.10}$$

$$\mathbf{R}_{B2,m-1,l} = [R\cos(\theta_{ml} - \theta_z/2),\ R\sin(\theta_{ml} - \theta_z/2),\ cl + d_0/2] \tag{4.11}$$

$$\mathbf{R}_{B3,m,l-1} = [R\cos(\theta_{ml}),\ R\sin(\theta_{ml}),\ cl - d_0] \tag{4.12}$$

The six second nearest neighbors are situated at $\mathbf{R}_{A,m+1,l}$, $\mathbf{R}_{A,m,l+1}$, $\mathbf{R}_{A,m-1,l+1}$, $\mathbf{R}_{A,m-1,l}$, $\mathbf{R}_{A,m,l-1}$, and $\mathbf{R}_{A,m+1,l-1}$. We construct the bond-stretching and bond-bending terms as before but now for the zigzag geometry.

4.3.1 Detailed study for (10,0) CNTs

We consider both models presented above for calculating the phonon modes of a (10,0) CNT. It has 40 atoms in the unit cell as the (10,10) CNT, but smaller diameter and a longer unit cell (see Table 4.1 and Fig. 4.1). In the MJ model the relative weight for the three interactions was set to $k_2/k_1 = 0.12$ and $k_3/k_1 = 0.024$, as for the (10,10) CNT. In Ref. [28] Mahan and Jeon assert that the relative weights for a (10,0) CNT

are $k_2/k_1 = 0.09$ and $k_3/k_1 = 0.033$ but we obtain his dispersion curves using the firstly mentioned weights. The overall scaling of the dispersion curves was fixed by setting the solution $\sqrt{3}$ to be the optical phonon at 1600 cm^{-1}. For the 4NNFC model we used the same parameters as for the (10,10) CNT. We obtain again 66 distinct phonon branches, where 12 modes are non-degenerate and 54 are doubly degenerate. Figure 4.9 shows the results using the MJ model (panel (a)) and the 4NNFC model with the original parametrization of Saito and coworkers (panel (b)). As in the case of the (10,10) CNT, the MJ model gives a correct behavior of the four acoustic branches, with a q^2 dependence for the flexure modes (panel (c)). In the 4NNFC model occurs again the same problem in the low frequency region (panel (d)), as in the case of the (10,10) CNT: The rotational acoustic mode has a non-zero frequency ($\sim$ 21 cm^{-1}) for $q = 0$. As mentioned, it is due to the fact that the effect of curvature is not perfectly included in the force constants. This effect becomes more and more evident for CNTs with smaller diameter. Indeed, for the larger (10,10) CNT the effect is smaller, see Fig. 4.5 (panel (d)). In order to avoid such unphysical result, we use the same procedure we used for the (10,10) CNT. We vary empirically ϕ_{to} in order to obtain zero frequency for the rotational acoustic mode. We do this both for the parametrization of Saito and coworkers and for our own parametrization. The results are shown in Fig. 4.10. Considering first Saitos parametrization, for a (10,0) nanotube with a correction[2] to ϕ_{to} we obtain a frequency of the twisting mode of $\omega \simeq 10^{-3}$ cm^{-1} at $q = 0$. These factors are greater than for the (10,10) CNT: the correction must be stronger because of the smaller radius and the higher curvature effect of the (10,0) CNT. Considering our own parametrization we obtain as wanted the quadratic TA mode and $\omega \simeq 10^{-1}$ cm^{-1} at $q = 0$ for the TW acoustic mode.[3]

[2]The parameter ε was $\sim 9.0 \cdot 10^{-3}$, $9.5 \cdot 10^{-3}$, and $3.89 \cdot 10^{-2}$ for second, third, and fourth nearest neighbors, respectively

[3]The correction to ϕ_{to} was $\varepsilon \sim 9.5 \cdot 10^{-3}$, $1.0 \cdot 10^{-2}$, and $4.88 \cdot 10^{-2}$ for second, third, and fourth nearest neighbors, respectively

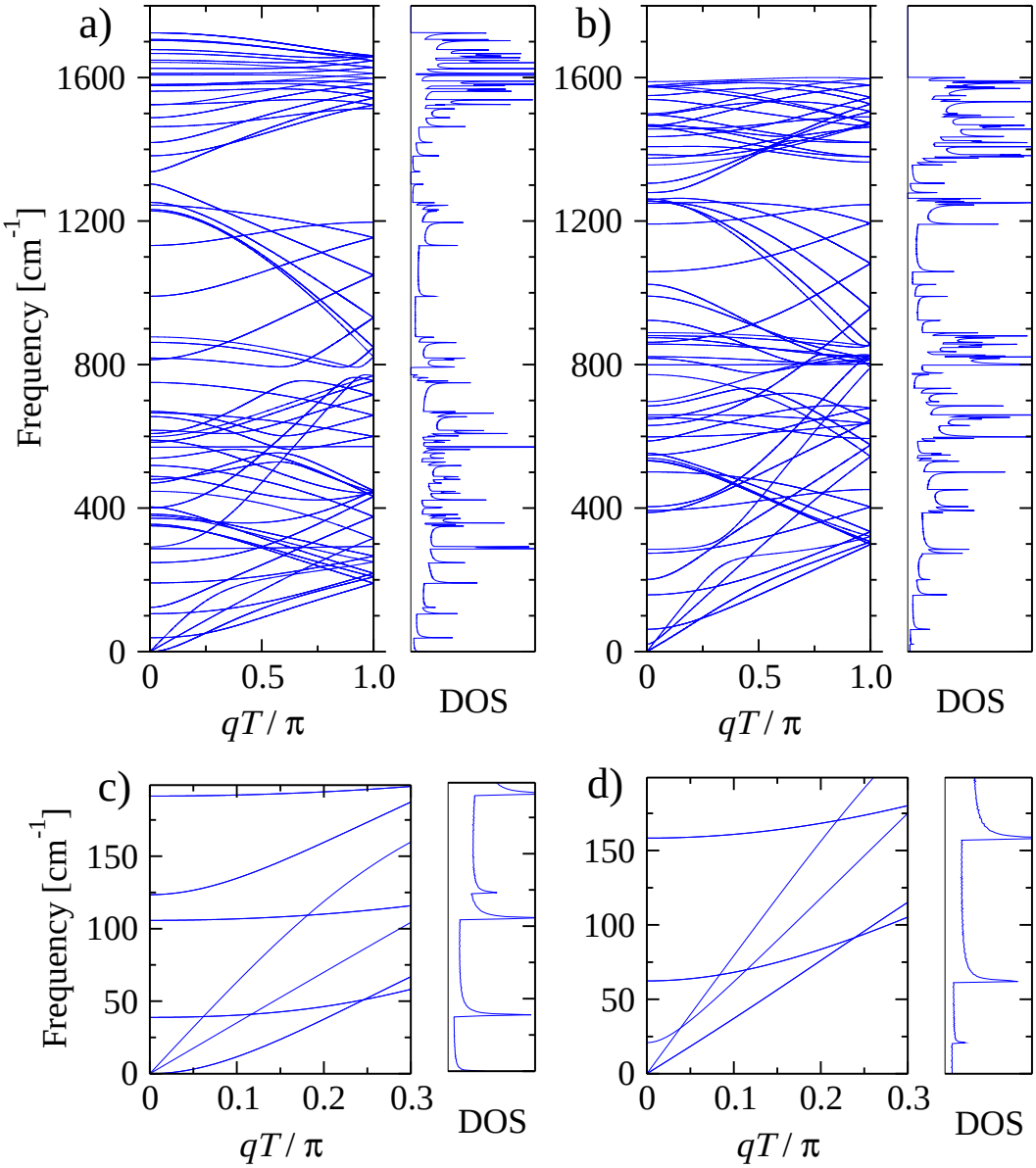

Figure 4.9: Phonon dispersion and vibrational density of states (DOS) for a (10,0) CNT, calculated with the force constant model of Mahan and Jeon (panel (a)-(c)), and the fourth nearest neighbor model (4NNFC) (panel (b)-(d)). Panel (c)-(d) show a larger scale representation of the low-frequency region. Only the calculation within the MJ model gives a quadratic dispersion for the transverse acoustic (TA) modes. In the 4NNFC model all acoustic modes have linear dispersion for small wave vectors. The rotational TW mode has not zero frequency at $q = 0$ as it must be, but actually ~ 21 cm^{-1}. This effect is larger than in the (10,10) CNT because of the smaller radius and the stronger curvature and it is also the origin of an additional spike in the DOS.

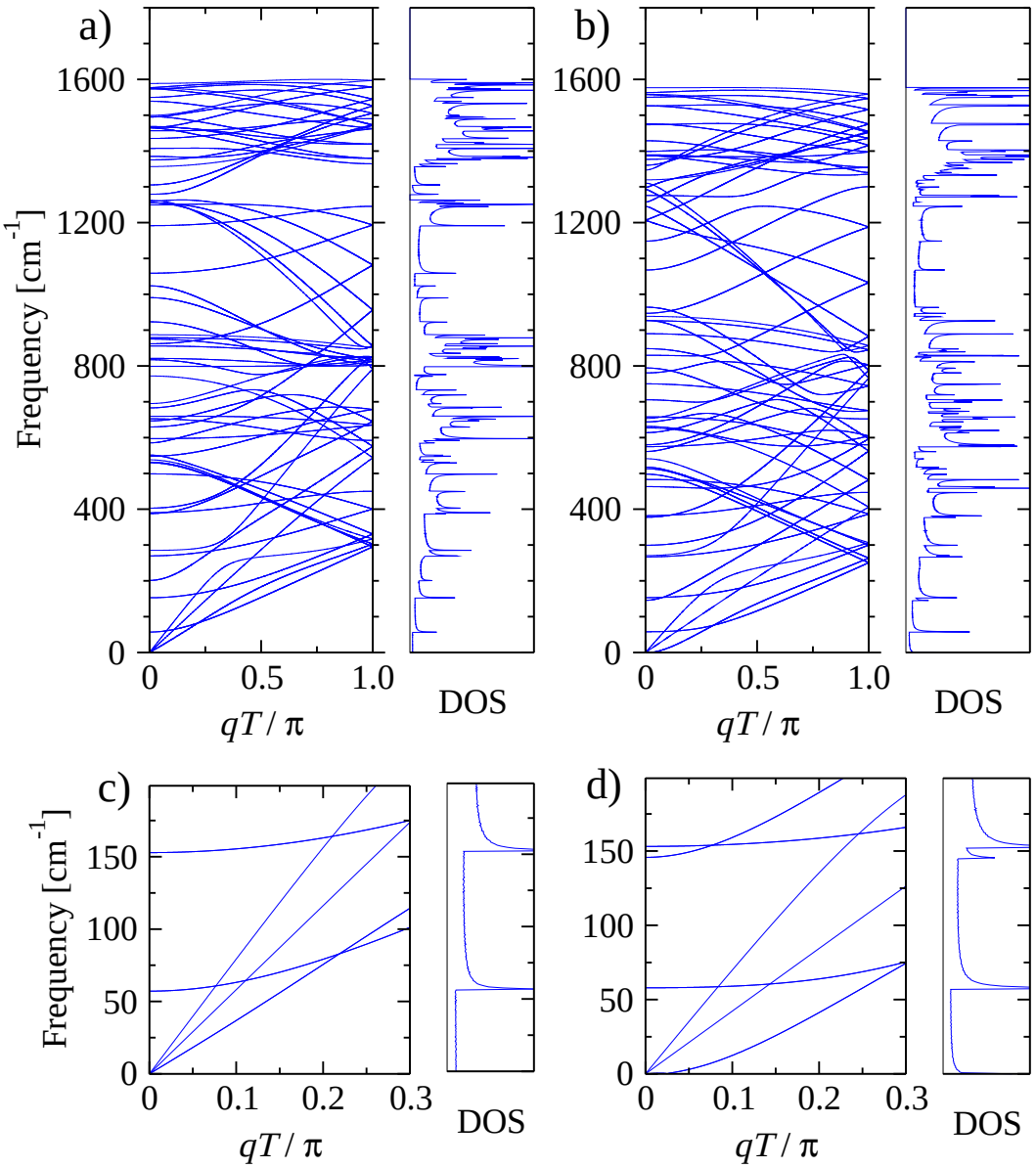

Figure 4.10: Phonon dispersion and vibrational density of states (DOS) for a (10,0) CNT calculated with the fourth-nearest-neighbor model. Panel (a)-(c) are obtained with the parametrization of Saito *et al.* and panel (b)-(d) with our new parametrization: they show respectively linear and quadratic dispersion for the TA modes. In both models the ϕ_{to} constants have been corrected in order to obtain zero frequency for the acoustic TW mode at the Brillouin-zone center.

4.4 Radial-breathing mode

The radial-breathing mode (RBM) arises from a radial expansion and contraction of the entire tube. This mode is unique to single-walled CNTs and is taken as indicative of the presence of nanotubes in a sample. Furthermore, it is the best known feature in the Raman spectra of carbon nanotubes [10] and plays an important role in experiments [63]. The RBM is often used to determine the diameter or diameter distribution in nanotube samples on the basis of Raman data, as it has a particularly simple relationship between its frequency and the tube diameter. We will show that the frequency of the RBM is proportional to the inverse diameter of the tube and independent of chirality. The expected dependence of the RBM frequency on diameter is:

$$\omega_{\mathrm{RBM}} = \frac{C_1}{d_t^{\kappa}} + C_2(d_t) \tag{4.13}$$

with C_1 a constant, C_2 possibly depending on diameter d_t and an exponent κ. This functional dependence was first introduced by Jishi *et al.* [41] with C_2=0 and κ=1. Several articles and a range of values of C_1 have been published, differing from each other by a few per cent. A review of the experimental and theoretical values can be found in Ref. [12]. For isolated tubes the values ranges from $C_1 = 218$ to 248 $\mathrm{cm}^{-1}\,\mathrm{nm}$.

We calculate the RBM frequencies of a number of armchair ($n = 3 - 12$) and zigzag ($n = 6 - 20$) nanotubes with the 4NNFC model with our parametrization. The obtained frequencies are almost perfectly inverse proportional to the radius of the tube as shown in Fig. 4.11 (panel (a)) and independent on chirality. The RBM frequency decreases with increasing tube diameter and becomes zero in the limit of infinite diameter, which corresponds to the out-of-plane tangential acoustic mode of graphene at $q = 0$. The reason is that the force needed for a radial deformation of a nanotube increases as the diameter decreases. By fitting the frequencies of the RBM to tube diameters by the inverse proportional relation of Eq. (4.13), we get negligible values for C_2 and $C_1 = 212\,\mathrm{cm}^{-1}\,\mathrm{nm}$ for armchair tubes (panel (b)), which is in satisfactory agreement with the experimental value of $224\,\mathrm{cm}^{-1}\,\mathrm{nm}$ [64]. For zigzag nanotubes (panel (c)) we get $C_1 = 209\,\mathrm{cm}^{-1}\,\mathrm{nm}$. The values of C_1 are in agreement also with previous calculations [54,57,65-67]. We did the same calculations also with the frequencies obtained by the original parametrization of Saito and coworkers. In Fig. 4.11 the results are plotted in green. We obtain $C_1 = 223\,\mathrm{cm}^{-1}\,\mathrm{nm}$ for armchair tubes and $C_1 = 222\,\mathrm{cm}^{-1}\,\mathrm{nm}$ for zigzag nanotubes. These are in better agreement with experimental values than our parametrization, since the RBM frequencies are somewhat higher.

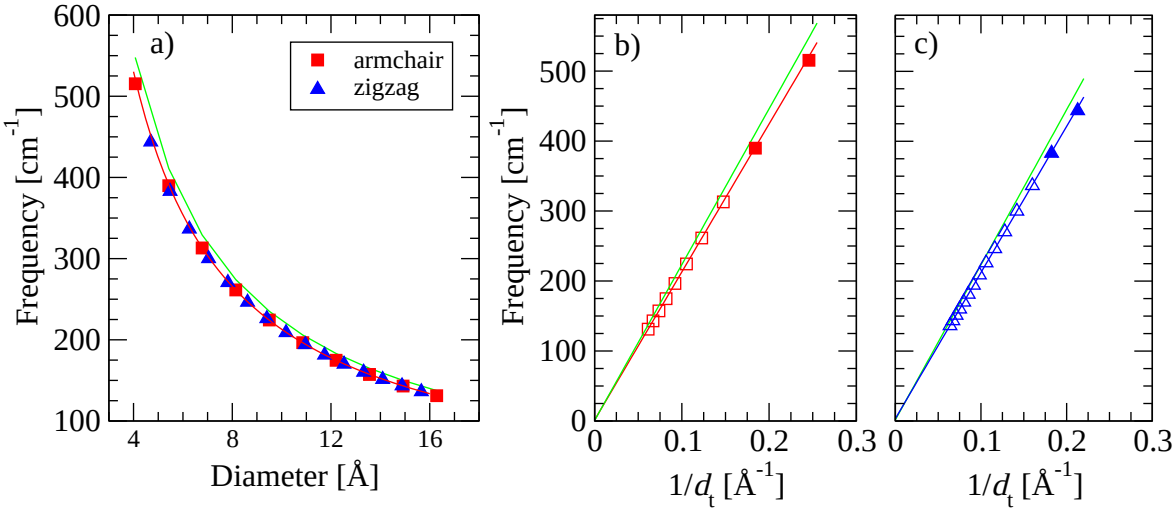

Figure 4.11: Panel (a): Frequency of the radial-breathing mode of various armchair ($n = 3 - 12$) and zigzag ($n = 6 - 20$) tubes as a function of the nanotube diameter, calculated with the 4NNFC model with our new parametrization. For comparison, the green line shows the results for the original parametrization of Saito. A possible chirality dependence, if any, is well below the resolution of the data. Panel (c) and (d) show the frequency of the RBM as a function of the inverse tube diameter for armchair and zigzag tubes, respectively. The solid lines are a linear fit to the data excluding the small-diameter tubes (3,3), (4,4), (6,0), (7,0), which are marked by filled squares and triangles. These present a deviation from the predicted behavior, with a decrease in the RBM frequency. Reference [57] explains it as a consequence of the hybridization changes and the decrease of the π interaction induced by the curvature.

The proportionality constant C_1 is almost the same for armchair and zigzag tubes, which suggests that there is no chirality dependence. This is due to the fact that the RBM corresponds to a stretching of the graphene sheet in the [110] (armchair tubes) or [100] (zigzag tubes) direction. Because the system is isotrope in the hexagonal plane, the elastic constant that the describes the stretching of a graphene sheet is independent on the direction [65]. Thus C_1 is the same for all tubes and the RBM frequency depends only on the diameter of the tube.

Also other low-frequency modes depend strongly on the tube diameter [13, 48]. Instead, the higher frequency modes do not have a strong dependence on the diameter since the frequencies of the higher optical modes are more sensitively determined by the local movements of the atoms.

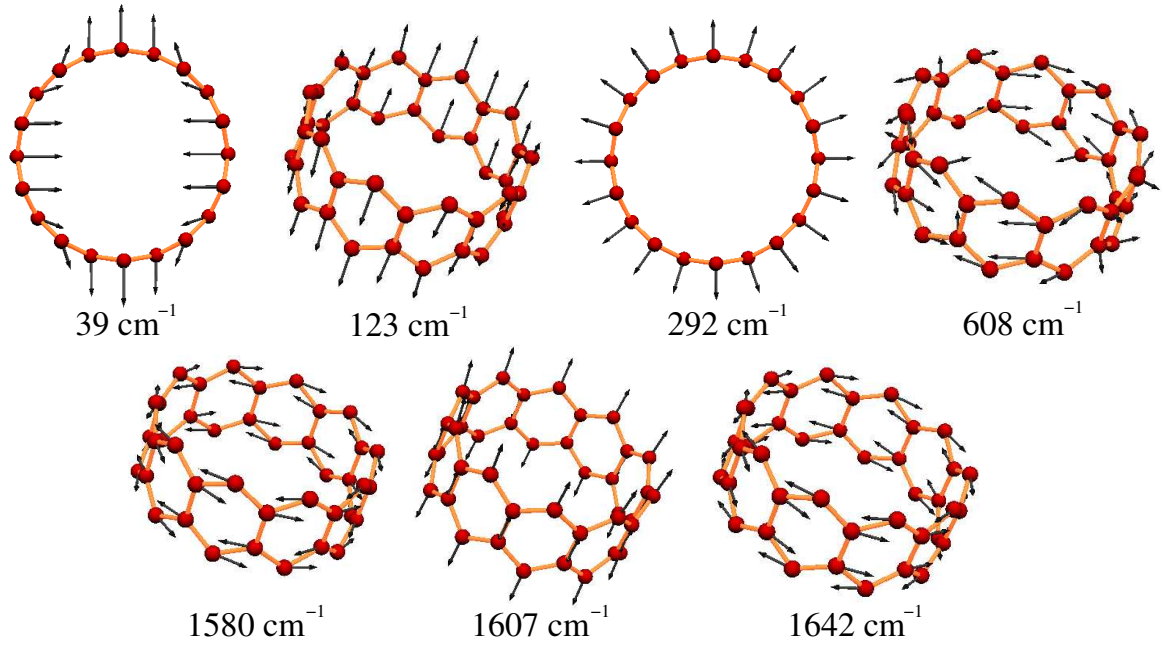

Figure 4.12: Raman-active normal mode eigenvectors and frequencies for a (10,0) CNT, calculated with the MJ model. These vibrational modes are the seven strongest Raman-active modes. The arrows indicate the magnitude and direction of the atomic displacements for $q = 0$.

4.5 Visualization of the vibrational modes

After studying the dispersion relations of carbon nanotubes, we want to know how the atoms do effectively move and proceed with visualizing their displacements. For this purpose we diagonalize the dynamical matrix as before for every q vector to obtain eigenfrequencies and eigenvectors. The latter contain the displacements of every basis atom, and can be represented graphically. Among the great variety of vibrational modes, we select significant examples for both the models that we presented above. We choose to visualize some of the Raman-active normal modes that show strong Raman intensity in experimental studies [10] (see also Sec. 1.3), and furthermore to have a look at the four acoustic modes. In Fig. 4.12 we show the normal mode displacements for the seven strongest Raman active modes for a (10,0) CNT at $q = 0$. Armchair nanotubes show equivalent kind of modes as the zigzag ones, which suggests that vibrational modes have no chirality dependence. Figure 4.13 shows three selected Raman active modes for a (10,10) CNT for $q = 0$, calculated with the MJ model. Panel (a) shows the lowest lying optical mode, whith E_{2g} symmetry [12, 13], in this mode the nanotube moves uniformly with an oval deformation of its cross section. In the previous Section we

introduced the radial-breathing mode (RBM) (A_{1g} symmetry), which is now illustrated in panel (b): All atoms move in phase in the radial direction creating a breathing-like vibration of the entire tube. A high-frequency optical mode with E_{2g} symmetry is shown in panel (c). It is clear that this mode is out-of-phase between nearest-neighbor atoms, while the other two modes of panel (a)-(b) show in-phase motion. Most of the low frequency modes have strongly diameter-changing movements, while the higher-frequency modes consist in local diameter-independent movements of the atoms. For direct comparison, Fig. 4.14 shows the same modes calculated with the 4NNFC model with our parametrization. These vibrations are much more complicated than those in Fig.4.13, since there is a considerable mode mixing. The RBM does not show purely radial movement, but has also a component of rotation around the tube axis. We found that the RBM is coupled to the acoustic TW mode, since both modes show breathing behavior combined with a rotational motion.

Finally, we consider the behavior of the four acoustic modes: the doubly degenerate transverse acoustic (TA) mode, the twisting (TW) mode and the longitudinal acoustic (LA) mode. These are shown for nonzero wave vector ($qT/\pi = 0.075$) respectively in panel (a), (b), and (c) of Fig. 4.15, on an expanded scale, to make them clearly visible. Since they are independent on chirality, we show zigzag (10,0) CNTs in panel (a) and armchair (10,10) CNTs in panel (b) and (c). The left (orange) tubes are calculated with the MJ model, the right (blue) ones with the 4NNFC model. In the MJ model the pure modes are clearly recognizable. For $q \neq 0$ the acoustic mode with lowest energy is the TA, in which the whole tube makes bending oscillations, or vibrates like a plucked string (the tube can be plucked in any direction perpendicular to its axis, so this mode is doubly degenerate). In the TW mode portions of the tube are rotated by varying amounts about the tube axis, therefore, it is called also torsional mode. It results from a translation of graphene along the chiral vector. The acoustic mode with highest frequency is the LA, in which the tube is stretched and compressed along its axis, as is clearly observable from the side view. In the 4NNFC model the mode mixing is evident: The TA mode represents bending oscillations with also a longitudinal component and is similar to the LA mode. The TW mode shows a breathing-like behavior with longitudinal component, but no torsion at all is present. We suggest that the MJ model provides a rather elementary, quick method, that with only three parameters and up-to second-nearest-neighbor interactions can reproduce only a simplified version of the true vibrational behavior. The 4NNFC model with 12 adjustable parameters and up-to fourth-nearest-neighbor interactions provides a much more realistic view. However, we emphasize that for an unequivocal representation one has to consider the eigenvectors and eigenfrequencies resulting from *ab initio* calculations.

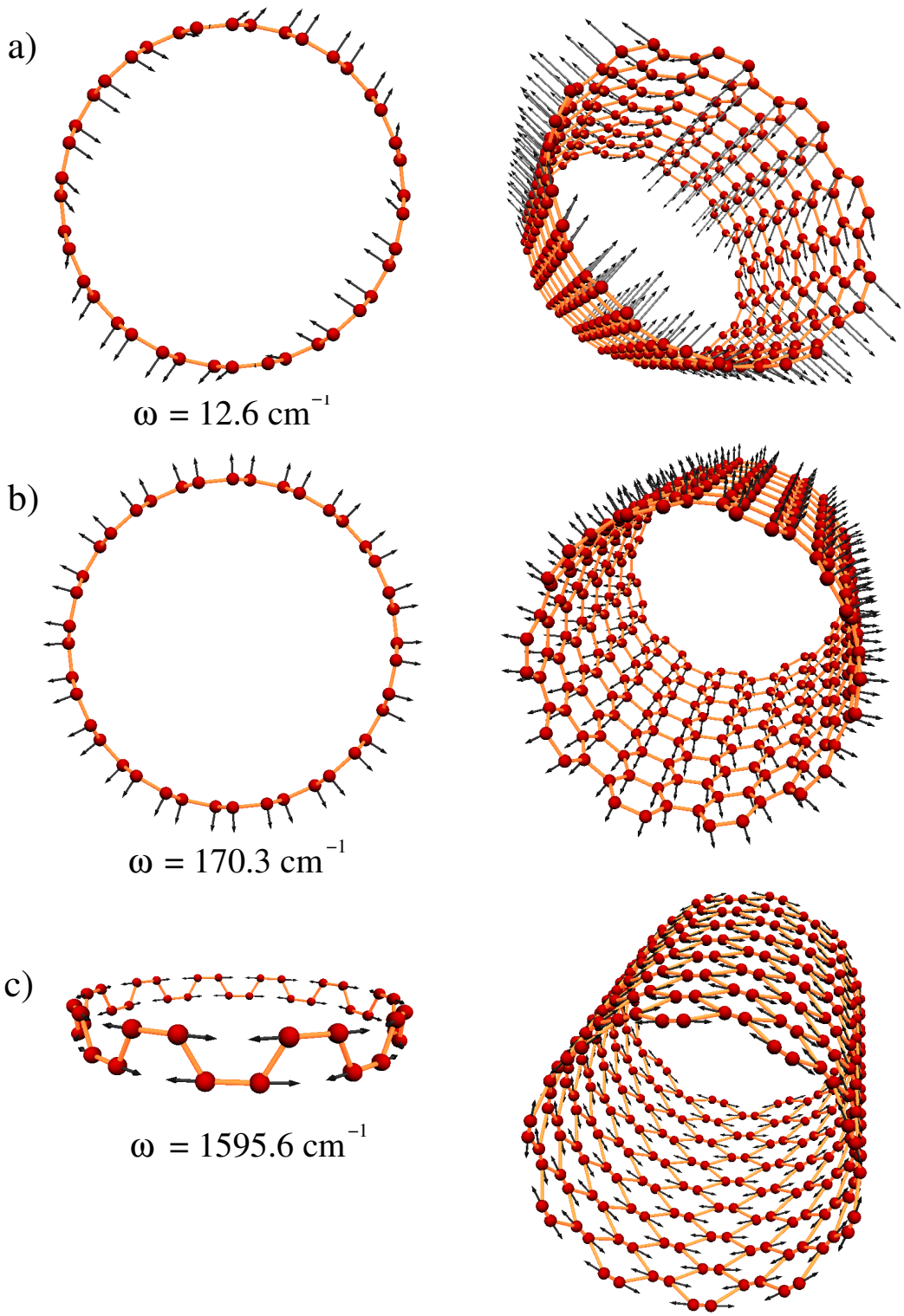

Figure 4.13: Selected Raman active vibrational modes of a (10,10) CNT, at $q = 0$, calculated with the MJ model. For more details see the text.

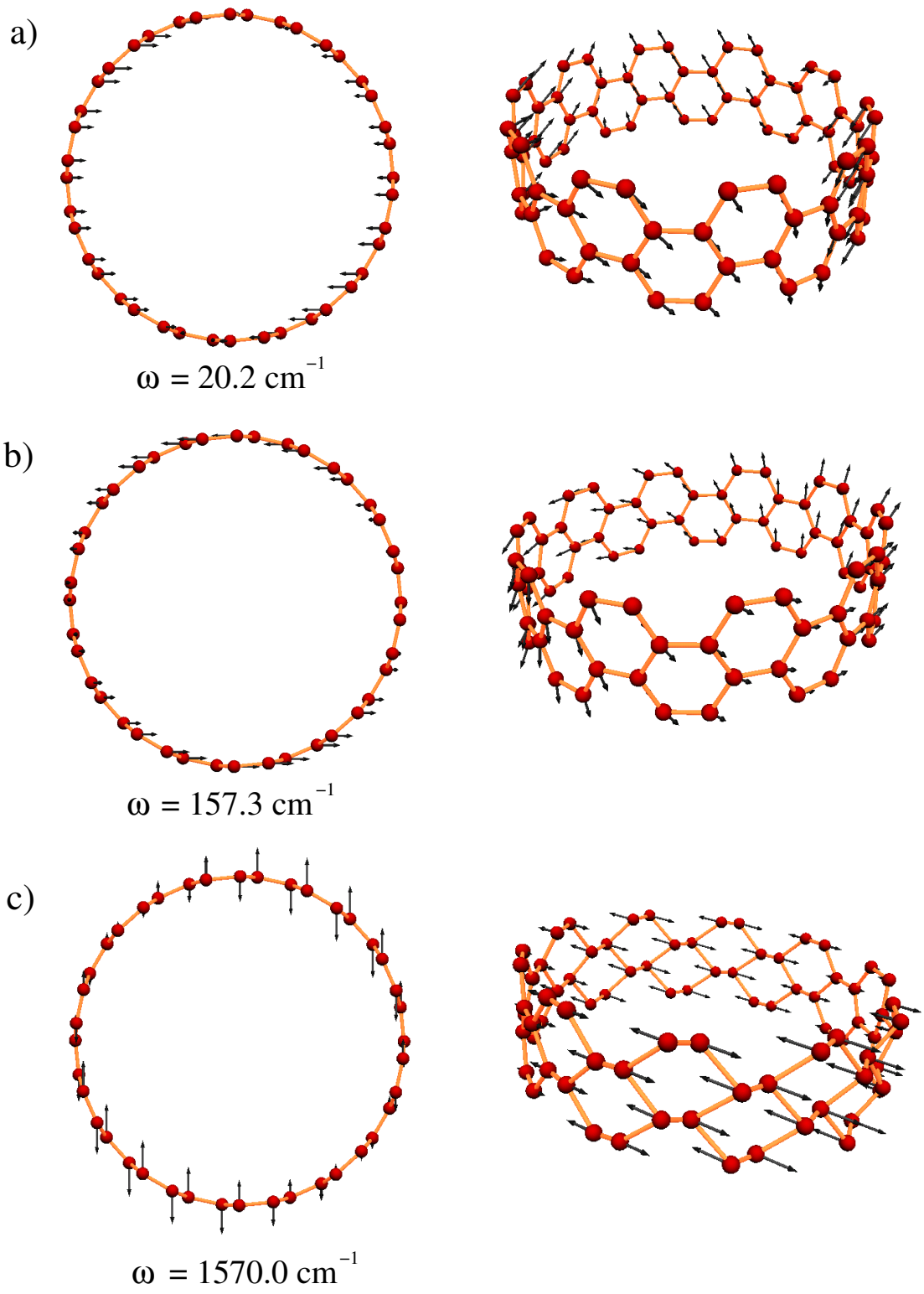

Figure 4.14: The same as in Fig. 4.13, calculated with the 4NNFC model.

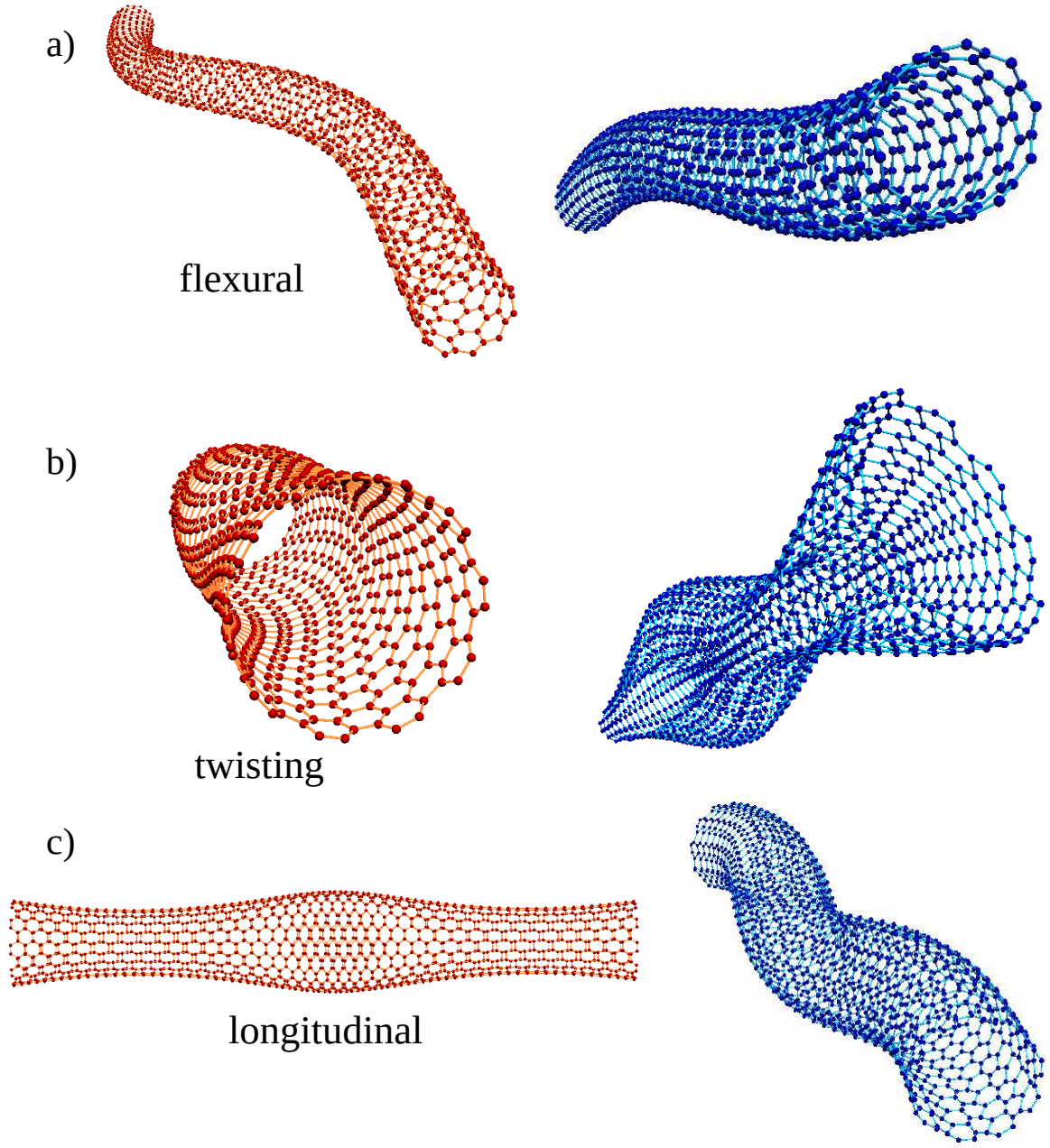

Figure 4.15: Acoustic modes for $q \neq 0$: the TA mode for a (10,0) CNT (panel (a)), the TW and the LA mode for a (10,10) CNT (panel (b)-(c)). The tubes on the left (orange) are calculated with the MJ model, that on the right (blue) with the 4NNFC model. See also the text for more details.

Chapter 5

Thermodynamics and phonon transport

The thermal properties of carbon nanotubes are directly related to their unique structure and small size. Because of these properties, nanotubes may prove to be an ideal material both for the study of low-dimensional phonon physics and for possible applications such as thermal management.

After explaining in Sec. 5.1 the role of anharmonicity in lattice dynamics, we turn to investigate the specific heat c_{V} of several carbon nanotubes in Sec. 5.2. The main contribution to the specific heat of a nanotube is the vibrational one, because the electronic one is negligible even at a few Kelvin [68]. We show that there is a close connection between the behavior of the acoustic modes, the phonon density of states, and the low-temperature specific heat. Section 5.3 deals with phonon heat transport in carbon nanotubes, investigated using a method analogous to the Landauer theory of electronic transport. We prove that in a low-temperature regime dominated by ballistic-phonon propagation the thermal conductance of a nanotube is quantized, the fundamental quantum of thermal conductance being $\pi^2 k_{\mathrm{B}}^2 T/(3h)$.

5.1 Temperature effects in lattice dynamics

Most of the temperature effects in solid-state physics have their origin in the anharmonicity of the lattice potential energy. However, the traditional theory of lattice dynamics is based on the assumption of small vibrational amplitudes of the atoms about their mean position. Under this condition, the properties of a crystal can be described accurately in the harmonic approximation: The potential energy of the lattice is expanded in powers of the ion displacements on their equilibrium positions and the expansion is terminated after the first nonvanishing (quadratic) term.

Within this approximation, the lattice vibrations can be decoupled by a transforma-

tion to normal coordinates. This leads, when the normal vibrations are quantized, to the concept of phonons as noninteracting excitations of the lattice. The decoupling is not possible when we take higher terms in the expansion of the potential. Generally, the anharmonic terms are small compared with the harmonic part of the Hamiltonian and their effect can be calculated within perturbation theory. They can be seen as perturbations which cause transitions between two harmonic states and lead to interactions between phonons. A phonon from a given state $(\mathbf{q}, s)$[1] will disappear after a finite time through a multi-phonon process, e.g. decay into other phonons. The phonons then have finite lifetime. At the same time, the anharmonic terms contribute to the phonon energy, causing a renormalization of the phonon frequencies $\omega_s(\mathbf{q})$. This frequency shift must be taken into account, for example, in the determination of phonon frequencies by resonance experiments (neutron scattering, Raman scattering, etc.). The finite lifetime results in a broadening of the lines of the scattering spectrum.

The anharmonic terms play an important role in the thermodynamics of crystals. They give rise to the phenomenon of thermal expansion, the difference between adiabatic and isothermal processes, between specific heat at constant volume and at constant pressure, and they influence the thermal conductivity and the temperature dependence of phonon frequencies. Furthermore, the anharmonic terms determine the thermal equilibrium of phonons and the lattice heat conduction.

The transport properties of a crystal are given both by the electron and the phonon system. The mean number of phonons of type $(\mathbf{q}, s)$ present in thermal equilibrium at temperature T is given as

$$n_s(\mathbf{q}) = \frac{1}{\mathrm{e}^{\hbar\omega_s(\mathbf{q})/k_\mathrm{B}T} - 1} \tag{5.1}$$

which represents a Bose-Einstein distribution function [22].

5.1.1 Thermal expansion

In the harmonic approximation, the equilibrium positions of the lattice ions are determined by minimizing the potential energy and are regarded as temperature independent. Unfortunately, this is reasonable for most solids only for temperatures well below the melting point: At very low temperatures, the ions move close to their equilibrium positions because of the small thermal energies and the harmonic approximation succeeds in describing the atom motions. At higher temperatures, the thermal energy is sufficient to permit the ions to move farther from their equilibrium positions and the anharmonic terms become relevant.

[1] $\mathbf{q}$ is the wave vector and s the branch index.

The harmonic approximation neglects thermal expansion and leads to identical adiabatic and isothermal elastic constants, and to a temperature independent specific heat above the Debye temperature.[2] This is not valid anymore when we take into account the lattice anharmonicity. Thermal and caloric quantities show different behavior. The importance of anharmonic terms is reflected in the high-temperature behavior of the specific heat. In this temperature regime, the harmonic approximation states that the specific heat due to lattice vibrations should obey the classical law of Dulong and Petit, which predicts a contribution to the specific heat of $3k_{\mathrm{B}}$ per ion. The failure of the high-temperature specific heat to approach this value is an anharmonic effect. Furthermore, the frequency shift in the normal modes is due to the thermal expansion. In real crystals the force constants Φ in the harmonic approximation are defined for the equilibrium ion positions about which the harmonic expansion is made. However, since in real crystals the harmonic approximation is not exact, a change in the equilibrium lattice vectors due to anharmonic terms changes also the normal mode frequencies.

5.1.2 Thermal conductivity

In a system of non-interacting phonons, locally delivered thermal energy is distributed through the crystal by phonons with the velocity of elastic waves. In a perfectly harmonic crystal the phonon states are stationary states, that remain unaltered in the course of the time and a thermal current carried by phonons will persist forever. Therefore, a perfectly harmonic crystal would have an infinite thermal conductivity. In the case of non-interacting phonons or phonons that interact through *normal* processes[3] the total crystal momentum is conserved. Phonons carry energy even if the temperature gradient is zero and, thus, the crystal has no thermal resistivity. Non-zero thermal resistivity means that in the interaction process between phonons the conservation law of total momentum is violated and so-called *umklapp* processes[4] take place. These processes are strongly temperature dependent.

At low temperatures the only scattering process that can occur at an appreciable rate are those that conserve the total crystal momentum, thus the normal processes. *Umklapp* processes are "frozen out" because they take place only between phonons with

[2]The Debye temperature $\Theta_{\mathrm{D}} = \hbar\omega_{\mathrm{D}}/k_{\mathrm{B}}$ is a measure of the temperature above which all modes begin to be excited and below which modes begin to be "frozen out". The Debye frequency ω_{D}, or cutoff frequency, is a measure of the maximum phonon frequency.

[3]A *normal* process is a phonon collision in which the total initial and final crystal momenta are equal. Energy and wave vector are conserved.

[4]In an *umklapp* process the total crystal momenta before and after the collision differ by a non-zero reciprocal lattice vector.

energy $\hbar\omega_s$ that is not small compared with $\hbar\omega_\mathrm{D}$, where ω_D is the Debye frequency. At low temperature the mean number of such phonons is

$$n_s(\mathbf{q}) = \frac{1}{\mathrm{e}^{\hbar\omega_s(\mathbf{q})/k_\mathrm{B}T} - 1} \approx \frac{1}{\mathrm{e}^{\hbar\omega_\mathrm{D}/k_\mathrm{B}T} - 1} \approx \mathrm{e}^{-\hbar\omega_\mathrm{D}/k_\mathrm{B}T}. \tag{5.2}$$

As the temperature drops, the number of phonons that can participate in *umklapp* processes drops exponentially, the conductivity increases exponentially and the anharmonic terms become negligible. Without the *umklapp* processes the thermal conductivity would be infinite. As the conductivity increases exponentially with decreasing temperature, the phonon mean free path becomes soon comparable to the mean free path due to scattering of phonons by lattice imperfections or even to the mean free path describing the scattering of phonons by the sides of the finite crystal. Therefore, at very low temperatures the conductivity is limited by temperature-independent scattering processes determined by the geometry and purity of the sample and the temperature dependence of the conductivity becomes that of the specific heat.

The analysis of the full temperature range leads to the following result: In the low-temperature region the conductance is limited by surface scattering and rises with temperature as the phonon specific heat. As the temperature rises, *umklapp* processes become frequent enough to yield a mean free path shorter than the temperature-independent one. At this point the thermal conductivity reaches a maximum, beyond which it declines rapidly reflecting the exponential increase in the number of umklapp processes with rising temperature. The exponential decline is quickly replaced by a slower power law, because scattering processes are enhanced by an increasing number of phonons. Indeed, at high temperatures the total number of phonons in the crystal is proportional to T because the thermal phonon occupation number of Eq. (5.1) is $n_s(\mathbf{q}) \approx k_\mathrm{B}T/\hbar\omega_s(\mathbf{q})$. For further specifications we refer to the book of Ashcroft and Mermin [22] or Madelung [24]. Reference [69] presents the calculated thermal conductivity of a carbon nanotube.

In conclusion, if we keep into account anharmonicity, we expect the normal modes to interact among each other and to have a finite lifetime. Scattering processes lead to a frequency shift and to a damping of phonons. Anharmonic effects have remarkable influences mostly at high temperatures while the low-temperature range is well described by the harmonic approximation.

5.2 Specific heat

According to statistical thermodynamics, the vibrational partition function of phonons can be written as

$$Z = \prod_{\mathbf{q},s} \frac{\mathrm{e}^{-\hbar\omega_s(\mathbf{q})/2k_\mathrm{B}T}}{1-\mathrm{e}^{-\hbar\omega_s(\mathbf{q})/k_\mathrm{B}T}}, \tag{5.3}$$

where k_B is the Boltzmann constant, T is the temperature, and $s = 1, \ldots, 3r$. The internal energy is then

$$E = k_\mathrm{B}T^2 \left(\frac{\partial \ln Z}{\partial T}\right) = \sum_{\mathbf{q},s} \frac{\hbar\omega_s(\mathbf{q})}{2} \frac{\mathrm{e}^{\hbar\omega_s(\mathbf{q})/k_\mathrm{B}T}+1}{\mathrm{e}^{\hbar\omega_s(\mathbf{q})/k_\mathrm{B}T}-1} \tag{5.4}$$

$$= \sum_{\mathbf{q},s} \frac{\hbar\omega_s(\mathbf{q})}{2} \coth\left(\frac{\hbar\omega_s(\mathbf{q})}{2k_\mathrm{B}T}\right) \tag{5.5}$$

The specific heat is the change of total energy with temperature:

$$c_\mathrm{V} = \frac{1}{V}\left(\frac{\partial E}{\partial T}\right)_V = \frac{k_\mathrm{B}}{V} \sum_{\mathbf{q},s} \left(\frac{\hbar\omega_s(\mathbf{q})}{2k_\mathrm{B}T}\right)^2 \frac{1}{\sinh^2(\hbar\omega_s(\mathbf{q})/2k_\mathrm{B}T)}. \tag{5.6}$$

We do not distinguish between specific heat at constant volume or constant pressure, since the harmonic approximation does not include thermal expansion of the lattice. The specific heat depends in a detailed way on the frequency spectrum of the normal modes. The frequency spectrum $g(\omega)$, or density of states (DOS), is defined such that $g(\omega)\mathrm{d}\omega$ is the fraction of eigenfrequencies in the interval $(\omega, \omega + \mathrm{d}\omega)$:

$$g(\omega) = \frac{1}{3rN} \sum_s \int \frac{V}{(2\pi)^3} \frac{\mathrm{d}S}{|\nabla\omega_s(\mathbf{q})|} \tag{5.7}$$

where the integration is done over a surface S of constant frequency in the first Brillouin zone. There will be a structure of singularities in $g(\omega)$, reflecting the fact that the group velocity $\nabla\omega_s(\mathbf{q})$ vanishes at some frequencies. The singularities are known as van Hove singularities.

Within the harmonic approximation the thermodynamic functions are additive functions of the eigenfrequencies $\omega_s(\mathbf{q})$. However, since the crystal volume V is very large and the $\mathbf{q}$ values are densely spaced, the sum over $\mathbf{q}$ can be replaced by an integral [70]:

$$\sum_{\mathbf{q},s} \to \sum_s \int \mathrm{d}\mathbf{q} \equiv \sum_s \frac{V}{(2\pi)^3} \int \mathrm{d}^3q \tag{5.8}$$

$$= \sum_s \frac{V}{(2\pi)^3} \int \mathrm{d}S \frac{\mathrm{d}\omega_s}{|\nabla\omega_s|} \tag{5.9}$$

$$= 3rN \int_0^\infty g(\omega)\mathrm{d}\omega. \tag{5.10}$$

Dimension	Phonon dispersion	Phonon DOS	Specific heat
1D	$\omega \propto q^2$	$g(\omega) \propto 1/\sqrt{\omega}$	$c_\mathrm{V} \propto \sqrt{T}$
	$\omega \propto q$	$g(\omega) = \mathrm{const}$	$c_\mathrm{V} \propto T$
2D	$\omega \propto q^2$	$g(\omega) = \mathrm{const}$	$c_\mathrm{V} \propto T$
	$\omega \propto q$	$g(\omega) \propto \omega$	$c_\mathrm{V} \propto T^2$
3D	$\omega \propto q$	$g(\omega) \propto \omega^2$	$c_\mathrm{V} \propto T^3$

Table 5.1: Low-temperature behavior of the specific heat. The dimensionality of the system has great influence on the density of states and, therefore, on the specific heat. At low temperature only acoustic modes are excited. These can have either linear or quadratic dispersion.

Thus, for the specific heat we obtain:

$$c_\mathrm{V} = 3rNk_\mathrm{B} \int_0^\infty \mathrm{d}\omega \left(\frac{\hbar\omega}{2k_\mathrm{B}T}\right)^2 \frac{g(\omega)}{\sinh^2(\hbar\omega/2k_\mathrm{B}T)}. \tag{5.11}$$

The high-temperature (or classical) limit of this expression does not depend on the particular structure of the carbon system and is equal to $3k_\mathrm{B}/m = 2078$ mJ/gK with m being the atomic mass of carbon. In the low temperature regime, modes with $\hbar\omega_s(\mathbf{q}) \gg k_\mathrm{B}T$ will negligibly contribute to Eq. (5.11), since the integrand will vanish exponentially. However, because $\omega_s(q) \to 0$ as $q \to 0$ in the four acoustic branches of a carbon nanotube, this condition is not satisfied by acoustic modes at long wavelengths, even at very low temperature. These modes alone determine the behavior of the specific heat at low temperatures. Furthermore, the low-temperature behavior of c_V contains information regarding the dimensionality of the system. Because nanotubes are quasi-one dimensional (1D) systems consisting of rolled-up 2D sheets, they are expected to exhibit both 1D and 2D behavior. Table 5.1 gives a general overview of the dependence of c_V on the dimensionality, on the density of states, and on the behavior of the acoustic branches. The specific heat of carbon nanotubes is mainly determined by phonons, electronic contributions to it can be neglected [68].

Figure 5.1 shows the calculated low-energy vibrational density of states of graphene and of two (10,10) carbon nanotubes with respectively linear and quadratic dispersion of the TA mode. The DOS of the nanotube with quadratic dispersion has a characteristic singularity of the type $1/\sqrt{\omega}$ at $\omega = 0$, due to the q^2 mode, while the nanotube with linear dispersion and graphene have finite DOS at this frequency, as predicted in Table 5.1. With increasing energy the DOS of the nanotubes increases stepwise with the entry of higher subbands. This happens because the periodic boundary condition on the circumferential wave vector splits each of the modes into 1D subbands that give rise to sharp spikes in the DOS: At each band edge there is a van Hove singularity. In contrast to the 1D DOS of the nanotubes, the calculated DOS of graphene varies

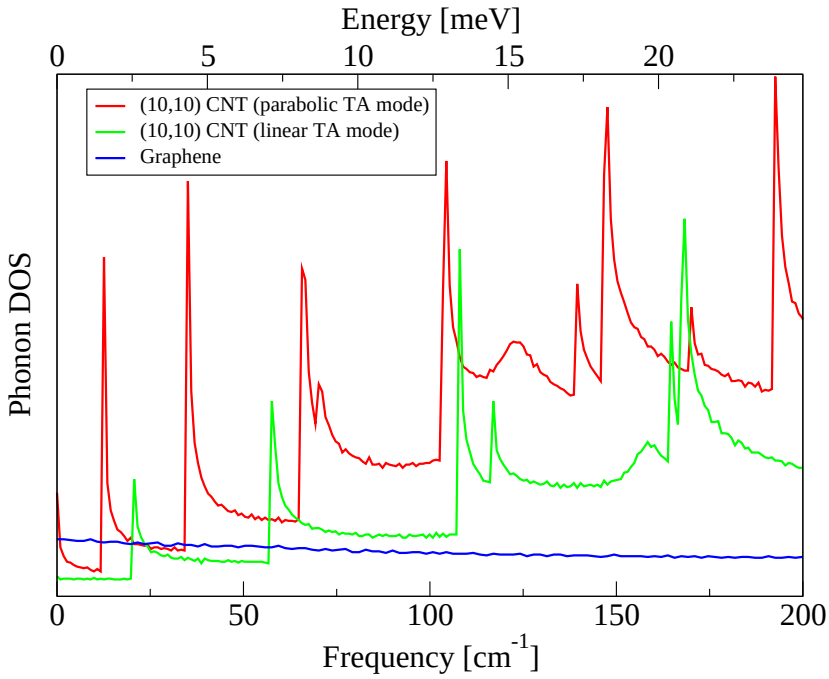

Figure 5.1: Phonon density of states for a (10,10) CNT in the Mahan-Jeon (MJ) model (red line), a (10,10) CNT in the fourth-nearest-neighbor (4NNFC) model with only linear acoustic modes (green line) and graphene in the 4NNFC model (blue line). The two latter lines show finite DOS at $\omega = 0$, while the first shows a singularity that is due to the acoustic mode with q^2 dependence. This prompts again that the 4NNFC model with the parametrization of Saito *et al.* does not yield the flexural character of the TA mode. This results in a wrong specific heat at low temperatures, because the behavior of c_V depends sensitively on the DOS. Beside this, the DOS of the nanotubes increases stepwise with the entry of higher subbands, demonstrating the 1D behavior at low temperatures. Instead, the q^2 mode of graphene gives rise to a nearly constant DOS for graphene. The curves are not scaled, therefore the comparison is only qualitative.

smoothly. The quadratic dispersion yields a constant DOS in 2D, which dominates the contribution of the other two (linear dispersing) acoustic modes. Thus, in a nanotube the phonons are 1D at the lowest temperatures: Only the four acoustic subbands are occupied. At a temperature $T_{\mathrm{opt}} = \hbar\omega_{\mathrm{opt}}/6k_{\mathrm{B}}$, the first optical subband with frequency ω_{opt} at $q = 0$ begins to contribute to the specific heat. The optical phonons give negligible contribution to the specific heat for temperatures less than T_{opt}, for which the factor multiplying $g(\omega)$ in the integral (5.11) becomes smaller than 0.1 [71]. For example for $\omega_{\mathrm{opt}} \approx 20$ cm^{-1} this happens at $T_{\mathrm{opt}} = 4.8$ K. Well above T_{opt}, many subbands are occupied and the tube is essentially 2D.

The specific heat calculated from the theoretical DOS spectra is shown in Fig. 5.2 as

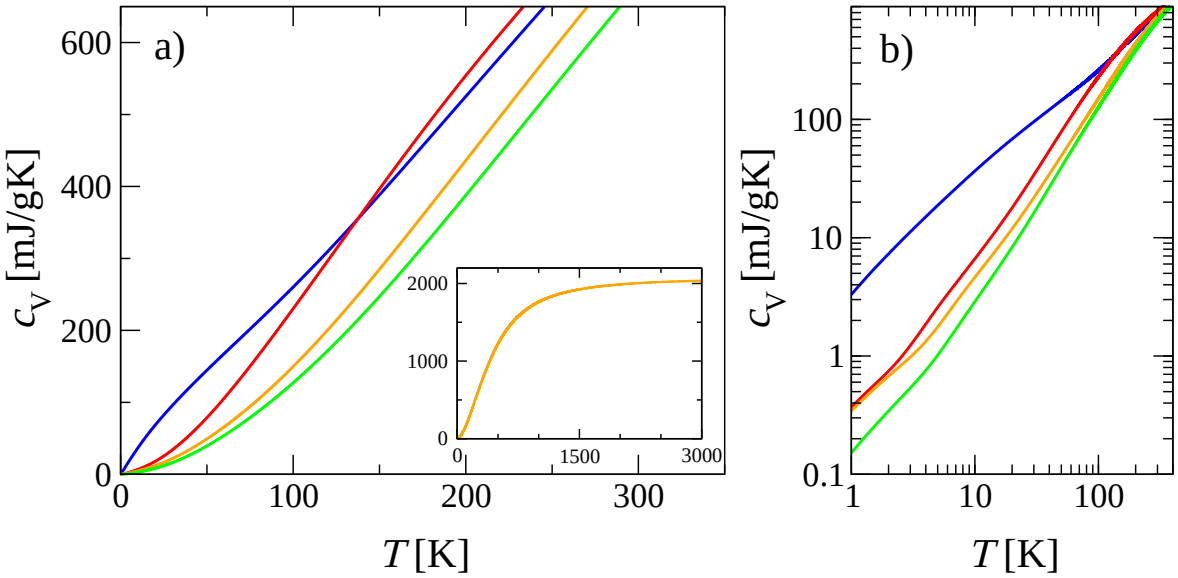

Figure 5.2: Panel (a): specific heat as a function of temperature for graphene (blue line), calculated with the 4NNFC model and our new parameters of Table 3.2, and for a (10,10) CNT calculated with the MJ model (red line), the 4NNFC model with our parameters (orange line), and the 4NNFC model with the original constants of Saito *et al.* (green line). The inset shows a wider temperature interval to demonstrate that c_V approaches the value 2078 mJ/gK for high temperatures. Panel (b): specific heat on a logarithmic scale for the low frequency region. The assignment of the colors is the same as in panel (a).

a function of temperature. The dimensionality of the system reflects in the behavior of c_V: In graphene the low-temperature specific heat is dominated by the quadratic layer-bending mode and therefore has a roughly linear T dependence. We could also confirm that the (10,10) CNT with linear dispersing acoustic modes (green line in Fig. 5.2) shows $c_V \propto T$ at low T, with an increase in slope due to the contribution from the first subband above ≈4 K. This behavior is in accordance with the prediction of Table 5.1 and is a direct confirmation of a 1D quantized phonon spectrum in carbon nanotubes. For the nanotubes with a quadratic dispersion of the TA modes (red and orange lines in Fig. 5.2), the task of recognizing the correct T dependence of c_V becomes more involved. For temperatures below T_{opt} we can not define a clear T dependence, since two linear and two quadratic modes contribute to c_V, superposing on each other. We find that between 1 K and T_{opt} the dependence is linear in T, which suggests that the linear modes are already dominating. Above T_{opt} the slope increases due to the optical phonons. In the calculation with the Mahan-Jeon (MJ) model (red line in Fig. 5.2) this happens earlier than in the 4NNFC model with our parametrization (orange line). This is due to the fact that the first gives a lower frequency for ω_{opt}, which is 12.6

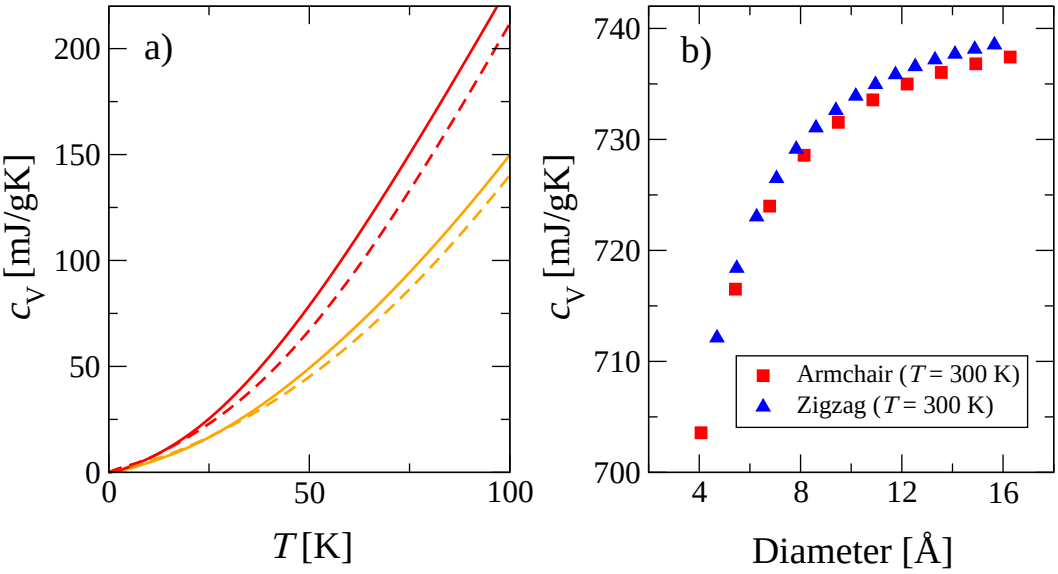

Figure 5.3: Chirality dependence of the specific heat. Panel (a): temperature dependence of c_V for a (10,10) CNT (straight lines) and a (10,0) CNT (dashed lines). The assignment of the colors is the same as in Fig. 5.2. Panel (b): the effect of tube diameter on zigzag and armchair CNT specific heat. At a given temperature the specific heat increases with the increase of tube diameter. The upper limit is given by graphene, with $c_V = 794$ mJ/gK at 300 K.

cm^{-1}, while the other one gives 20.2 cm^{-1}. At high temperatures, all the specific heats are identical and converge to the high temperature limit of 2078 mJ/gK. At low temperatures, the nanotube curve lies well below the graphene one because the tube has no low-energy counterpart to the layer bending modes [7]. Our results for c_V agree very well with previous calculations and experiments [7,71-73].

Similar results can be obtained from other armchair and zigzag nanotubes. But since the first optical subband edge varies from tube to tube, the turning points are different, resulting in crossover of c_V curves. The general uptrend and the high-temperature limit are the same. Figure 5.3 (panel (a)) shows the specific heat curves for a (10,10) and a (10,0) CNT. The tube diameter influences the specific heat of carbon nanotubes, especially in the range of 25-350 K. In order to discern the effect of tube diameter on the specific heat, additional results for $T = 300$ K are displayed in Fig. 5.3 (panel (b)), using the 4NNFC model with our parametrization. At a given temperature the specific heat increases with the increase of tube diameter. This was as expected, since for very large diameters the curve should approach the c_V value of graphene, which is 794 mJ/gK at 300 K. However, the effect diminishes at large tube diameter. The chirality shows only a small effect in the tubes specific heat, with c_V of the zigzag tubes

lying over that of the armchair tubes. This small effect is negligible and could also be caused by inaccuracies of the model description. The results are in good agreement with those of Ref. [74, 75].

5.3 Landauer phonon transport

The physics of mesoscopic electron transport in one dimension has attracted a lot of attention in the last two decades. One striking result is the quantization of electrical conduction, observed in a quasi one dimensional constriction of two dimensional electron gas between reservoirs. The conductance of this system is determined by the number of participating quantum states or 'channels' within the constriction. Each spin-degenerate channel contributes a quantized unit of $2e^2/h$ to the electrical conductance, as has been understood within the framework of Landauer theory. In the case of an ideal long one-dimensional wire with no scattering, the conductance between the electrodes is [76]:

$$G = N_{\mathrm{C}} \frac{2e^2}{h} \tag{5.12}$$

with N_{C} the number of channels available for transport. This leads to a quantized conductance.

One dimensional ballistic phonon transport should also be possible. Phonon heat transport in mesoscopic systems can be investigated using methods analogous to the Landauer description of electrical conductance. The thermal conductance of phonon waveguides in the ballistic, one-dimensional limit has recently been calculated using the Landauer formula [77, 78].

5.3.1 Phonon currents

We consider a model of an ideal one-dimensional heat conductor as illustrated in Fig. 5.4. Two long perfect leads join a central segment in which the phonon scattering occurs. We consider only elastic scattering and neglect phonon-phonon interaction.

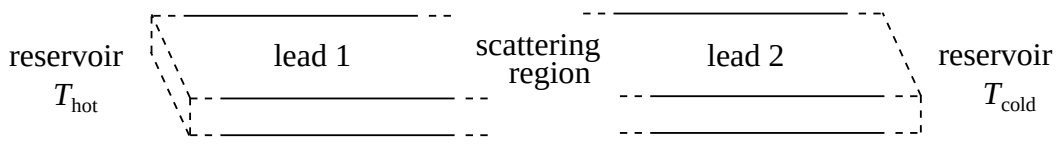

Figure 5.4: Schematic diagram of the model wire. The left and right reservoirs are at temperatures T_{hot} and T_{cold}, respectively.

The other ends of the two leads are connected to reservoirs of temperature $T_{\rm hot}$ and $T_{\rm cold}$ where the phonon distributions are Bose-Einstein distributions $\eta_i(\omega) = 1/(\mathrm{e}^{\hbar\omega/k_{\rm B}T_i} - 1)$ with $i =$ hot/cold. No scattering occurs at the reservoir-lead connections. The calculation of the heat transport proceeds as in the calculation of the ideal electrical conductance (Eq. (5.12)) except that we are interested in energy transport, rather than number transport, and that the thermal distribution is given by the Bose distribution $\eta(\omega)$ rather than by the Fermi distribution. Considering first the transport by the right moving phonons, the energy flux is [77]:

$$J^+ = \frac{1}{2\pi} \sum_s \int_0^\infty \mathrm{d}q\, \hbar\omega_s(q)\, \eta_{\rm hot}(\omega_s(q))\, v_s(q)\, \mathcal{T}_s(q) \tag{5.13}$$

where $\omega_s(q)$ is the dispersion relation of the discrete mode s, $v_s(q)$ is the group velocity and $\mathcal{T}_s(q)$ are transmission coefficients characterizing the coupling of waveguide modes to the reservoirs. Transforming the integral to an integral over frequencies yields an expression for the heat transport by right moving phonons that can be written as a sum of mode contributions $J^+ = \sum_s J_s^+$ with:

$$J_s^+ = \frac{1}{2\pi} \int_{\omega_s^{\rm min}}^{\omega_s^{\rm max}} \mathrm{d}\omega\, \hbar\omega\, \eta_{\rm hot}(\omega)\, \mathcal{T}_s(\omega), \tag{5.14}$$

where $\omega_s^{\rm min}$ and $\omega_s^{\rm max}$ are the cutoff frequencies of the sth mode, that define the frequency interval in which the mode propagates. The group velocity $v_s = \partial\omega_s/\partial q$ was canceled by the 1D density of states $g(\omega_s) = \partial q/\partial\omega_s$. The heat transport is given by summing J_s^+ over the modes s and subtracting the analogous expression for $\sum_s J_s^-$ for the left moving phonons. The reservoir-to-reservoir heat current or Landauer energy flux, takes the form:

$$J_{\rm ph} = \sum_s \int_{\omega_s^{\rm min}}^{\omega_s^{\rm max}} \frac{\mathrm{d}\omega}{2\pi}\, \hbar\omega\, [\eta_{\rm hot} - \eta_{\rm cold}]\, \mathcal{T}_s(\omega) \tag{5.15}$$

This expression is similar to the Landauer result for electrical current:

$$J_{\rm el} = \int \mathcal{T}(E)[f_{\rm hot} - f_{\rm cold}]\, \mathrm{d}E \tag{5.16}$$

in a junction connecting two electron reservoirs characterized by Fermi distributions f_i and a transmission function $\mathcal{T}(E)$.

Assuming perfectly adiabatic contact between the thermal reservoirs and the ballistic quantum wire, the transmission function for the mode s is a step function:

$$\mathcal{T}_s(\omega) = \begin{cases} 1 & \text{for } \omega_s^{\rm min} \le \omega \le \omega_s^{\rm max}, \\ 0 & \text{otherwise.} \end{cases} \tag{5.17}$$

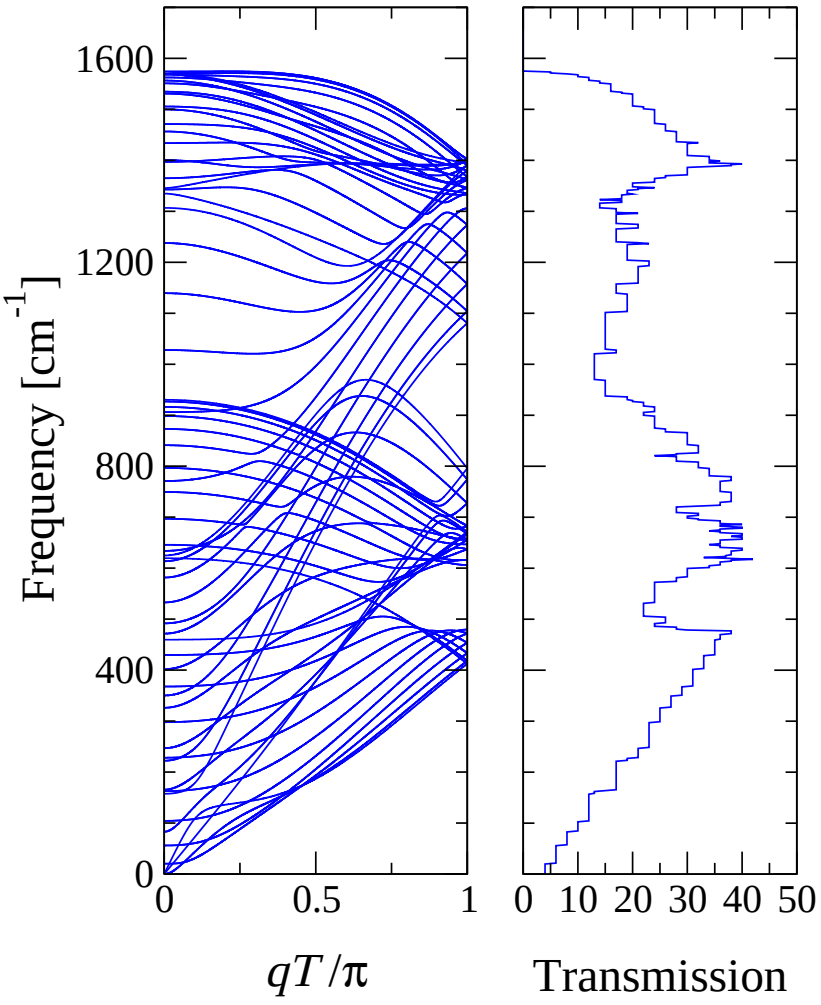

Figure 5.5: Phonon dispersion of a (10,10) CNT and the transmission function $\mathcal{T} = \sum_s \mathcal{T}_s(\omega)$. The latter is a sum of $s = 120$ step functions.

The total transmission function is given by:

$$\mathcal{T} = \sum_s \mathcal{T}_s(\omega). \tag{5.18}$$

For a (10,10) CNT it is illustrated in Fig. 5.5 (for the evaluation of the total transmission function see App. A) Considering only the total transmission, it is possible to eliminate the sum over s in Eq. (5.15), obtaining for the heat current:

$$J_{\rm ph} = \int_0^\infty \frac{\mathrm{d}\omega}{2\pi}\, \hbar\omega \left[\eta_{\rm hot} - \eta_{\rm cold}\right] \mathcal{T}(\omega) \tag{5.19}$$

5.3.2 Thermal conductance

In this Section, we investigate the low-temperature thermal conductance of carbon nanotubes placed between hot and cold heat baths and the possibility of ballistic phonon transport within the nanotube. The reservoirs are represented as systems of independent harmonic oscillators at thermal equilibrium. We consider a nanotube coupled linearly to these thermal environments and neglect anharmonic effects. The thermal conductance is defined as:

$$\kappa_{\rm ph} = \frac{J_{\rm ph}}{\Delta T} \tag{5.20}$$

with $\Delta T = T_{\rm hot} - T_{\rm cold}$. In the limit of linear response, $\Delta T \ll T \equiv (T_{\rm hot} + T_{\rm cold})/2$, we obtain using Eq. (5.19) and the substitution $x = \hbar\omega/k_{\rm B}T$:

$$\kappa_{\rm ph} = \frac{k_{\rm B}^2 T}{h} \int_0^\infty {\rm d}x \, \frac{x^2 {\rm e}^x}{({\rm e}^x - 1)^2} \, \mathcal{T}\left(x \frac{k_{\rm B}T}{\hbar}\right). \tag{5.21}$$

This equation plays the role of a 'universal' phonon conductance in direct analogy with the expression (5.12) for the electronic case. An important statement is that the result is independent of all details of the dispersion curve except the transmission function. This arises because the density of states in the frequency integral is cancelled by the group velocity. (For the evaluation of the integral in Eq. (5.21) see App. B).

In the following, we demonstrate that at low temperatures a carbon nanotube behaves as a ballistic, one-dimensional wire and the phonon thermal conductance is quantized. The integral in Eq. (5.21) is given by the product of two functions: the transmission function and a weight function $x^2{\rm e}^x/({\rm e}^x - 1)^2$. The former is related to the phonon spectral properties of the nanotube and the latter takes into account the effects due to temperature. For high temperatures, the two functions are non-zero within the same range, this means that all the transmission modes contribute to the thermal conductance. Whereas, in the limit of low temperature, the broadness of the weight function is extended only to the low energy modes. Fig. 5.6 illustrates schematically the relative behavior of these two functions. Therefore, at low temperatures only the four lowest lying acoustic modes of a nanotube give an appreciable contribution to the thermal conductance. In this temperature regime Eq. (5.21) becomes greatly simplified:

$$\kappa_{\rm ph} \simeq \frac{k_{\rm B}^2 T}{h} \, 4 \int_0^\infty {\rm d}x \, \frac{x^2 {\rm e}^x}{({\rm e}^x - 1)^2} = 4 \, \frac{\pi^2 k_{\rm B}^2 T}{3h}. \tag{5.22}$$

Here, 4 represents the number of acoustic branches. The upper limit of the integral is of few importance, because the integrand function falls off rapidly, before the successive

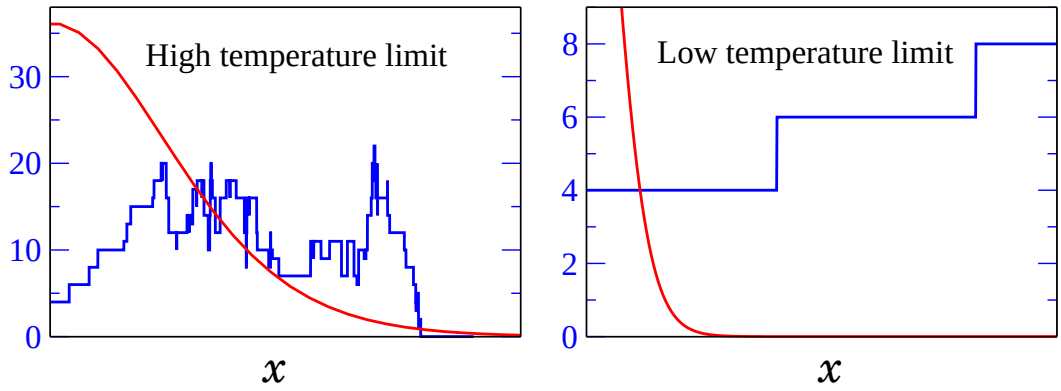

Figure 5.6: Sketch of the two functions that are multiplied in the integral in Eq. (5.21): the transmission function (here, that of a carbon nanotube, blue line) and the temperature-dependent weight function $x^2 e^x/(e^x-1)^2$ (red line). For low temperatures, the weight function falls off to zero before the first step in the transmission function takes place. This step is from 4 to 6 (as indicated on the axis) for a nanotube and is due to the excitation of the lowest optical modes. For this reason, at low temperatures only the 4 acoustic modes contribute to the thermal conductance.

step in the transmission function takes place (see Fig. 5.6). A fundamental relation holds for each mode:

$$\kappa_0 = \frac{\pi^2 k_B^2 T}{3h}, \tag{5.23}$$

an expression independent of any material parameters. This quantum of thermal conductance represents the *maximum possible value of energy transported per phonon mode*. It does not depend on particle statistics, therefore, is universal for fermions, bosons, and anyons [79]. Figure 5.7 shows the temperature dependent thermal conductance of a (10,10) CNT, normalized to the value of $4\kappa_0$. The calculated values approach unity in the low temperature limit, demonstrating that the phonon thermal conductance of carbon nanotubes is quantized. Steps are not observed, however, because of the broadening of the Bose-Einstein distribution compared with the subband edge separation. Furthermore, the thermal conductance depends only on the tube radius and not on chirality. Results for armchair tubes are very similar to the ones for zigzag tubes, when the same diameters are compared. This arises because the energy of the lowest lying optical modes, $\hbar\omega_o$, is determined only by the tube radius and decreases approximately according to $\sim 1/R^2$ [11]. Figure 5.7 (panel (b)) shows the thermal conductance for several nanotubes.

It is interesting to consider the effect of the behavior of the acoustic branches on the thermal conductance, whether it is relevant or not if the TW acoustic mode has linear

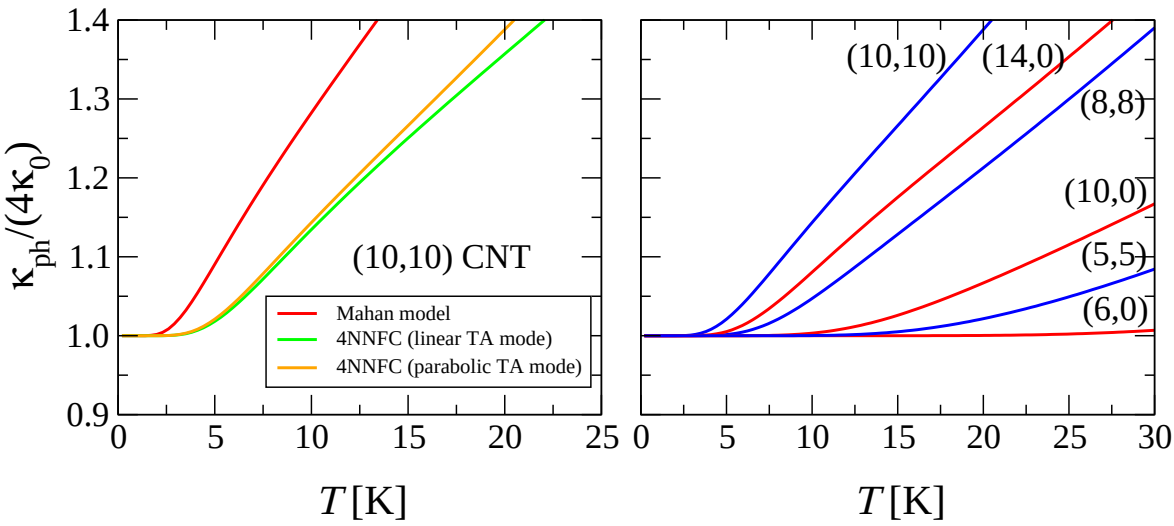

Figure 5.7: Panel (a): Phonon thermal conductance for a (10,10) CNT calculated with the MJ model (red line), the 4NNFC model with our parameters (orange line), and the 4NNFC model with the original constants of Saito *et al.* (green line). The two latter show, respectively, quadratic and linear dispersion for the TA mode, however this difference does not influence the qualitative behavior of the two curves. The deviations above 10 K are due to small differences in the optical frequencies. Panel (b): Thermal conductance for several carbon nanotubes, calculated with our parametrization. The length of the plateau depends on the lowest optical frequency.

or quadratic dependence on q. It is clear that, to construct the transmission function, it does not matter whether the dispersions are linear or quadratic, but only that the branch's upper and lower limits should be accurately computed. We performed the calculations for both cases and obtained very similar results, as illustrated in Fig. 5.7 (panel (a)). The results of the 4NNFC model are believed to be more accurate than the ones obtained using Mahan and Jeon's method for the dispersions, because the latter does not correctly reproduce the graphene phonon dispersion.

Our results are in good agreement with those of Yamamoto *et al.* [11] and Mingo *et al.* [80]. Experimental studies were achieved by Schwab *et al.* [8], who observed the quantum thermal conductance in a nanofabricated 1D structure, which behaves essentially like a phonon waveguide. Brown *et al.* [81] measured simultaneously ballistic thermal and electrical conductance of individual multiwall carbon nanotubes.

Expression (5.21) represents an idealized case in which the transmission of phonons from one reservoir to the other happens without reflections. A more realistic model has to incorporate the effects of the reflections caused by the contacts between the reservoirs and the 1D wire. Furthermore, whenever the system size is larger than the mean free

path, which depends on temperature, scattering of phonons due to anharmonicity of the interatomic potential begins to decrease the conductance and the transport is no longer ballistic.

Conclusions and perspectives

The vibrational properties of carbon nanotubes play a fundamental role in the physics and the characterization of modern materials. Apart from being of fundamental interest for both experimental and theoretical research, vibrations are of central importance for the application of nanotubes in electronic devices.

According to Moore's Law, the microelectronic devices have been continuously scaled down. The limits to the further miniaturization of microelectronics have led to intense research directed toward the development of nanoelectronics. However, the decrease in feature size and the increase in power consumption give rise to a fundamental problem: How can we cope with the enormous heat generation? Modelling heat transfer of carbon nanotubes is a serious issue for understanding the thermal properties of nanotube-based composites and nanoelectronic devices. Key point is that in carbon nanotubes the thermal properties are dominated at all temperatures by phonons rather than by electrons. Most heat is carried by phonons of large wave vector and they have mean free paths at room temperature between 1 and 100 nm. Therefore, in many systems of current interest, the scale of the microstructure is the same scale as the mean free path of the phonons and, sometimes, comparable to the phonon wavelength. In order to have a satisfactory description of this effect one needs an accurate understanding of the fundamental phonon processes, in particular scattering by electrons and by zone boundaries.

In this work, we developed a picture of the vibrational properties of armchair and zigzag carbon nanotubes. The calculations of the phonons were accomplished by comparing and modifying two different force-constant models: A valence force-field model with three free parameters [28] and one consisting in the direct parameterization of the real-space force constants, with twelve parameters [13]. While the former is optimized for the calculation of phonon dispersions of carbon nanotubes, the latter was introduced for graphene and then adapted to nanotube geometry. In the first case we used

parameters present in literature whereas in the second one we achieved a new parameterization of the force constants of graphene. Indeed, in the original parameterization the force constants were empirically determined by fitting to measured elastic constants and phonon frequencies. We applied a method called 'force matching', consisting of an optimization procedure which tries to match as closely as possible *ab initio*-derived forces. This method is valid since *ab initio* data can complement the experimental quantities normally used to fit potentials. In the specific, by fitting the twelve free parameters and considering atomic interactions up to fourth nearest neighbors, for almost the whole spectrum of the graphene we obtained an excellent agreement with the *ab initio* data [50]. With the same force constant model adapted to the geometry of carbon nanotubes and with our new parameterization, the low-frequency region of the phonon spectrum of carbon nanotubes shows remarkable changes. We found a qualitative difference with the results of the previous parameterization in a quadratic, rather than linear, dispersion of the transverse acoustic modes of nanotubes. There is disagreement in literature about the character of these so-called flexural modes. It is known from classical elasticity theory that in a solid wire there are flexural modes, but it is not obvious that nanotubes should have flexural modes, too. Only a detailed study of symmetry rules shows that the correct behavior must be quadratic. Furthermore, we put some corrections to the parameterizations for the special cases of the (10,10) and (10,0) CNT, in order to remove the problem of non-zero frequency of the twisting mode at zero wave vector.

For a better understanding, we visualized selected vibrational modes and compared the results obtained using the above mentioned two different force-constant models. With the three-parameter model we found atomic movements similar to those published in the literature, whereas with the twelve-parameter model the character of the vibrations was not clear due to considerable mode mixing. We suggest that a higher number of parameters should provide a more reliable result.

Eventually, we studied some thermal properties of carbon nanotubes through the calculation of the specific heat and the thermal conductance of nanotubes of different diameter and chirality. Comparing calculations for graphene and carbon nanotubes we demonstrated that the specific heat directly reflects the dimensionality of the system. Because nanotubes are quasi one-dimensional systems consisting of rolled-up 2D sheets, they exhibit both 1D and 2D behavior. Concerning heat transport, we showed that nanotubes can readily conduct heat by ballistic phonon propagation and that at low temperatures the thermal conductance for a single phonon channel approaches a maximum value of $\kappa_0 = \pi^2 k_B^2 T/(3h)$, the universal quantum of thermal conductance.

Despite the extensive work done so far, there are still a lot of interesting issues to be resolved. First of all the fourth-nearest-neighbor (4NNFC) model with twelve parameters should be improved paying particular attention to the behavior of the twisting mode. For this purpose one needs a direct implementation of the rotational sum rule. Afterwards, the model has to be generalized in order to describe tubes of various chiralities. Eventually, the question of how the atoms do effectively move should be clarified taking into consideration *ab initio* eigenvectors. Through a comparison between the latter and the eigenvectors obtained from the 4NNFC model it is possible to proof the reliability of the model approach. For this purpose it is important to include and study the influence of the non-diagonal terms in the force-constant tensors.

Regarding the specific heat and the thermal conductance, we recommend a systematic study with a qualitative analysis of the dependence on temperature, especially in the low-temperature regime. The influence of chirality on the behaviour of c_V and κ/κ_0 has to be studied in detail and a classification has to be performed.

Wider tasks are the vibrational properties of double- and multi-wall carbon nanotubes. Each layer can be viewed as obtained by rolling up an infinite strip of a graphite sheet into a seamless cylinder. The interlayer carbon-carbon interactions can be described by force constants of the valence force-field type obtained by fitting of the phonon dispersion of graphite. The interlayer interactions can be modeled by a potential of the Lennard-Jones type [82].

There are also very interesting topics that are closely related to experiments. The interplay between discrete vibrational and electronic degrees of freedom in molecular electronic devices represents an ascending research field. There are already both theoretical [83-85] and experimental [63] works showing that current directly injected into a suspended single-wall carbon nanotube can be used to excite, detect, and control a specific vibrational mode of the molecule. More theoretical work is needed to understand the current dependence of phonon-assisted tunnelling.

Another very important possible application of nanotubes where vibrations play a fundamental role is the fabrication of mass sensors based on a resonating CNT cantilever. The working principle is that the resonant frequency of the cantilever is dependent on the mass of the device, thus, by monitoring the resonant frequency change of the cantilever, any mass changes of the device can be detected. Such studies of nanoelectromechanical systems (NEMS) [86] promise to revolutionize measurements of extremely small displacements and extremely weak forces. NEMS can be built with mass sensitivities approaching a few attograms and with cross-sections of about 10 nm. The small effective mass of the vibrating part of the device gives NEMS a high sensitivity to additional masses, opening a wide range of sensing applications.

Appendix A

A topological approach to the transmission calculation

In this Appendix, we present a method to calculate the total transmission function, which is defined in Eq. (5.18). Basically, we need an algorithm that counts the number of phonon branches (accounting also for possible degenerations) populated at a fixed frequency $\overline{\omega}$. To clarify the procedure we explain the method on the prototypical example of a simple phonon dispersion, illustrated in Fig. A.1.

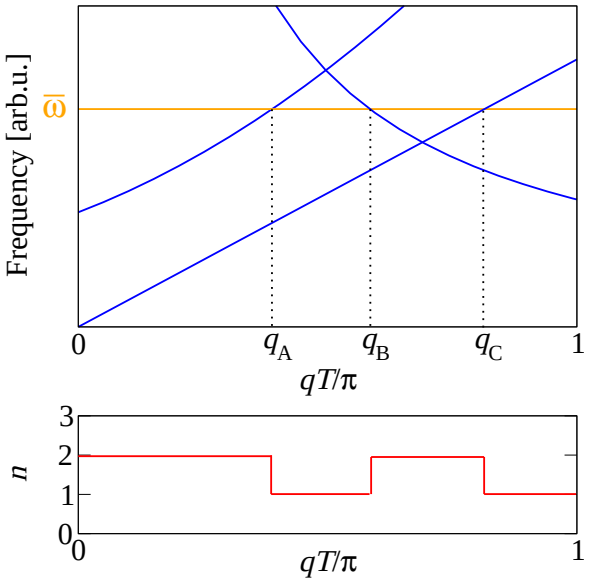

Figure A.1: A line of constant frequency (orange) crossing some branches of a phonon spectrum (blue lines). q_A, q_B and q_C denote the wave vectors of the crossing points. The lower panel represents the number n of branches that lie under the line $\omega = \overline{\omega}$, plotted against the wave vector. The number of steps in $n(q)$ are equal to the transmission: $\mathcal{T}(\overline{\omega}) = 3$.

The line representing a fixed frequency $\overline{\omega}$ crosses three branches of the dispersion, thus for $\omega = \overline{\omega}$ the transmission is $\mathcal{T}(\overline{\omega}) = 3$. The decisive point now is to formulate an appropriate algorithm that can do this for a fine grid of frequencies of an arbitrary phonon dispersion. The easiest way would be to fix a frequency and to count numer-

ically how often this frequency appears in the phonon dispersion, which means how many branches cross the line $\omega = \overline{\omega}$. This is easy to count by hand, but does not work when translated in a computer language. The problem is that in general we do not have the analytical expression for the dispersion curves, but only an amount of points. Our data are such that for every discrete q-vector between 0 and π/T, we have a set of the corresponding frequencies. With this method a computer would provide the phonon density of states instead of the wanted transmission function.

There is a method that works well even if the curves are made up only by single points. The idea is to choose a fine grid of q-vectors, and for each of them to run a loop over frequencies, counting how many branches for a fixed q appear with $\omega < \overline{\omega}$. Looking at the example of Fig. A.1, for q-vectors of the interval $0 < q < q_{\mathrm{A}}$ there are $n = 2$ branches lying below the line $\omega = \overline{\omega}$. At q_{A} there is a crossing, so that for $q_{\mathrm{A}} < q < q_{\mathrm{B}}$, only one branch lies under the line. For $q_{\mathrm{B}} < q < q_{\mathrm{C}}$ there are again two branches and for $q_{\mathrm{C}} < q < \pi/T$ there is one. This is plotted in the lower panel of Fig. A.1. The decisive point is to count the number of steps in the function n. In our example, we had three steps, respectively at q_{A}, q_{B} and q_{C}. The transmission function at the frequency $\overline{\omega}$ is equal to the number of steps: $\mathcal{T}(\overline{\omega}) = 3$. There can be also special cases where a step has $|\Delta n| = 2$. This has to be taken into account and has to be counted as 2. The transmission is thus given by:

$$\mathcal{T}(\overline{\omega}) = \sum_{r_{\overline{\omega}}=1}^{R_{\overline{\omega}}} |c_{r_{\overline{\omega}}}| \tag{A.1}$$

where $r_{\overline{\omega}} = 1, \ldots, R_{\overline{\omega}}$ are the steps and $c_{r_{\overline{\omega}}}$ is the amplitude of the $r_{\overline{\omega}}$th step. This has to be done for a fine grid of frequencies of the whole spectrum. The final result is the transmission function $\mathcal{T}(\omega)$.

Appendix B

Integral of the thermal conductance

In this Appendix, we provide the methods for solving the integral that appears in the expression for the thermal conductance. This was given by Eq. (5.21):

$$\kappa_{\mathrm{ph}} = k_{\mathrm{B}}\gamma \int_0^\infty \mathrm{d}x \, \frac{x^2 \mathrm{e}^x}{(\mathrm{e}^x - 1)^2} \, \mathcal{T}(x\gamma) \qquad \text{with} \quad \gamma = \frac{k_{\mathrm{B}} T}{\hbar} \tag{B.1}$$

where the transmission function $\mathcal{T}$ is a sum of step functions defined in Eq. (5.17). Dividing the whole frequency range from 0 to ω_{max} in N_{bin} small intervals (bins), we can split $\mathcal{T}$ in a set of constants functions $\mathcal{T}_n$ defined in these intervals:

$$\mathcal{T}(x\gamma) = \sum_{n=1}^{N_{\mathrm{bin}}} \mathcal{T}_n \, [\Theta(\gamma(x - x_n)) \cdot \Theta(\gamma(x_{n+1} - x))] \tag{B.2}$$

where Θ are step functions. Inserting Eq. (B.2) in Eq. (B.1) it is possible to put $\sum_n \mathcal{T}_n$ outside of the integral and eliminate the step functions changing the integration limits:

$$\kappa_{\mathrm{ph}} = k_{\mathrm{B}}\gamma \sum_{n=1}^{N_{\mathrm{bin}}} \mathcal{T}_n \int_0^\infty \mathrm{d}x \, \frac{x^2 \mathrm{e}^x}{(\mathrm{e}^x - 1)^2} \, \Theta(\gamma(x - x_n)) \cdot \Theta(\gamma(x_{n+1} - x)) \tag{B.3}$$

$$= k_{\mathrm{B}}\gamma \sum_{n=1}^{N_{\mathrm{bin}}} \mathcal{T}_n \underbrace{\int_{x_n}^{x_{n+1}} \mathrm{d}x \, \frac{x^2 \mathrm{e}^x}{(\mathrm{e}^x - 1)^2}}_{F(x_n, x_{n+1})} . \tag{B.4}$$

The analytical expression for $F(x_n, x_{n+1})$ is:

$$F(x_n, x_{n+1}) = \frac{x_n^2 \mathrm{e}^{x_n}}{\mathrm{e}^{x_n} - 1} - \frac{x_{n+1}^2 \mathrm{e}^{x_{n+1}}}{\mathrm{e}^{x_{n+1}} - 1} + 2 \ln \frac{(1 - \mathrm{e}^{x_{n+1}})^{x_{n+1}}}{(1 - \mathrm{e}^{x_n})^{x_n}} + 2 \left[\mathrm{Li}_2(\mathrm{e}^{x_{n+1}}) - \mathrm{Li}_2(\mathrm{e}^{x_n}) \right] . \tag{B.5}$$

In this expression appears the dilogarithm function[1] $\mathrm{Li}_2(s)$, which is a special case of the polylogarithm function $\mathrm{Li}_z(s)$ for $z = 2$ [87]. The polylogarithm function can be defined by the sum:

$$\mathrm{Li}_z(s) = \sum_{n=1}^{\infty} \frac{s^n}{n^z}. \tag{B.6}$$

The dilogarithm function is defined also by the integral:

$$\mathrm{Li}_2(s) = \int_s^0 \frac{\ln(1-t)}{t}\,\mathrm{d}t. \tag{B.7}$$

The real and imaginary part of $\mathrm{Li}_2(s)$ are plotted in Fig. B.1.

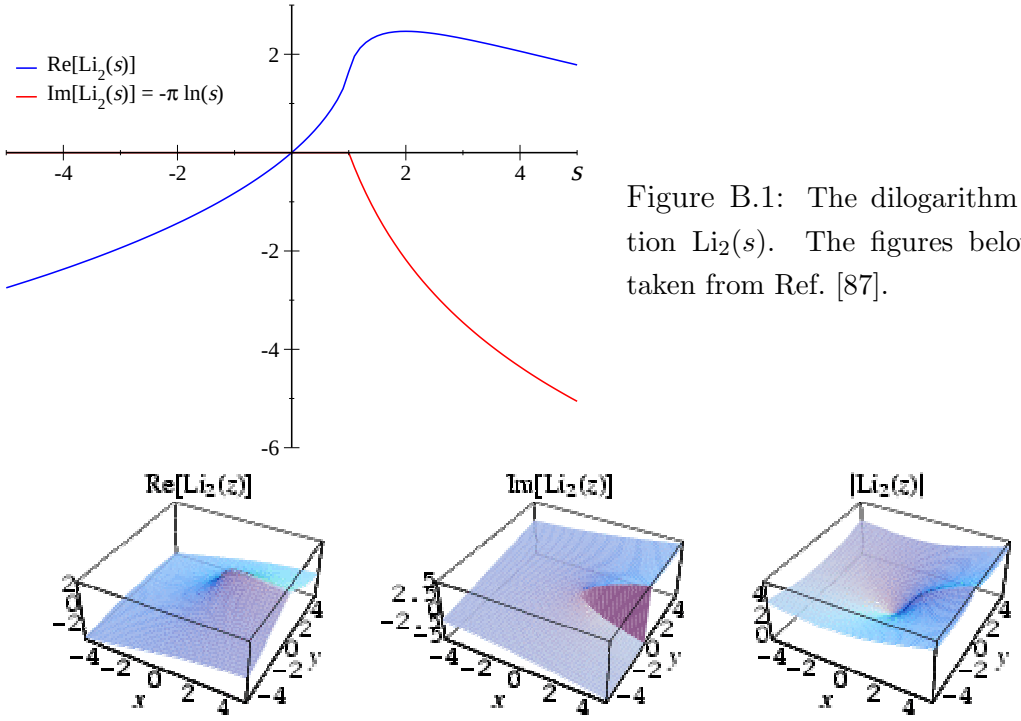

Figure B.1: The dilogarithm function $\mathrm{Li}_2(s)$. The figures below are taken from Ref. [87].

Since there are great numerical problems for evaluating Eq. (B.5) for large, but still finite values of x_n and x_{n+1}, which is the case here[2] (it appears even e^{x_n}), we must find another way to solve Eq. (B.4). Starting point is the function $F(0, x_n)$. For $x_n \to \infty$ the integration is very easy:

$$F(0,\infty) = \int_0^{\infty} \mathrm{d}x\, \frac{x^2 \mathrm{e}^x}{(\mathrm{e}^x - 1)^2} = \frac{\pi^2}{3} \tag{B.8}$$

[1] It is called also *Lewin* function or *Appel* function.

[2] Note that x is defined as $x = \hbar\omega/k_\mathrm{B}T$, so that large values of x are given by low temperatures and/or high frequencies.

which means that for $x_n \to \infty$ the function $F(0, x_n)$ converges to $\pi^2/3$. For small values of x_n, it is possible to evaluate $F(0, x_n)$ without numerical problems. Fig. B.2 shows the behavior of the function $F(0, x)$.

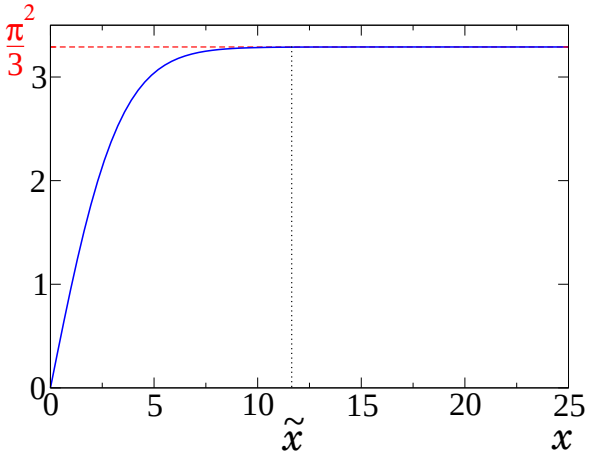

Figure B.2: Plot of the function $F(0,x) = \int_0^x \mathrm{d}t\, t^2 \mathrm{e}^t/(\mathrm{e}^t-1)^2$. Note that in Chap. 5, x depends both on frequency and temperature through the relation $x = \hbar\omega/k_\mathrm{B}T$. For large values of x, the function converges to $\pi^2/3$.

For $x > \tilde{x}$ the function reaches the asymptotic value $\pi^2/3$. That means that starting from a certain value $\tilde{x}$ it is not necessary any more to calculate F using Eq. (B.5), but one can set $F(0, x)$ directly equal to $\pi^2/3$, avoiding numerical problems due to large x values. Then the integral of Eq. (B.4) can be solved as:

$$\kappa_\mathrm{ph} = k_\mathrm{B}\gamma \sum_{n=1}^{N_\mathrm{bin}} \mathcal{T}_n \left(\int_0^{x_{n+1}} \mathrm{d}x\, \frac{x^2\mathrm{e}^x}{(\mathrm{e}^x-1)^2} - \int_0^{x_n} \mathrm{d}x\, \frac{x^2\mathrm{e}^x}{(\mathrm{e}^x-1)^2} \right) \tag{B.9}$$

$$= k_\mathrm{B}\gamma \sum_{n=1}^{N_\mathrm{bin}} \mathcal{T}_n \left[F(0, x_{n+1}) - F(0, x_n) \right]. \tag{B.10}$$

References

[1] H. W. Kroto, J. R. Heath, S. C. O'Brien, R. F. Curl, and R. E. Smalley, *C_{60}: Buckminsterfullerene*, Nature **318**, 162 (1985). `online`.

[2] S. Iijima, *Helical microtubules of graphitic carbon*, Nature **354**, 56 (1991). `online`.

[3] S. Iijima and T. Ichihashi, *Single-shell carbon nanotubes of 1 nm diameter*, Nature **363**, 603 (1993). `online`.

[4] D. S. Bethune, C. H. Kiang, M. S. de Vries, G. Gorman, R. Savoy, J. Vazquez, and R. Beyers, *Cobalt-catalysed growth of carbon nanotubes with single-atomic-layer walls*, Nature **363**, 603 (1993). `online`.

[5] H. W. C. Postma, T. Teepen, Z. Yao, M. Grifoni, and C. Dekker, *Carbon nanotube single-electron transistors at room temperature*, Science **293**, 76 (2001). `online`.

[6] A. Bachtold, P. Hadley, T. Nakanishi, and C. Dekker, *Logic circuits with carbon nanotube transistors*, Science **294**, 1317 (2001). `online`.

[7] J. Hone, B. Batlogg, Z. Benes, A. T. Johnson, and J. Fischer, *Quantized phonon spectrum of single-wall carbon nanotubes*, Science **289**, 1730 (2000). `online`.

[8] K. Schwab, E. A. Henriksen, J. M. Worlock, and M. L. Roukes, *Measurement of the quantum of thermal conductance*, Nature **404**, 974 (2000). `online`.

[9] Z. K. Tang, L. Zhang, L. Wang, X. X. Zhang, G. H. Wen, G. D. Li, J. N. Wang, C. T. Chan, and P. Sheng, *Superconductivity in 4 Angstrom single-walled carbon nanotubes*, Science **292**, 2462 (2001). `online`.

[10] A. M. Rao, E. Richter, S. Bandow, B. Chase, P. C. Eklund, K. A. Williams, S. Fang, K. R. Subbaswamy, M. Menon, A. Thess, R. E. Smalley, G. Dresselhaus, and M. S. Dresselhaus, *Diameter-selective Raman scattering from vibrational modes in carbon nanotubes*, Science **275**, 187 (1997). `online`.

[11] T. Yamamoto, S. Watanabe, and K. Watanabe, *Universal features of quantized thermal conductance of carbon nanotubes*, Phys. Rev. Lett. **92**, 75502 (2004). `online`.

[12] S. Reich, C. Thomsen, and J. Maultzsch, *Carbon nanotubes*. Wiley-VCH, Weinheim, 2004.

[13] R. Saito, G. Dresselhaus, and M. Dresselhaus, *Physical properties of carbon nanotubes*. Imperial College Press, London, 1998.

[14] J. R. Hauptmann, *Spin-transport in carbon nanotubes*. PhD thesis, University of Copenhagen, 2003. `online`.

[15] E. Thune and C. Strunk in *Lecture notes in physics*, G. Cuniberti, G. Fagas, and K. Richter, eds., vol. 680. Springer, Berlin Heidelberg, 2005.

[16] M. T. Dove, *Structure and dynamics*. Oxford University Press, Oxford, 2003.

[17] R. Saito, A. Jorio, A. G. Souza Filho, G. Dresselhaus, M. S. Dresselhaus, and M. Pimenta, *Probing phonon dispersion relations of graphite by double resonance Raman scattering*, Phys. Rev. Lett. **88**, 27401 (2002). `online`.

[18] R. Saito, T. Takeya, T. Kimura, G. Dresselhaus, and M. S. Dresselhaus, *Raman intensity of single-wall carbon nanotubes*, Phys. Rev. B **57**, 4145 (1998). `online`.

[19] M. Born and R. Oppenheimer, *Zur Quantentheorie der Molekeln*, Ann. Physik **84**, 457 (1927).

[20] U. Rössler, *Solid State Theory*. Springer, Berlin Heidelberg, 2004.

[21] G. Czycholl, *Theoretische Festkörperphysik*. Springer, Berlin Heidelberg, 2004.

[22] N. W. Ashcroft and N. D. Mermin, *Solid State Physics*. Saunders College Publishing, 1976.

[23] A. N. Cleland, *Foundations of Nanomechanics*. Springer, Berlin Heidelberg, 2003.

[24] O. Madelung, *Introduction to Solid-State Theory*. Springer, Berlin Heidelberg, 1978.

[25] W. Kohn and L. J. Sham, *Self consistent equations including exchange and correlation effects*, Phys. Rev. **140**, A1133 (1965). `online`.

[26] P. Pavone, *Old and new aspects in lattice-dynamical theory*, J. Phys.: Condens. Matter **13**, 7593 (2001). `online`.

[27] P. Giannozzi, S. de Gironcoli, P. Pavone, and S. Baroni, Ab initio *calculation of phonon dispersions in semiconductors*, Phys. Rev. B **43**, 7231 (1991). `online`.

[28] G. D. Mahan and G. S. Jeon, *Flexure modes in carbon nanotubes*, Phys. Rev. B **70**, 75405 (2004). `online`.

[29] J. G. Kirkwood, *The skeletal modes of vibration of long chain molecules*, J. Chem. Phys. **7**, 506 (1939). `online`.

[30] P. N. Keating, *Effect of invariance requirements on the elastic strain energy of crystals with application to a diamond structue*, Phys. Rev. **145**, 637 (1966). `online`.

[31] K. C. Hass, *Tight binding study of the lattice dynamics of graphite*, Phys. Rev. B **46**, 139 (1992). `online`.

[32] G. Benedek and G. Onida, *Bulk and surface dynamics of graphite with the bond charge model*, Phys. Rev. B **47**, 16471 (1993). `online`.

[33] C. Lobo and J. L. Martins, *Valence force field model for graphene and fullerenes*, Z. Phys. D **39**, 159 (1997). `online`.

[34] G. D. Mahan and G. S. Jeon, *Microscopic origin of infrared activity in graphite*, Phys. Rev. B **71**, 184306 (2005). `online`.

[35] Y. N. Gartstein, *Vibrations of single-wall carbon nanotubes: lattice models and low frequency dispersion*, Phys. Lett. A **327**, 83 (2004). `online`.

[36] Y. N. Gartstein, *Simple empirical model for vibrational spectra of single-wall carbon nanotubes*, Cond-mat/0402286 (2004). `online`.

[37] C. Aizawa, R. Souda, S. Otani, Y. Ishizawa, and C. Oshima, *Bond softening in monolayer graphite formed on transition-metal carbide surfaces*, Phys. Rev. B **42**, 11469 (1990). `online`.

[38] R. M. Martin, *Elastic properties of ZnS structure semiconductors*, Phys. Rev. B **1**, 4005 (1970). online.

[39] H. Rücker and M. Methfessel, *Anharmonic Keating model for group-IV semiconductors with application to the lattice dynamics in alloys of Si, Ge, and C*, Phys. Rev. B **52**, 11059 (1995). online.

[40] R. A. Jishi and G. Dresselhaus, *Lattice-dynamical model for graphite*, Phys. Rev. B **26**, 4514 (1982). online.

[41] R. A. Jishi, L. Venkataraman, M. Dresselhaus, and G. Dresselhaus, *Phonon modes in carbon nanotubules*, Chem. Phys. Lett. **209**, 77 (1993).

[42] J. Maultzsch, S. Reich, C. Thomsen, H. Requardt, and P. Ordejón, *Phonon dispersion in graphite*, Phys. Rev. Lett. **92**, 75501 (2004). online.

[43] C. Oshima, C. Aizawa, R. Souda, Y. Ishizawa, and Y. Sumiyoshi, *Surface phonon dispersion curves of graphite (0001) over the entire energy region*, Solid State Commun. **65**, 1601 (1988). online.

[44] S. Siebenritt, R. Pues, K. Rieder, and A. M. Shikin, *Surface phonon dispersion in graphite and in a lanthanum graphite intercalation compound*, Phys. Rev. B **55**, 7927 (1997). online.

[45] P. Pavone, R. Bauer, K. Karch, O. Schütt, S. Vent, W. Windl, D. Strauch, S. Baroni, and S. de Gironcoli, *Ab initio phonon calculations in solids*, Physica B **219/220**, 439 (1996). online.

[46] O. Dubay and G. Kresse, *Accurate density functional calculations for the phonon dispersion relations of graphite layer and carbon nanotubes*, Phys. Rev. B **67**, 35401 (2003). online.

[47] L. Vitali, M. A. Schneider, K. Kern, L. Wirtz, and A. Rubio, *Phonon and plasmon excitation in inelastic electron tunneling spectroscopy of graphite*, Phys. Rev. B **69**, 121414 (2004). online.

[48] L.-H. Ye, B.-G. Liu, D.-S. Wang, and R. Han, *Ab initio dispersions of single-wall carbon nanotubes*, Phys. Rev. B **69**, 235409 (2004). online.

[49] N. Mounet and N. Marzari, *First principles determination of the structural, vibrational and thermodynamic properties of diamond, graphite, and derivatives*, Phys. Rev. B **71**, 205214 (2005). online.

[50] K. P. Bohnen and R. Heid, private communication.

[51] P. Pavone, K. Karch, O. Schütt, D. Strauch, W. Windl, P. Giannozzi, and S. Baroni, *Ab initio lattice dynamics in diamond*, Phys. Rev. B **48**, 3156 (1993). `online`.

[52] A. Grüneis, R. Saito, T. Kimura, L. G. Cancado, M. A. Pimenta, A. Jorio, A. G. Souza Filho, G. Dresselhaus, and M. S. Dresselhaus, *Determination of two-dimensional phonon dispersion relation of graphite by Raman spectroscopy*, Phys. Rev. B **65**, 155405 (2002). `online`.

[53] G. Samsonidze, R. Saito, A. Jorio, A. Souza Filho, A. Grüneis, M. A. Pimenta, G. Dresselhaus, and M. S. Dresselhaus, *Phonon trigonal warping effect in graphite and carbon nanotubes*, Phys. Rev. Lett. **90**, 27403 (2003). `online`.

[54] V. N. Popov, V. E. van Doren, and M. Balkanski, *Lattice dynamics of single-walled carbon nanotubes*, Phys. Rev. B **59**, 8355 (1999). `online`.

[55] V. N. Popov, V. E. van Doren, and M. Balkanski, *Elastic properties of single-walled carbon nanotubes*, Phys. Rev. B **61**, 3078 (2000). `online`.

[56] J. Yu, R. K. Kalia, and P. Vashishta, *Phonons in graphitic tubules: a tight binding molecular dynamics study*, J. Chem. Phys. **103**, 6697 (1995). `online`.

[57] D. Sánchez-Portal, E. Artacho, J. M. Soler, A. Rubio, and P. Ordejón, *Ab initio structural, elastic, and vibrational properties of carbon nanotubes*, Phys. Rev. B **59**, 12678 (1999). `online`.

[58] K. P. Bohnen, R. Heid, H. J. Liu, and C. T. Chan, *Lattice dynamics and electron-phonon interaction in (3,3) carbon nanotubes*, Phys. Rev. Lett. **93**, 245501 (2004). `online`.

[59] X. Zhao, Y. Liu, S. Inoue, T. Suzuki, R. O. Jones, and Y. Ando, *Smallest carbon nanotube is 3 Å in diameter*, Phys. Rev. Lett. **92**, 125502 (2004). `online`.

[60] S. Roth and D. Carroll, *One-dimensional metals*. Wiley-VCH, Weinheim, 1999.

[61] J. X. Cao, X. H. Yan, Y. Xiao, Y. Tang, and J. W. Ding, *Exact study of lattice dynamics of single-walled carbon nanotubes*, Phys. Rev. B **67**, 45413 (2003). `online`.

[62] S. Rols, Z. Benes, E. Anglaret, J. L. Sauvajol, P. Papanek, J. E. Fischer, G. Coddens, H. Schober, and A. J. Dianoux, *Phonon density of states of single-wall carbon nanotubes*, Phys. Rev. Lett. **85**, 5222 (2000). `online`.

[63] B. J. LeRoy, S. G. Lemay, J. Kong, and C. Dekker, *Electrical generation and absorption of phonons in carbon nanotubes*, Nature **432**, 371 (2004). `online`.

[64] A. M. Rao, J. Chen, E. Richter, U. Schlecht, P. C. Eklund, R. C. Haddon, U. D. Venkateswaran, Y. K. Kwon, and D. Tománek, *Effect of van der Waals interactions on the Raman modes in single walled carbon nanotubes*, Phys. Rev. Lett. **86**, 3895 (2001). `online`.

[65] J. Kürti, G. Kresse, and H. Kuzmany, *First-principles calculations of the radial breathing mode of single-wall carbon nanotubes*, Phys. Rev. B **58**, 8869 (1998). `online`.

[66] M. Machón, S. Reich, H. Telg, J. Maultzsch, P. Ordejón, and C. Thomsen, *Strength of radial breathing mode in single-walled carbon nanotubes*, Phys. Rev. B **71**, 35416 (2005). `online`.

[67] Y. Xiao, Z. M. Li, X. H. Yan, Y. Zhang, Y. L. Mao, and Y. R. Yang, *Curvature effect on the radial breathing modes of single-walled carbon nanotubes*, Phys. Rev. B **71**, 233405 (2005). `online`.

[68] L. X. Benedict, S. G. Louie, and M. L. Cohen, *Heat capacity of carbon nanotubes*, Solid State Commun. **100**, 177 (1996). `online`.

[69] S. Berber, Y.-K. Kwon, and D. Tománek, *Unusually high thermal conductivity of carbon nanotubes*, Phys. Rev. Lett. **84**, 4613 (2000). `online`.

[70] G. P. Srivastava, *The physics of phonons*. Adam Hilger IOP publishing Ltd, Bristol, 1990.

[71] A. Mizel, L. Benedict, M. Cohen, S. Louie, A. Zettl, N. Budraa, and W. Beyermann, *Analysis of the low-temperature specific heat of multiwalled carbon nanotubes and carbon nanotube ropes*, Phys. Rev. B **60**, 3264 (1999). `online`.

[72] J. Hone, M. C. Llaguno, M. J. Biercuk, A. T. Johnson, B. Batlogg, Z. Benes, and J. Fischer, *Thermal properties of carbon nanotubes and nanotube-based materials*, Appl. Phys. A **74**, 339 (2002). `online`.

[73] V. N. Popov, *Low-temperature specific heat of nanotube systems*, Phys. Rev. B **66**, 153408 (2002). `online`.

[74] E. Dobardžić, I. Milošević, T. Vuković, and M. Damnjanović, *Single-wall carbon nanotubes phonon spectra: symmetry based calculations*, Phys. Rev. B **68**, 45408 (2003). `online`.

[75] C. Li and T.-W. Chou, *Quantized molecular structural mechanics modeling for studying the specific heat of single-walled carbon nanotubes*, Phys. Rev. B **71**, 75409 (2005). `online`.

[76] S. Datta, *Electronic Transport in Mesoscopic Systems*. Cambridge University Press, Cambridge, 1995.

[77] D. E. Angelescu, M. C. Cross, and M. L. Roukes, *Heat transport in mesoscopic systems*, Superlatt. Microstruct. **23**, 673 (1998). `online`.

[78] L. Rego and G. Kirczenow, *Quantized thermal conductance of dielectric quantum wires*, Phys. Rev. Lett. **81**, 232 (1998). `online`.

[79] L. Rego and G. Kirczenow, *Fractional exclusion statistics and the universal quantum of thermal conductance: a unifying approach*, Phys. Rev. B **59**, 13080 (1999). `online`.

[80] N. Mingo and D. A. Broido, *Carbon nanotube ballistic thermal conductance and its limits*, Phys. Rev. Lett. **95**, 96105 (2005). `online`.

[81] E. Brown, L. Hao, J. C. Gallop, and J. C. Macfarlane, *Ballistic thermal and electrical conductance measurements on individual multiwall carbon nanotubes*, Appl. Phys. Lett. **87**, 23107 (2005). `online`.

[82] V. N. Popov and L. Henrard, *Breathinglike phonon modes of multiwalled carbon nanotubes*, Phys. Rev. B **65**, 235415 (2002). `online`.

[83] M. Gheorghe, R. Gutiérrez, N. Ranjan, A. Pecchia, A. Di Carlo, and G. Cuniberti, *Vibrational effects in the linear conductance of carbon nanotubes*, Europhys. Lett. **71**, 438 (2005). `online`.

[84] D. A. Ryndyk, M. Hartung, and G. Cuniberti, *Nonequilibrium excitations of molecular vibrons*, Phys. Rev. B **73**, 45420 (2006). `online`.

[85] M. Hartung, *Effects of vibration on charge transport through molecular bridges*, Master's thesis, University of Regensburg, 2004. `online`.

[86] M. Roukes, *Nanoelectromechanical systems face the future*, PhysicsWorld **14**, (2001). `online`.

[87] E. W. Weisste. `http://mathworld.wolfram.com/Dilogarithm.html`. From *Mathworld* – Wolfram web resource.

Danksagung

Als erstes möchte ich mich bei meinem Betreuer Dr. Giovanni Cuniberti bedanken, der mir einen ersten Einblick in wissenschaftliche Arbeitsweise und Forschung ermöglicht hat. Seine Neugierde und seine Liebe zum Detail sind mir im laufe dieses Jahres ein wichtiges Beispiel gewesen.

Ein herzliches Dankeschön geht an *Maestro* Dr. Pasquale Pavone. Er hat mich mit seiner Begeisterung und Optimismus durch die komplexe Welt der Phononen geleitet. Seine unerschütterliche Ruhe hat mir geholfen immer das positive der Dinge zu sehen.

Der wesentliche Teil dieser Arbeit kam Dank des Beitrages von Dr. Klaus-Peter Bohnen und Dr. Rolf Heid zustande. Sie haben mir freundlicherweise die *ab initio* Daten von Graphene zur Verfügung gestellt. Einen großen Teil der Informatikkenntnisse die ich in diesem Jahr angeeignet habe verdanke ich Michael Hartung, der mir stets hilfsbereit zur Seite stand. Ich bedanke mich bei Dr. Andrea Donarini für seinen grundlegenden Beitrag im letzten Teil meiner Arbeit.

Ich möchte mich bei allen Mitgliedern der Arbeitsgruppe für die gemeinsamen Momente bedanken; ganz besonders danke ich Norbert Nemec und Dr. Rafael Gutiérrez für ihre wissenschaftliche Unterstützung. Ich bedanke mich bei meinen Kollegen im *Diplomandenzimmer* Andreas Pfund, Thomas Ernst, Mirjam Schmid und Matthias Scheid für die freundschaftliche Atmosphäre und die angenehmen Ablenkungen.

Ein besonderer Dank geht an Dr. Dario Bercioux für seine unverzichtbare Hilfe bei allen Angelegenheiten rund um meine Arbeit und für seine nützlichen Tips. Mit seinen stets motivierenden Worten und seiner endlosen Geduld ist er mir eine wichtige Stütze gewesen.

Ich möchte meinen Eltern dafür danken, dass sie mich in diesen Jahren unterstützt haben und Vertrauen in mich gehabt haben. Sie haben mich bis zum Erreichen dieses wichtigen Ziels immer wieder ermutigt.

Regensburg, März 2006

Ringraziamenti

Inanzitutto ringrazio il Dott. Giovanni Cuniberti per avermi introdotto al mondo della ricerca universitaria e per il tempo dedicato a condurmi nei vari ambiti del progetto. La sua curiosità scientifica e il suo spirito critico mi sono stati da insegnamento nel corso di quest'anno.

Un grandissimo ringraziamento va al *Maestro* Dott. Pasquale Pavone. È lui che col suo entusiasmo ed ottimismo mi ha guidata nel vibrante mondo dei fononi. La sua infrangibile calma mi ha portato a vedere sempre il lato positivo delle cose.

La parte originale di questo lavoro ha avuto luce grazie al contributo del Dott. Klaus-Peter Bohnen e del Dott. Rolf Heid, che mi hanno gentilmente messo a disposizione i dati *ab initio* della grafene. La maggior parte delle conoscenze informatiche acquisite in quest'anno le devo a Michael Hartung, che è sempre stato disposto ad aiutarmi. Vorrei ringraziare il Dott. Andrea Donarini per il suo indispensabile apporto nell'ultima parte del mio lavoro.

Ringrazio tutti i miei compagni di gruppo per i momenti di lavoro e di relax; in particolare Norbert Nemec ed il Dott. Rafael Gutiérrez. Ringrazio i miei compagni della *Diplomandenzimmer* Andreas Pfund, Thomas Ernst, Mirjam Schmid e Matthias Scheid per l'atmosfera amichevole e le piacevoli distrazioni.

Un ringraziamento particolare va al Dott. Dario Bercioux per il suo fondamentale contributo a tutte le faccende riguardanti questa tesi e per i suoi immancabili consigli. Con le sue parole incoraggianti e tanta pazienza ha saputo darmi sempre il giusto appoggio.

Vorrei ringraziare i miei genitori per aver creduto in me e per avermi sostenuto nel corso di questi anni. Mi hanno dato supporto fino al raggiungimento di questo importante traguardo.

Regensburg, marzo 2006

Erklärung

Hiermit erkläre ich, dass ich die Diplomarbeit selbstständig angefertigt habe und keine Hilfsmittel außer den in der Arbeit angegebenen benutzt habe.

Regensburg, den 13. März 2006

.....

Janina Zimmermann